A Multi-Scale Approach to Shaping Carbon Nanotube Structures for Hollow Microneedles

Thesis by

Bradley Lyon

In Partial Fulfillment of the Requirements

for the Degree of

Doctor of Philosophy

CALIFORNIA INSTITUTE OF TECHNOLOGY

Pasadena, California

2014

(Defended May 13, 2014)

Acknowledgements

I would like to begin by thanking my advisor, Professor Morteza Gharib, for his inspiring guidance and leadership throughout this project. I would also like to thank my thesis committee, Professors Beverley McKeon, Guruswami Ravichandran, and Yu-Chong Tai, for their support and helpful feedback.

I would like to thank the entire Gharib group for their support and camaraderie. In particular, I thank Adrianus Indrat Aria for being a great mentor, teammate, and friend. I thank Masoud Beizai for his assistance and unique insights. I thank Amir Gat for his friendship and his assistance in the initial stages of the project. I thank Julia Cossé for her assistance in fabricating molds for the silicone skin patches. I thank all of my undergraduate students for their assistance: Melissa Cronin and Sreeni Appasani, for fabricating skin patches to support the *in vivo* study, and Neeru Ravi for her assistance in running experiments for the fluid absorbance of CNTs.

I would like to acknowledge the assistance from Kavli Nanoscience Institute (KNI), UCLA Nanolab, and the Analytical Facility of Geology and Planetary Sciences in providing access to state of the art fabrication and characterization equipment that was crucial to the success of this project. I especially would like to thank Hoc Ngo, Risaku Toda, and Jim Lacy for their assistance in catalyst deposition, Chi Ma for assistance in sample imaging, and Guy DeRose for assistance in obtaining AFM data.

I would like to thank the Office of Laboratory Animal Resources (OLAR) for their outstanding support of the *in vivo* study. I want to thank Dr. Janet Baer and Dr. Karen Lencioni for their assistance in designing the methodology for the *in vivo* study. I want to thank Melissa McPherson, Gwen Williams, and Monica Calvario for providing the technical expertise for

working with the animals that made the *in vivo* study possible. I also want to thank the OLAR staff for locating homes for all of the rabbits at the conclusion of the *in vivo* study.

I would also like to thank both Dr. Brittney DeClerck of the USC Keck Medical Center and Dr. Leslie Ballas of the USC Norris Cancer Center for their tremendous care and support. I would like to additionally thank Dr. Brittney DeClerck for the insightful discussions on transdermal drug delivery.

I would like to thank my family for their unwavering love and support. I am grateful to my pets for the joy they bring to my life: my dogs, Joey and Lily, and my rabbit, Cali (formerly Rabbit #2). Finally, I thank my wife and best friend, Rebecca Meltzer Lyon, whose love and support means everything to me.

Abstract

The concept of a carbon nanotube microneedle array is explored in this thesis from multiple perspectives including microneedle fabrication, physical aspects of transdermal delivery, and *in vivo* transdermal drug delivery experiments. Starting with standard techniques in carbon nanotube (CNT) fabrication, including catalyst patterning and chemical vapor deposition, vertically-aligned carbon nanotubes are utilized as a scaffold to define the shape of the hollow microneedle. Passive, scalable techniques based on capillary action and unique photolithographic methods are utilized to produce a CNT-polymer composite microneedle. Specific examples of CNT-polyimide and CNT-epoxy microneedles are investigated. Further analysis of the transport properties of polymer resins reveals general requirements for applying arbitrary polymers to the fabrication process.

The bottom-up fabrication approach embodied by vertically-aligned carbon nanotubes allows for more direct construction of complex high-aspect ratio features than standard top-down fabrication approaches, making microneedles an ideal application for CNTs. However, current vertically-aligned CNT fabrication techniques only allow for the production of extruded geometries with a constant cross-sectional area, such as cylinders. To rectify this limitation, isotropic oxygen etching is introduced as a novel fabrication technique to create true 3D CNT geometry. Oxygen etching is utilized to create a conical geometry from a cylindrical CNT structure as well as create complex shape transformations in other CNT geometries.

CNT-polymer composite microneedles are anchored onto a common polymer base less than 50 µm thick, which allows for the microneedles to be incorporated into multiple drug delivery platforms, including modified hypodermic syringes and silicone skin patches.

Cylindrical microneedles are fabricated with 100 µm outer diameter and height of 200-250 µm with a central cavity, or lumen, diameter of 30 µm to facilitate liquid drug flow. *In vitro* delivery experiments in swine skin demonstrate the ability of the microneedles to successfully penetrate the skin and deliver aqueous solutions.

An *in vivo* study was performed to assess the ability of the CNT-polymer microneedles to deliver drugs transdermally. CNT-polymer microneedles are attached to a hand actuated silicone skin patch that holds a liquid reservoir of drugs. Fentanyl, a potent analgesic, was administered to New Zealand White Rabbits through 3 routes of delivery: topical patch, CNT-polymer microneedles, and subcutaneous hypodermic injection. Results demonstrate that the CNT-polymer microneedles have a similar onset of action as the topical patch. CNT-polymer microneedles were also vetted as a painless delivery approach compared to hypodermic injection. Comparative analysis with contemporary microneedle designs demonstrates that the delivery achieved through CNT-polymer microneedles is akin to current hollow microneedle architectures. The inherent advantage of applying a bottom-up fabrication approach alongside similar delivery performance to contemporary microneedle designs demonstrates that the CNT-polymer composite microneedle is a viable architecture in the emerging field of painless transdermal delivery.

LIST OF FIGURES

LIST OF TABLES

TABLE OF CONTENTS

Chapter 1

Introduction

1.1 Review of Microneedles

Microneedles represent a potentially transformative technology for drug delivery. Microneedles replace standard hypodermic injections performed by a medical professional, with a painless delivery that can be self-administered by the patient. This transformation is particularly powerful in the developing world, which requires a decentralized strategy for healthcare to compensate for a shortage of medical personnel and facilities (Chin 2009). Specifically for vaccinations, microneedle delivery into the skin has demonstrated enhanced immune response over standard intramuscular injection. This allows for reduction in the volume of therapeutic agent required to inoculate a patient, which can ultimately increase the supply of vaccines and lower the cost of inoculation per patient (Kim et al. 2012; Kim and Prausnitz 2011; La Montagne and Fauci 2004). Reduction in vaccine dose enables more effective management of vaccine supply, including more rapid production of vaccine for emerging pathogen threats and better handling of sudden supply shocks. In 2004, a supply shock of influenza vaccine occurred in the United States as vaccine contamination cut the available vaccine supply in half (Kenney et al. 2004).

Fear of hypodermic needle injections, or needle phobia, is estimated to affect over 10% of the population (Birchall 2006). The painless aspect of microneedles alone is predicted to improve patient compliance for medical treatments performed routinely via hypodermic injection.

Previous studies have demonstrated that microneedles significantly reduce the amount of pain and discomfort felt by patients (Gill et al. 2008). The painless attribute of microneedles is attributed primarily to the short length of the microneedles, typically less than 1 mm. The short length of the microneedles is designed to allow for precise delivery into the epidermis and upper dermis layers of the skin. The epidermis and upper dermis layers of skin contain a sparse distribution of nerves resulting in a painless delivery. In comparison, hypodermic injections are typically given in deeper tissues, such as the subcutaneous layer of the skin and the muscles, which contain a higher concentration of nerves. (Hegde, Kaveri, and Bayry 2011). A schematic of the different layers of the skin and the target delivery depth for microneedles and conventional delivery methods including topical patches and hypodermic injection is shown in Figure 6.1.

Within the last decade, much progress has been made in the development of different microneedle architectures. Solid microneedles do not directly deliver drugs, but are used to painlessly penetrate the skin. Solid microneedles have been marketed for a variety of applications including scar treatment (Doddaballapur 2009) and improving skin permeability of topical drug formulations (Zhou et al. 2010). Several solid microneedle products have been commercialized and are now commonly available, including Dermaroller® (AesthetiCare, West Yorkshire, UK) and Genosys® (Hansderma, Downey, CA) (Kim, Park, and Prausnitz 2012).

Coated and dissolving microneedles have been shown to fulfill a unique niche in allowing for passive, continuous release of drug into the skin by using a dissolving polymer matrix embedded with drugs to either coat a solid microneedle or to mold a microneedle completely from the polymer matrix. Drug delivery rates are tied to the rate at which the polymer matrix dissolves in the skin, which can last from minutes for water soluble polymers or up to weeks or months for biodegradable polymers (Sullivan et al. 2010; Lee et al. 2011; Cormier et al. 2004; Park, Allen, and Prausnitz 2005). Dissolving microneedles have been formulated to allow for administration of large biotherapeutics such as influenza vaccine (Sullivan et al. 2010). A

commercially available dissolving microneedle, MicroHyala® (CosMED Pharmaceutical Co, Kyoto, Japan), has been marketed for cosmetic purposes to treat wrinkles.

Hollow microneedles conceptually act like an array of small hypodermic microneedles. The central cavity, or lumen, of the hollow microneedles allows for injection of liquid drug solutions. Hollow microneedles potentially offer a large advantage in performance over other microneedle architectures. By acting purely as a mechanical conduit for delivery without having to incorporate drug into the structure of the needle, the architecture is more flexible and can allow for more direct application of existing drug formulations currently used for hypodermic injection. Additionally, the hollow microneedle allows for delivery of larger drug molecules and volumes than other microneedle architectures (Kim, Park, and Prausnitz 2012). By interfacing the hollow microneedles with micropumps, the hollow microneedle can facilitate active control over the drug delivery profile to allow for continuous drug release or closed-loop control of drug administration when coupled with an external sensor for applications such as insulin delivery (Ma et al. 2006; Ali and Nagib 2011; Ochoa, Mousoulis, and Ziaie 2012; Zisser and Jovanovic 2006).

Complications in fabrication have been identified as a deterrent against future development of hollow microneedle platforms (Kim, Park, and Prausnitz 2012). The primary approaches for fabricating hollow microneedles to date have all focused on top-down approaches using materials such as silicon, metal, or glass. Top-down fabrication methods start with a bulk material and progressively creating smaller features through processes such as wafer etching or glass pulling. Silicon microneedles are routinely fabricated from silicon wafers by reactive ion etching and have demonstrated success in delivering drug in solid, coated, and hollow microneedle architectures (Häfeli et al. 2009; Gardeniers et al. 2003). However, the requirement to fabricate a hollow cavity, or lumen, for hollow microneedles poses additional fabrication challenges for top-down approaches. Specifically for silicon microneedles, the geometry of the microneedle is defined in piecemeal. Separate etching sequences are required to define the outer

shape of the microneedle, to create the lumen, and to optimize the overall structure. Overall, the iterated etching sequences add considerable time and cost to fabrication, limiting the commercial viability of the technology.

Here, a novel bottom-up approach to fabricating hollow microneedles using vertically-aligned carbon nanotubes (VA-CNTs) is introduced. Bottom-up processes create a micro- or nano- structure by assembly of smaller components. For carbon nanotubes, chemical vapor deposition allows for self-assembly of carbon atoms to fabricate carbon nanotubes. This bottom-up approach is intended to provide a much simpler and more scalable alternative to contemporary top-down approaches for producing hollow microneedles to allow for future technological, medicinal, and industrial development of the hollow microneedle architecture.

1.2 Objectives

The use of carbon nanotubes to create a hollow microneedle is a brand-new concept. As such, the primary purpose of this thesis is to broadly investigate the feasibility of the concept from a wide range of perspectives including microneedle fabrication, incorporation in drug delivery platforms, and delivery performance from both a physical and medicinal perspective. Looking forward, the desired outcome of this study is to create a broad foundation for the CNT microneedle concept in order to motivate continued interest and research in both the microneedle and CNT fabrication communities.

Each chapter is organized to investigate a single facet of the CNT microneedle concept. Chapter 2 provides background on carbon nanotubes (CNTs) and discusses the present challenges in applying the standard CNT fabrication techniques to producing a microneedle. Chapters 3 and 4 focus on the fabrication of CNT-polymer composite microneedles, including the fabrication methodology and process requirements for selecting polymers that are compatible with the fabrication methods. Chapter 4 analyzes in detail the microfluidic transport of polymer resin

during the fabrication process. Chapters 5 through 6 focus on the delivery performance of a subset of CNT-polymer composite microneedle designs through *in vitro* delivery experiments and an *in vivo* study examining the use of the CNT-polymer composite microneedle to delivery fentanyl transdermally. In this study, the primary delivery platform used in conjunction with the CNT microneedles is a hand actuated skin patch. Of particular interest for delivery is to separately analyze the contributions of the CNT microneedles from the contributions of the skin patch. In this context, the general performance of the CNT microneedles can be extracted from the combined performance of the skin patch-CNT microneedle delivery system.

In Chapter 7, a more fundamental study is undertaken on optimizing the geometry of CNT bundles through oxygen etching. The goal of the oxygen etching study is to demonstrate an approach to expand on the standard patterning capabilities of CNT fabrication as presented in Chapter 2. Within the context of the objectives of each chapter, the experimental results of the CNT microneedle are compared to similar data from existing hollow microneedle architectures. This analysis is used to determine where CNT microneedles may provide a comparative advantage over current approaches, and in which areas the CNT microneedle may still be deficient.

1.3 Scope

The fields of CNT fabrication and microneedles are both well established. Work on CNTs dates back to 1991 with the synthetic fabrication of CNTs by Iijima (Iijima 1991). Today, CNT research has grown exponentially, with over 24,000 publications and 2,000 patents issued in the year 2011 alone (De Volder et al. 2013). The field of modern microneedles began to develop in 1998 as the microfabrication techniques from the microelectronics industry were adapted for microneedle fabrication. Since the 1990s, the microneedle field has grown steadily, with over 300 publications in the year 2011 alone (Kim, Park, and Prausnitz 2012). Despite the large scope of

these fields, little, if any, overlap between the fields of carbon nanotubes and microneedles exists. Literature searches demonstrate that the closest embodiment to a CNT microneedle that has been previously considered is to fabricate CNTs on top of a solid silicon microneedle to act as a sensing element for glucose in interstitial fluid (Yoon et al. 2013).

Current challenges in the individual fields of CNT fabrication and microneedles are presented to provide context to the CNT microneedle. These issues include topics such as the ability to scale CNT fabrication to industrial production, limitations in total deliverable drug volume through hollow microneedles, and the general biocompatibility of microneedles. However, these issues of the parent fields are not investigated in detail in this study. Instead, the scope of this thesis is limited to the development of the CNT microneedle architecture and the unique advantages and challenges that this architecture represents.

One of the unique characteristics of this study is the presentation of the CNT microneedle from concept all the way to *in vivo* drug delivery study. The ability to rapidly propel this study in terms of technology development required limiting the number of microneedle embodiments under consideration in this study to only a few representative designs in terms of CNT properties, polymer choice, needle geometry, and delivery platform. However, discussions are presented throughout the thesis on how the concepts presented can be extended to arbitrary CNT microneedle designs. In particular, Chapter 4 analyzes the fabrication of the CNT-polymer composite from a microfluidic perspective in order to develop criteria for introducing arbitrary polymers into the CNT composite architecture.

1.4 Thesis Overview

Chapter 2 introduces the bottom-up assembly approach embodied by carbon nanotubes, and discusses the inherent benefits and challenges of using CNTs to produce microneedles. The standard fabrication techniques of catalyst patterning and chemical vapor deposition for

producing patterned vertically-aligned carbon nanotube arrays are reviewed. Additionally, the specific procedure and methodology used for fabricating CNTs in this study are also presented.

Chapter 3 focuses on the fabrication process to transform patterned vertically-aligned CNTs into CNT-polymer composite microneedles. Fabrication techniques are demonstrated for two classes of polymers: thermoset polymers and negative photoresists. A comparison of the fabrication and geometry of the CNT-polymer microneedle to other microneedle architectures is presented.

Chapter 4 deconstructs the fabrication processes presented in Chapter 3 into a set of criteria to allow for screening of arbitrary thermoset polymers and negative photoresists for incorporation into the CNT-polymer microneedle concept. Specific attention is given to the transport of polymer resin through the porous CNT scaffold in order to understand the formation of the CNT-polymer composite. From this, criteria based on the physical properties of the polymer resin are determined for properly screening candidate thermoset polymers. The goal of this study is to allow for universal adaption of the CNT-polymer composite microneedle beyond the representative polymers that are discussed within the scope of this thesis.

Chapter 5 investigates the physical aspects of delivery through the CNT-polymer microneedles on the level of laboratory and *in vitro* swine skin delivery experiments. The CNT-polymer microneedles are incorporated onto several delivery platforms including syringes, hand actuated skin patches, and syringe pump actuated skin patches. Of particular interest here is to evaluate the performance of the microneedles separately from the performance of the microneedle-delivery platform system. Focus in analysis is given to the physical conditions of delivery, including how the geometry of the microneedle influences the hydraulic resistance of delivery and the ability of the microneedle to successfully penetrate the skin.

Chapter 6 focuses on the delivery of the CNT-polymer microneedles from the perspective of drug delivery. An *in vivo* study is performed looking at the delivery of fentanyl, a potent analgesic, through the CNT-polymer microneedles attached to a hand actuated skin patch delivery platform. Delivery of fentanyl through the microneedles is compared to standard delivery routes, including topical patch and subcutaneous injection. Based on the results of this *in vivo* study, discussion focuses on the possible medical applications of the CNT-polymer microneedles, and how the delivery of the CNT-microneedle-skin patch system presented here compares to other hollow microneedle architectures.

Chapter 7 explores the use of isotropic oxygen etching to create true three-dimensional CNT bundle geometry. As will be discussed in Chapter 2, typical CNT fabrication techniques only allow for the creation of CNT bundles with constant cross-section geometry. Oxygen etching is investigated within the context of producing optimal microneedle geometry, including the formation of a taper geometry to allow for longer microneedles. A model is presented to predict microneedle geometry produced by oxygen etching, and to better understand the nature of the shape transformation.

Chapter 8 summarizes the results of the study. Directions for future study of CNT-polymer composite microneedles as presented throughout the thesis are also summarized.

Chapter 2

Vertically-Aligned Carbon Nanotubes: Overview and Application to Hollow Microneedles

2.1 Introduction

As introduced in Section 1.1, carbon nanotube microneedles represent a paradigm shift in the approach to fabricating microneedles. The modern field of microneedles, originating in the 1990s, adapted top-down fabrication techniques from the microelectronics industry for producing integrated circuits (Kim, Park, and Prausnitz 2012). However, the high aspect ratio geometry required for a microneedle can be created more simply using a bottom-up approach rather than a top-down approach. In fact, in the first paper on the synthetic fabrication of carbon nanotubes by Iijima, before the term "carbon nanotube" was put into common use, Iijima first describes the material as "needle-like tubes" (Iijima 1991). The challenge of implementing bottom-up processing in practice is the reliance on passive physical and chemical nano-scale mechanisms to "self-assemble" materials. Therefore, a large degree of nanoscience and process engineering is required to develop a reliable fabrication procedure. In addition to carbon nanotubes, other examples of bottom-up materials include silicon nanowires (Huang, Fang, and Zhu 2007), quantum dots (Marzin et al. 1994), and DNA.

CNT synthesis can be achieved through several techniques including arc discharge, laser ablation, and chemical vapor deposition. Arc discharge and laser ablation are commonly used in industrial applications. However, they only allow for the fabrication of CNT powders comprised of randomly aligned CNTs without attachment to an underlying substrate. In the form of a powder, CNTs are limited to architectures where they are dispersed in a solution to form materials such as composites, paints, and thin films. A wide array of applications using powder CNTs has been commercialized to date. CNTs are mixed with plastic resins to form electrically conducting plastics for electromagnetic shielding (Yang et al. 2005). Powder CNT composites have been generated for a variety of products including sports equipment, wind turbine blades, and boat hulls. CNT powders have been incorporated in the cathode and anode structures in commercial lithium-ion batteries to improve electrical conductivity and mechanical integrity during cycling (De Volder et al. 2013). Powder CNTs have been utilized to develop membranes for commercial water filtration systems (Upadhyayula et al. 2009). CNT coatings are also currently being developed to passively prevent ice accumulation on aircraft (Batelle Memorial Institute, 2011).

On the laboratory level, arc discharge, laser ablation, and chemical vapor deposition are all very common techniques to fabricate carbon nanotubes. However, CNTs produced by chemical vapor deposition have had considerably less commercial success to present. Chemical vapor deposition, as will be presented in this study, is the only fabrication method that allows for patterned growth of CNTs on a substrate. CVD truly enables the spirit of bottom-up assembly by allowing for atom-by-atom assembly of carbon atoms to produce carbon nanotubes on the nano-scale that are used in turn to create complex CNT patterns all the way to the micro- and macro-scales. The most promising set of commercial applications, to date, that utilize CVD fabrication is the use of vertically-aligned CNTs as a feedstock for producing high tensile strength, electrically conductive yarns (Park and Lee 2012). The direct use of actual patterned CNTs has been limited

to industrial research and development for applications ranging from electrical interconnects, to supercapacitor electrodes, to thermal interfaces for microelectronics (De Volder et al. 2013).

The use of patterned CNTs is constrained by a number of factors, including cost and a lack of techniques to transfer the CNT structures to secondary substrates and modify the structure through mechanical and chemical techniques without damaging the structure. The goal of this study is to demonstrate how the bottom-up approach can allow for the fabrication of complex mechanical structures in the embodiment of the hollow microneedle. Here, the concepts of patterned, aligned carbon nanotube fabrication through catalyst deposition and chemical vapor deposition will be introduced and discussed. From this context, an analysis of the benefits and challenges of using CNTs to produce hollow microneedles will be presented.

2.2 Fabrication Process

2.2.1 Overview

Figure 2.1 illustrates the process of fabricating patterned vertically-aligned carbon nanotube arrays. The general processes of fabricating patterned vertically-aligned carbon nanotubes through catalyst patterning and chemical vapor deposition has been developed and demonstrated in prior studies (Teo et al. 2001) (Milne et al. 2004). During chemical vapor deposition, vertically-aligned carbon nanotubes are fabricated through atomic self-assembly catalyzed by iron nanoparticles. By controlling the position of iron catalyst on a substrate material, vertically-aligned carbon nanotubes can be patterned in arrays conforming to the position of the iron catalyst. Carbon nanotubes fabricated in this study are multi-wall with an average diameter of 20 nm with a mean interspacing of 50 nm, resulting in a packing density in the range of 120-180 nanotubes per square micrometer (Aria 2013). The height of the vertically-aligned carbon nanotube array can be varied between 100 µm – 1 mm.

I. Photolithography

Photoresist
Substrate

1. Spin Coat & Soft Bake

UV

2. Pattern Transfer
(*UV Exposure*)

4. Develop Photoresist in Base Solution

3. Post-Exposure Bake of Photoresist

II. Catalyst Deposition

1. Electron Beam Deposition of Catalyst Layers

2. Liftoff of Photoresist Mask

III. Chemical Vapor Deposition

700 °C

H_2

1. Catalyst Sintering
(*Pretreatment*)

700 °C

C_2H_4
H_2

2. CNT Growth

Figure 2.1- Flowchart for fabricating patterned vertically-aligned CNTs

CNT fabrication can be divided into two processes: catalyst patterning and nanotube synthesis. For catalyst patterning, photolithography is used to create a polymer mask on top of a substrate to define the geometry of the catalyst pattern. Next, physical vapor deposition is used to deposit a uniform nanometer-thin catalyst layer along with several underlying layers that support

the catalyst. For this study, electron beam evaporation is used as the physical vapor deposition method. After catalyst deposition, the polymer mask is removed from the substrate, leaving only the patterned catalyst on the substrate.

Nanotube synthesis is achieved through chemical vapor deposition. In the first step of CVD, the thin nanometer iron layer is sintered into nanoparticles at 700°C. Each nanoparticle acts as the seed particle for the self-assembly of a single CNT. Therefore, the efficiency of the sintering process in generating nanoparticles ultimately determines the packing density of the resulting array. After catalyst sintering, ethylene gas is flowed over the sample. At 700°C, ethylene gas dissociates, and the reactive carbon-containing subspecies are absorbed into the iron nanoparticles, which initiate the self-assembly process of the CNTs.

2.2.2 Photolithography (I)

A positive-tone photoresist (Shipley 1813, MicroChem, Newton, MA) is processed through photolithography to create a polymer mask for electron beam (e-beam) catalyst deposition. Silicon wafers are used as the underlying substrate for the process. To increase the adhesion of the photoresist to the silicon wafer, the surface of the wafer is treated with HMDS (hexamethyldisilazane) by placing the wafer in a sealed container with a small amount of liquid HMDS for 5 minutes. During this time, vapor from the HMDS deposits onto the wafer surface, forming a thin layer. Photoresist is dropcasted onto the wafer with a pipette, and immediately spin coated at 4,000 RPM for 60 seconds to create a uniform micrometer-thin resist layer across the wafer. After spin coating, the wafer is placed on a hot plate for 1 minute at 115°C. This soft baking process removes excess solvent from the photoresist solution.

A photomask is used to transfer the desired catalyst geometry to the photoresist layer. The pattern of the photomask is designed using a commercial CAD tool (AutoCAD 2012, Autodesk, San Rafael, CA) and printed onto a transparent plastic sheet through laser

photoplotting (CAD/Art Services, Bandon, OR). The minimum feature size that can be printed through this technique is approximately 10 µm. The transparency photomask is then attached to a 4" x 4" piece of soda lime glass to allow the photomask to be loaded into the mask aligner (MA6, Suss MicroTec, Sunnyvale, CA). The mask aligner aligns the photomask above the photoresist covered silicon wafer and exposes the sample to UV light. Exposure time is nominally set to 10 seconds.

Through UV exposure, the pattern inscribed in the photomask is transferred to the photoresist. Printed, or dark, areas of the photomask block UV exposure of the photoresist. UV light passes through transparent areas of the photomask and is absorbed by the photoresist. For positive-tone photoresist, as used here, the areas of the photoresist that were exposed to UV can be removed in the following step of photoresist development. In Chapter 3, a negative-tone photoresist will be utilized, which has the opposite effect. For negative-tone photoresist, areas of the photoresist that were *not* exposed to UV are removed during photoresist development.

Following exposure, the wafer is put through a post-exposure bake at 115°C for 60 seconds. To develop the photoresist, the wafer is immersed in a bath of a base developer for 5 minutes (MF-319 Developer, MicroChem, Newton, MA). Gentle agitation is applied to the bath to assist in dissolving exposed areas of the photoresist. After development, the wafer is rinsed in deionized water.

2.2.3 Catalyst Deposition (II)

At the end of the photolithography process, the silicon wafer is coated with a photoresist mask patterned in the desired catalyst geometry. An electron beam evaporator is used to deposit the catalyst and its supporting layers (Mark 40 Electron Beam Evaporator, CHA Industries, Fremont, CA). An optional silicon dioxide layer is deposited first, with 200 nm nominal thickness. Alumina is then deposited at 0.5 A/s, for a layer thickness of 10 nm. Iron catalyst is

deposited last, at 0.3 A/s, for a layer thickness of 1 nm. Alumina is a standard diffusion barrier to prohibit interaction of the iron with silicon. A physically deposited silicon dioxide layer was found to promote taller CNT array growth during chemical vapor deposition. Previous studies have postulated that the additional roughness and porosity in the support layers, as caused here by the presence of the deposited silicon dioxide layer, promotes optimal catalyst sintering and activity during nanotube fabrication (Amama et al. 2010).

After e-beam deposition, the photoresist mask, along with the undesired catalyst, is lifted off the silicon wafer by sonicating the wafer in acetone for 3 minutes, followed by an isopropanol rinse. The final result of patterned catalyst on a silicon wafer is shown in Figure 2.2. Catalyst patterning gives complete two dimensional control of the CNT pattern. Specifically for the application of hollow microneedles, catalyst patterning allows for control of the diameter of the microneedle, the diameter of the lumen, and the spacing between microneedles.
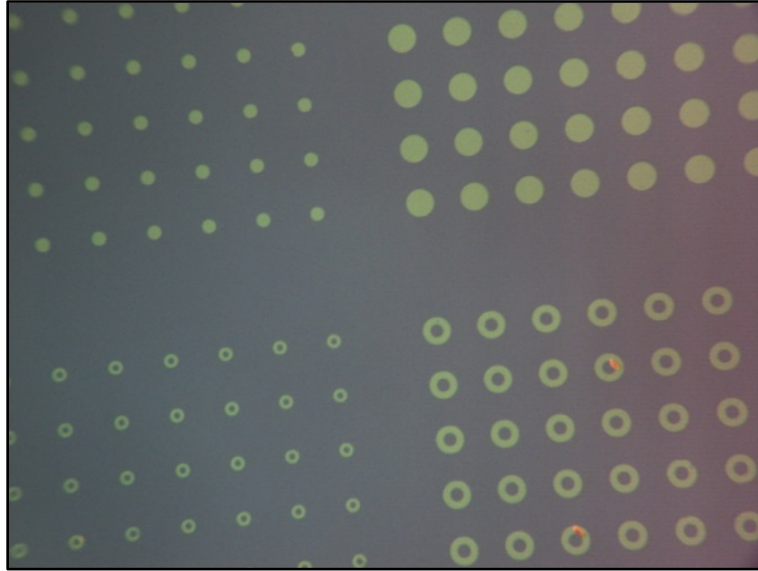
Figure 2.2- Catalyst patterned into 50 µm and 100 µm diameter circles on a silicon wafer.

2.2.4 CVD Fabrication (III)

Two custom thermal CVD furnaces were used in this study. The original furnace has a 1-inch diameter quartz process tube with a heated length of 12 inches, allowing for fabrication of approximately 8-16 CNT samples of dimensions 7 mm x 7 mm in a single run. A new furnace was built with a custom 4-inch diameter quartz process tube with a heated length of 36 inches, allowing for a maximum capacity of at least 6 silicon wafers of diameter 3 inches or at least 450 CNT samples of dimensions 7 mm x 7mm (Figure 2.3a). Samples were loaded and unloaded into the tube furnaces on custom quartz boats. Representative results from the 4-inch process tube furnace are illustrated optically in Figure 2.3b. For simplicity, these furnaces will be referred to simply by the diameter of the process tube, 1" and 4". Both CVD setups used commercial tube furnaces (Mini Mite Furnace [1"] & Split Hinge Three Zone Furnace [4"], Thermo Scientific, Waltham, MA).
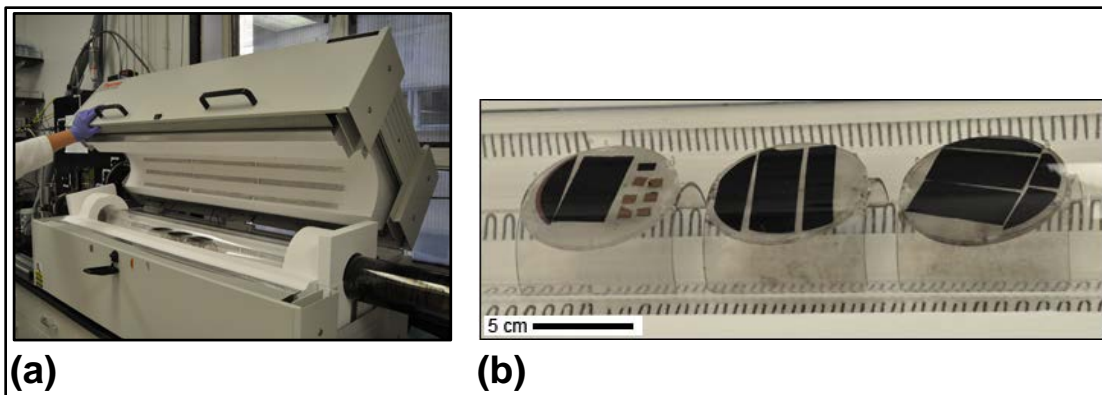
Figure 2.3- **(a)** 4" process tube furnace and **(b)** samples on custom quartz sample holders designed to hold 3" (76 mm) diameter silicon wafer.

Both the 1" and 4" furnaces were connected in parallel to the same gas storage and delivery system. Three high-purity gases were used for the CVD process, including argon (99.999% purity, Airgas, Radnor, PA), hydrogen (99.999% purity, Airgas, Radnor, PA), and

ethylene (99.95% purity, Matheson, Newark, CA). To ensure the quality of the feedstock gas used in the CVD process, the gas lines for ethylene, hydrogen, and argon are each individually evacuated and purged before every CVD process. The mass flow rate of each gas was controlled by a digital mass flow controller (πMFC, MKS Instruments, Fullerton, CA). The pressure in the CVD furnaces was controlled by a downstream pressure control (πPC, MKS Instruments, Fullerton, CA). A scroll vacuum pump (XDS 5, Edwards Vacuum, Sanborn, NY) is present downstream of the pressure controller to drive gas flow. The ultimate achievable vacuum of the system is 1 torr.

VA-CNT arrays fabricated in a single run of the 1" furnace demonstrated a wide variance in sample height on the order of hundreds of micrometers. A consistent pattern was observed where the sample height correlated to the position of the sample in the 1" furnace. Samples situated closer to the upstream end of the furnace were consistently shorter than samples situated closer to the downstream end of the furnace. Analysis of the gas flow during CNT growth revealed that the time for the gas to transverse across the heated length of the 1" furnace was less than 20 seconds. Thus, the temperature and composition of the gas were not uniform over the length of the process tube. To correct for this variance, the larger 4" furnace was constructed. The residence time of the gas during CNT growth for the 4" furnace was 10 minutes, ensuring a uniform gas temperature and composition throughout the volume of the process tube. As a result, the variance in CNT height between samples fabricated in the same CVD run was limited to 10 - 70 µm depending on the relative catalytic quality of the samples.

For the specific application of hollow microneedles, minimizing height variance is key in order to allow for the fabrication of consistent microneedle samples. For the specific microneedle geometry that is considered for this study, a target height of 250 µm to 300 µm was set for all CNT samples in the study. With the 1" furnace, the large height variance produced a small

sample yield of only 6-13% in the desired height range. In contrast, the 4" furnace had a sample yield of approximately 50%.

Process parameters for both the pretreatment and nanotube growth phases of CVD are given in Table 2.1 and Table 2.2 for the 1" and 4" furnaces respectively. The parameters of the 4" furnace were chosen to emulate the growth from the 1" furnace in terms of CNT diameter, packing density, and height. Details on the development and operation of the CNT fabrication procedure of the original 1" furnace are provided in previous work (Aria 2013). Here, focus is given on the development and operation of the 4" furnace, with comparison to the 1" furnace procedure as needed.

Parameter	Pretreatment	Growth
Temperature (°C)	750	750
Pressure (torr)	600	600
Argon (sccm)	200	-
Hydrogen (sccm)	285	210
Ethylene (sccm)	-	490
Process Time (min)	5	60

Table 2.1- CVD Parameters (1" Furnace)

Parameter	Pretreatment	Growth
Temperature (°C)	700	700
Pressure (torr)	600	600
Argon (sccm)	200	0
Hydrogen (sccm)	600	450
Ethylene (sccm)	0	300
Process Time (min)	5	60

Table 2.2- CVD Parameters (4" Furnace)

Samples are loaded into the 4" furnace using a custom quartz sample holder, allowing for samples as large as a 3" silicon wafer to be loaded into the furnace. Up to 6 quartz sample holders can be loaded into the furnace for a single process run. On the ends of the quartz process tube, custom quartz flanges were designed to allow for the process tube to be directly connected to the upstream and downstream piping by a stainless steel to quartz quick flange adapter (EVAC, Buchs, Switzerland). After closing the process tube via the quick flange connections, the furnace is pumped to its ultimate vacuum. Directly downstream of the furnace, a fan is placed underneath the process tube extruding from the furnace to accelerate the cooling of the gas. Following the termination of the process tube is a series of alternating water-cooled flanges and metal sieve traps (Nor-Cal Products, Yreka, CA) to cool the gas and remove precipitating hydrocarbon residue that may cause a blockage in the piping or damage the downstream pressure controller. The water-cooled flanges are connected to a chiller set to continuously deliver water through the flanges to maintain the temperature of the flanges at room temperature.

Delivery pressure from each gas supply is set to 15 psig for ethylene, hydrogen, and argon for the operation of the 4" furnace. The 4" furnace is heated to 700°C under an inert argon atmosphere of flow rate 500 sccm and pressure 600 torr. Catalyst sintering is achieved during the pretreatment phase. Upon reaching 700°C, hydrogen is introduced in addition to argon, with flow rates of 600 and 200 sccm respectively. Pressure is kept constant at 600 torr. The presence of hydrogen allows for the reduction of the iron catalyst, eliminating any naturally occurring iron oxides. The reduction of the iron catalyst increases the mobility of the catalyst, enabling it to sinter from the thin 1 nm catalyst sheet into a dense array of iron nanoparticles. Each iron nanoparticle acts as the seed particle for one carbon nanotube.

Following the five minute process time of pretreatment, CNT growth is initiated by introducing ethylene into the gas mixture simultaneous with the elimination of argon gas flow. The resulting ethylene and hydrogen gas mixture has an individual species flow rate of 300 and

450 sccm respectively. Process temperature and pressure are kept constant at 700°C and 600 torr respectively. During this process, the heat from the furnace causes the ethylene to dissociate, and the reactive carbon-containing subspecies are absorbed into the iron nanoparticles. The crystalline structure of the iron nanoparticle acts as a template for the self-assembly of carbon into carbon nanotubes.

At the very beginning of CNT growth, CNTs grow laterally along the surface of the substrate. Due to the high packing density of the CNTs achieved by the density of iron nanoparticles formed during pretreatment, the CNTs become spatially frustrated, causing the CNTs to intertwine and begin growing vertically above the substrate (Bedewy et al. 2009). The growth process is sustained for 60 minutes. Vertically-aligned CNTs reach typical heights in the range of 200 µm to 400 µm. This height range is selected specifically for the microneedle application investigated in this study.

In contrast to the ethylene-rich gas mixture used in the 1" furnace during growth, the gas mixture for growth in the 4" furnace is hydrogen-rich. Initial attempts to directly apply the parameters of the 1" furnace growth to the 4" furnace growth resulted in extremely short CNTs, with array height below 100 µm. The array was also covered with a thick coating of amorphous carbon, as could be directly visualized from SEM images. The presence of large amounts of amorphous carbon indicated that the process gas was too carbon-rich. The increase in gas residence time from 20 seconds in the 1" furnace to 10 minutes in the 4" furnace allowed for a higher rate of dissociation of ethylene than was observed in the 1" furnace. The overabundance of carbon caused the iron catalyst to become oversaturated with carbon, resulting in premature termination of CNT growth. The ratio of ethylene to hydrogen gas was progressively reduced, along with reduction of the furnace temperature, to reduce the abundance of reactive carbon species. The final resulting growth parameters reflect this transition, enabling sustained catalyst activity to allow for growth of CNTs in the desired height range.

At the end of the growth process, the ethylene and hydrogen gas flows are halted, and the furnace is kept in an inert argon atmosphere of flow rate 500 sccm and 600 torr while the furnace is cooled to room temperature. When the furnace temperature reaches 175°C, the argon gas flow is stopped, and the process tube is evacuated until the tube reaches its ultimate vacuum pressure. Upon reaching room temperature, a leak valve is opened to fill the process tube with air. After the process tube reaches atmospheric pressure, the samples are unloaded from the furnace.

2.3 Material Characteristics

SEM images of typical results from the CNT fabrication process are illustrated in Figure 2.4 (VP Field Emission SEM, Zeiss, Oberkochen, Germany). The patterned CNT structures conform exactly to the catalyst pattern, without any variation in cross-section geometry throughout the height of the pillar. CNTs are patterned into hollow cylinders with outer diameter of 150 µm with a central cavity, or lumen, diameter of 40 µm. The height of the cylinders is determined during the CVD growth process. Samples produced in the 4" furnace have a height in the range of 150 – 400 µm, with a high degree of height uniformity between samples produced in the same CVD process. Samples produced in the 1" furnace have a height in the range of 100–800 µm, with very little height uniformity between samples produced in the same CVD process.

From a macroscopic perspective, the CNT pillars appear to be solid, with perfect vertical alignment along the lateral surface of the pillars. On the nanoscale, the structure of the pillar is revealed to be porous, with an average nanotube to nanotube spacing of 50 nm, and a packing CNT density of 120-180 nanotubes per square micrometer. The general vertical growth direction of the nanotubes is still present at the nanoscale. However, the nanotubes do not grow perfectly vertical. Entanglement of neighboring CNTs, along with minor deviations in the lateral direction, is observed. In this way, the seemingly solid macroscopic vertically-aligned CNT structure is best described as a highly dense, nanoporous network of intertwined nanotubes.
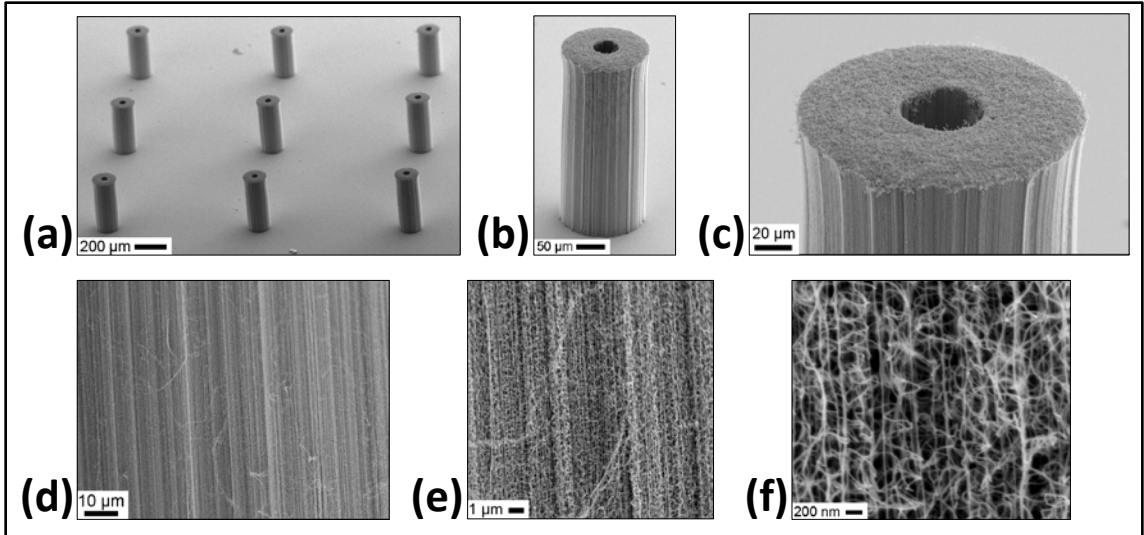
Figure 2.4- Multi-scale SEM images of CNT pillars ranging from **(a)** pillar array to **(f)** individual CNTs

2.4 Application to Hollow Microneedles

The preceding sections have introduced the general method of fabricating of vertically-aligned carbon nanotubes as well as the specific equipment, procedures, and results obtained in this study. Conceptually, the preceding sections provide a review of the current state of vertically-aligned CNT fabrication. From this perspective of common nanotube fabrication techniques, a discussion of the benefits and challenges of applying vertically-aligned CNTs is presented below.

2.4.1 Benefits

The primary benefit of using CNT structures for hollow microneedles over standard top-down approaches is the large degree of flexibility present in the bottom-up approach that can be applied to designing microneedle geometry. Through catalyst patterning, the size, shape, and spacing of vertically-aligned carbon nanotube microneedles can be varied arbitrarily. While the current mechanical requirements of transdermal drug delivery dictate the use of structures on the order of 100 µm, submicron VA-CNT scaffolds can be easily fabricated, if desired, using advanced lithography methods such as e-beam lithography or deep UV photolithography (Teo et

al. 2001). Chemical vapor deposition allows for the geometry of the microneedle to be fabricated in a single step.

1 mm generally represents the maximum length under consideration for microneedle architectures. A 1 mm maximum height ensures targeted delivery into the dermis layer of the skin while still minimizing pain associated with injection into deeper tissues (Gill et al. 2008). While a limited height range is investigated in this study, with a maximum microneedle length of 400 µm, the ability to grow CNT features more than 1 mm in length has been routinely demonstrated (Hasegawa and Noda 2011). In contrast, silicon microneedles are limited to heights below 1 mm since they are fabricated by etching silicon wafers that have a total thickness on the order of hundreds of microns.

2.4.2 Challenges

Many of the challenges of using CNTs for hollow microneedles are not unique to the application of hollow microneedles. While catalyst patterning allows for remarkable control over forming micro- and nano-scale CNT features, these patterns are generally restricted to use on the growth substrate, with few options available for transferring the patterns to other surfaces without inadvertently damaging the pattern. Techniques to anchor CNTs in silicone have been previously demonstrated, but do not allow for the option of preserving a clear lumen for hollow microneedles (Sansom, Rinderknecht, and Gharib 2008). CNT adhesion to the growth substrate is generally very weak, and the simple action of shearing the CNTs with a tweezers provides more than sufficient force to separate the CNTs from the substrate and destroy the vertically-aligned structure.

From the perspective of material strength and stiffness, patterned VA-CNTs alone cannot act as a microneedle. While under tension, individual carbon nanotubes have reported tensile strengths of up to 150 GPa (Yu et al. 2000). Due to this performance, CNTs have been commonly

proposed for use in extreme high-tension applications ranging from space elevators to tethers for formation flight satellites. However, under compression, the high aspect ratio of the CNTs (typically 20,000:1) makes the nanotubes prone to buckling (Figure 2.5), with an exceedingly low modulus under compression of only 550 kPa (Ci et al. 2008). Thus, the CNT microneedle alone cannot achieve skin penetration, regardless of the bulk microneedle geometry.
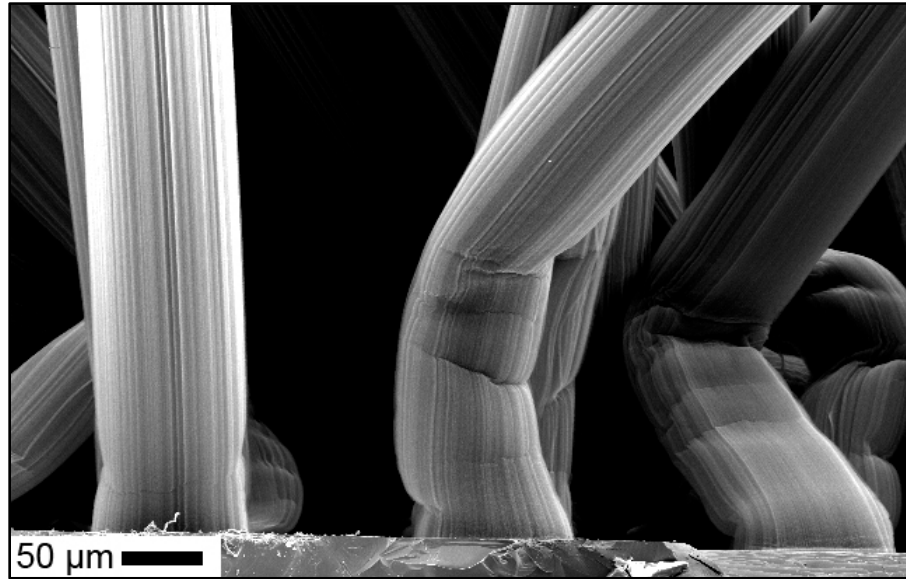
Figure 2.5- Base of buckled 100 µm diameter solid CNT pillar.

Another concern is the cost of fabricating CNTs, as well as the ability to scale-up the CVD process to an industrial level. The cost of producing multi-wall CNTs by CVD, currently at $100/kg, is considered cost prohibitive for many applications. However, the production capacity for CNTs has steadily grown in the last decade, with a 10-fold increase in production capacity since 2006 (De Volder et al. 2013). Previous work has also demonstrated the ability to integrate CVD into an assembly line process, allowing for continuous fabrication of vertically-aligned CNT samples that can further decrease the production cost of CNTs (de Villoria et al. 2009).

Carbon nanotubes and their sister material, graphene, are both fabricated through similar chemical vapor deposition processes. Specifically for graphene, CVD has been identified as providing the best monetary value for producing high quality graphene for electronic applications (Novoselov et al. 2012). The process for producing graphene by CVD is much more challenging than producing VA-CNTs, as the desire to reproducibly fabricate monolayer graphene depends on a thorough understanding of the kinetics of carbon absorption and desorption into the catalyst. Therefore, the continued study of CVD for both CNT and graphene will result in the long-term optimization of the technique, resulting in increased product yield and reduced operation costs.

Chapter 3

Microneedle Fabrication

3.1 Introduction

Using the catalyst patterning techniques from Chapter 2, vertically-aligned CNTs (VA-CNTs) can be patterned into almost any arbitrary geometry of constant cross-section. Additionally, the chemical vapor deposition (CVD) process for fabricating CNTs allows for microneedle to be constructed up to 1 mm in height. The advantage of the bottom-up approach is that the geometry of the entire microneedle, including the lumen, is defined in a single step of CVD. This creates a direct path for producing microneedles that is not present in other top-down approaches for fabricating hollow microneedles.

Here, the bottom-up approach is leveraged for fabricating CNTs and developing a novel approach to creating fully functional microneedles by creating a CNT-polymer composite microneedle. Polymer resins are used to infiltrate the porous CNT pillars through capillary action. After infiltration, the polymer is then subsequently cured to create the CNT-polymer composite structure. Previous studies have demonstrated the fabrication of micropatterned VA-CNT-polymer composites by using matrices of poly(dimethylsiloxane) (PDMS) and epoxy (Jung et al. 2006) (De Volder et al. 2010). In this work, these general concepts are extended to demonstrate that a composite of patterned VA-CNT and polymer can be used to directly fabricate an array of hollow microneedles.

In order to fabricate a functioning CNT-polymer composite microneedle and overcome the challenges delineated in Section 2.4, the following requirements for the CNT-polymer composite microneedle are defined:

(I) The resulting CNT-polymer composite must withstand the forcing required to achieve skin penetration.

(II) The lumen must be clear after processing and open at both ends.

(III) A thick polymer base (>25 µm) is required to unite the microneedles onto a single anchoring substrate.

(IV) The aforementioned polymer base allows for the microneedle array to be separated from the native silicon substrate.

(V) The approach is scalable for a large number of microneedles.

To satisfy Requirement I, polymers are used with an intrinsic stiffness greater than 1 GPa, which is considered sufficient to support skin penetration (Park, Allen, and Prausnitz 2005). Here, two families of polymer are considered, SU-8 epoxy and polyimide, which have a stiffness of 3 GPa and 2.5 GPa respectively (Microchem) (Jiang, Bin, and Matsuo 2005). Requirement V is important for the express application of hollow microneedles. With the goal of microneedles to provide an architecture that can be widely distributed to a large number of patients, it is important that the fabrication approach minimizes unnecessary fabrication costs to ensure that microneedles can be manufactured quickly and cheaply without issue of scale. Assuming that the bulk of the fabrication complexity and cost is tied to fabricating the CNT pillar, the additional methods to convert the CNTs into microneedles will focus on passive techniques that do not require *in stiu* control during processing in order to minimize additional fabrication complexity and cost. Generally, all of these objectives are interdependent, and thus careful choice of polymer must be

applied to create a functioning microneedle. For instance, the use of high viscosity polymer resins may easily create a thick polymer base. However, the slow transport of a highly viscous resin will also increase the difficulty of clearing the lumen.

3.2 Materials & Methods

3.2.1 Process Overview

Figure 3.1 outlines the microneedle fabrication process. Catalyst patterning and VA-CNT fabrication together create a CNT scaffold that defines the geometry of the microneedle, including the cross-sectional geometry and height (Step 1 & 2). Polymer resin is then dropcasted onto the CNT array and immediately spin coated (Step 3). Dropcasting is performed with a pipette and completely covers the CNT pillar array. In order to comply with Requirement V, resin is purposely applied in this manner such that there is no active control of the resin application.
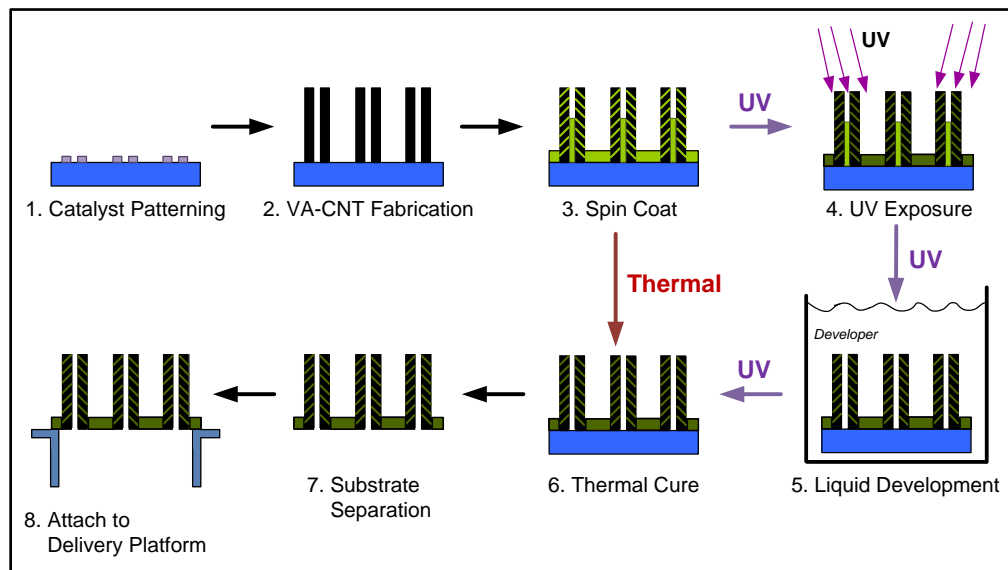
Figure 3.1- Microneedle fabrication schematic for thermal curing of thermoset polymer resins and selective UV curing of negative tone photoresists.

During spin coating, several actions occur simultaneously. Polymer resin wicks into the CNT scaffold to create a CNT-polymer composite (Figure 3.2). On the outer surface of the CNT scaffold, the polymer resin conformally coats the scaffold, allowing for the geometry of the scaffold to be preserved in the resulting microneedle. The remaining polymer resin creates a polymer base that unites the microneedles on a single platform. For some polymers, the lumen is completely clear of polymer after spin coating due to the high rate of capillary uptake into the CNT scaffold. For other polymers, the lumen is clogged after spin coating. A model for predicting which polymers will leave the lumen clear after spin coating is discussed in Chapter 4.
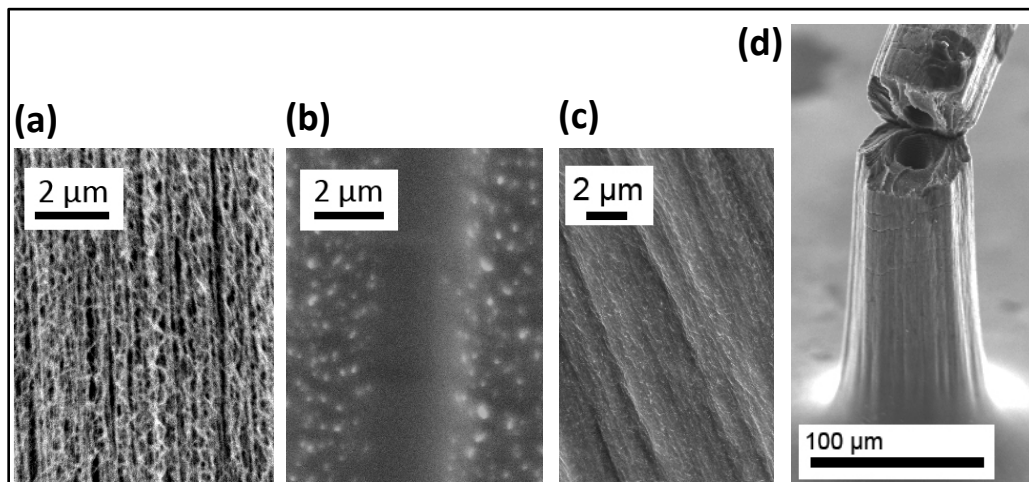
Figure 3.2- Structure of **(a)** CNT, **(b)** CNT-SU-8 2025 **(c)** CNT-BOPDA polyimide, **(d)** Broken CNT-BOPDA microneedle demonstrating full penetration of the polymer resin through the microneedle while not obstructing the lumen.

For thermoset polymer resins that passively clear the lumen during spin coating, the resin can be immediately heated to cure the composite and the polymer base (Step 6). For polymer resins that clog the lumen, a new approach, CNT Masked Photolithography, has been developed that uses a modified photolithography scheme to clear the lumen and selectively cure different

segments of the polymer by UV exposure (Step 4 & 5). For the selective UV curing process, utilizing CNT Masked Photolithography, the type of polymer is restricted to negative-tone photoresists. Negative-tone photoresists act in the opposite manner as positive-tone photoresists, as described in Chapter 2 and Figure 2.1. Negative-tone photoresists require UV exposure to cross-link polymer chains and solidify the polymer. Otherwise, polymer not exposed to UV is washed away during development.

For CNT Masked Photolithography, the sample is selectively cured under oblique incidence UV light (UV/Visible Light Exposure Chamber, MTI Corp., Richmond, CA) (Step 4). CNTs are commonly considered to be the world's darkest material due to their high light absorbance (Mizuno et al. 2009). The high UV absorbance of CNTs allows CNTs to be used as a masking element to shield the polymer resin in the lumen from UV exposure. Utilizing oblique incidence minimizes UV radiation entering the lumen from the top surface of the microneedle. The polymer base is directly exposed to UV radiation and is cross-linked. A high dose of UV is used, consistent with previous studies, to compensate for attenuation of UV light in the CNT scaffold to ensure at least partial cross-linking of the polymer resin within the CNT scaffold (De Volder et al. 2010). A hard bake process after development ensures that the polymer in the scaffold is fully cured.

After UV exposure, the microneedles go through a brief post-exposure bake to conform to the prescribed photolithographic process for the photoresists. The microneedle sample is then immersed in developer solution, which clears the uncured photoresist from the lumen while leaving the UV exposed resin in the scaffold and base untouched. (Step 5). To aid in clearing the lumen, the immersed sample is placed on a shaker table during development. After development, the sample is rinsed to stop development. Samples are then thermally cured to solidify all polymer resin that remains in the samples (Step 6).

After thermal curing the samples, the remainder of the fabrication process is the same for both the thermal cured and selective UV cured samples. The microneedle array can be removed from the silicon substrate, since the microneedles are anchored together in the cured polymer base (Step 7). The polymer base is macroscopically thin, 25 - 50 µm, and flexible. In this thickness range, it can be handled easily by tweezers without risk of tearing. In every testing instance, there have been no observations of tearing or other flow induced damage of the polymer base. For polymer bases thinner than 25 µm, the bases were unable to mechanically support the microneedle array during substrate separation and general handling of the array. For polymer bases thicker than 50 µm, the reduction in the height of the microneedles becomes prohibitive. After peeling the microneedle array from the silicon substrate, the polymer base can be cut cleanly with a razor blade to subdivide the array or reduce the base area.

Substrate separation is achieved by simple, mechanical means. Either a tweezers or razor blade can be used to peel the polymer base away from the substrate. This is achieved by generally choosing polymers that have poor adhesion to silicon dioxide, which comprises the top layer of the silicon substrate. Additionally, full curing of the polymer base minimizes adhesion of the polymer to the substrate. In some instances, a sacrificial layer, such as gold, which has poor adhesion to silicon dioxide, can be deposited after CNT fabrication (Step 2) of thickness 50 – 100 nm to ease in separation. Due to the nanometer thickness of the sacrificial layer, the additional deposition conformally coats the outer layer of the CNT scaffold without interfering in the capillary uptake of polymer resin.

After substrate separation, the lumen of the microneedle can be inspected from the underside to verify that the lumen is clear (Figure 3.3). Specifically for the selective UV process, the bottom of the lumen represents the most difficult point to clear polymer resin during development. A clogged lumen for the selective UV process would indicate that a longer development time is necessary. At this point, the fabrication of the microneedle array is complete,

and the array can be transferred to any given delivery platform (Step 8). In Chapter 5, performance of the microneedles on specific delivery platforms will be discussed.
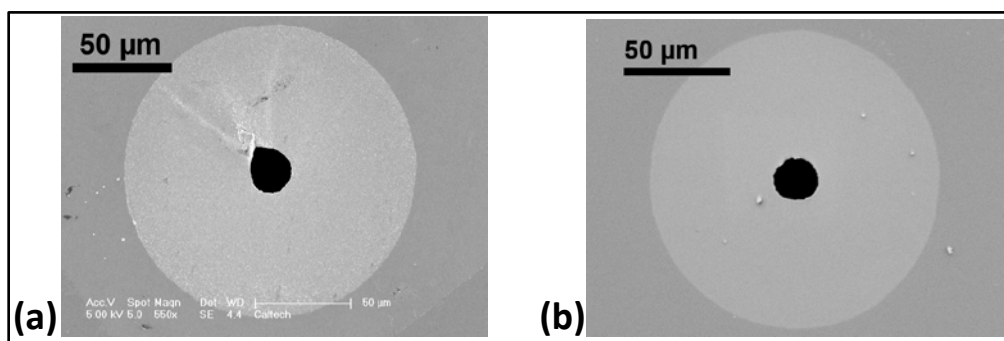
Figure 3.3- Underside of (a) SU8 2025- CNT and (b) BOPDA-CNT microneedles on polymer base showing clear lumen after substrate separation.

3.2.2 Thermal Cured Polymers

3.2.2.1 SU-8 2002, SU-8 2010

A previous study has shown that low viscosity formulations of SU-8, such as SU8-2002 and SU8-2010 (MicroChem, Newton, MA), can be spin coated on VA-CNTs to create a composite (De Volder et al. 2010). However, the thin film created by these resists through spin coating (2µm and 10µm for SU-8 2002 and SU-8 2010 respectively) is too fragile for making a structurally supportive base for the microneedles. These polymers are listed to illustrate the thermal technique.

These polymers are capable of being cured using the thermal technique. For these polymers, UV curing is used as part of the thermal technique to fully cross-link the polymer. However, these polymers are classified as thermal cured rather than the selective UV curing technique because the high wicking speed of these resists leaves the lumen cleared, negating the

need to develop and selectively etch away polymer resin left in the lumen. Thus, it is more closely classified as thermal cured with an additional step of UV curing only to ensure proper cross-linking of the polymer.

For both polymer variants, SU-8 is dropcast and spun on the sample at 3,000 RPM for 60 seconds. The samples are then soft baked on a hot plate at 95°C for 3 minutes/10 minutes for SU-8 2002/2010 respectively. The sample is exposed to oblique incidence UV light for 2 minutes/ 5 minutes at 30 mW/cm^2 (UV Exposure Chamber, MTI Corporation, Richmond, CA). Next, the samples are put through a post-exposure bake on a hot plate for 10/20 minutes at 95°C. Finally, the sample is hard baked at 150°C in a vacuum oven for 24 hours (VWR Signature Vacuum Oven, VWR, Radnor, PA).

3.2.2.2 BOPDA Polyimide

Poly(3,3′,4,4′-**b**enzophenonetetracarboxylic dianhydride-co-4,4′-**o**xydianiline/1,3-**p**henylene**dia**mine) (Sigma-Aldrich, St. Louis, MO), or BOPDA for short, is used as the polyimide resin. After dropcasting, the sample is spun at 1,000 rpm for 60 seconds. After spin coating, the polyimide is thermally cured using a four-step temperature ramp from 100°C to 250°C. The sample is placed on a hotplate for 100°C for 1 hour, followed by 30 minutes at 150°C, and an additional 30 minutes at 200°C. The sample is then moved into a vacuum oven at 250°C for 4 hours. The gradual temperature ramp is designed to ensure proper curing of the polyimide and prevent the polyimide from becoming brittle.

3.2.3 Selective UV Cured Polymers

3.2.3.1 SU-8 2025

In contrast to SU-8 2002 and SU-8 2010, the high viscosity of SU8-2025 (MicroChem, Newton, MA) causes the lumen to become clogged, necessitating the selective UV curing

method. The epoxy resin is dropcast, and the sample is spin coated at 3,000 rpm for 60 seconds. The sample is then soft baked at 95°C on a hot plate for 4 minutes. The sample is then exposed to UV light at 30 mW/cm^2 for up to 1 minute. Post exposure bake is performed for 3 minutes at 95°C. The microneedles are then submerged in SU-8 Developer to clear the uncured photoresist from the inner cavity (MicroChem, Newton, MA). The submerged sample is placed on a shaker table set to 150 rpm for 10 minutes. Following development, the sample is rinsed in isopropanol and cured in a vacuum oven at 150 °C for 20 minutes (Lyon, Aria, and Gharib 2013(a)). In contrast with SU-8 2002 and 2010, SU8-2025 was exposed to a lower total UV dose. This is because for exposure times greater than 1 minute, the epoxy resin in the lumen begins to cure, making the resin less responsive during development, leading to a permanently blocked lumen.

3.2.3.2 HD-4110

HD-4110 is a negative tone UV-curable polyimide resin (HD MicroSystems, Parlin NJ). After dropcasting the resin, the sample is spin coated at 1,500 rpm for 60 seconds. Soft bake is performed on a hot plate at 90°C for 2 minutes. The sample is then exposed to UV radiation for 5 minutes at 30 mW/cm^2. In substitution of a post-exposure bake, the sample is simply held at room temperature for 5 minutes before development to conform to the suggested photolithographic parameters of the resin's process data sheet. The sample is immersed in the developer solution, PA-401D, for 3 minutes (HD MicroSystems, Parlin NJ). For the duration of development, the immersed sample is placed on a shaker table at 150 rpm. After development, the sample is rinsed in PA-400R (HD MicroSystems, Parlin NJ). The sample is hard baked at 150°C in a vacuum oven for up to 24 hours.

3.3 Results

While the diameter and height of CNT scaffolds in general can be greatly varied through catalyst patterning and CVD as described in Chapter 2, a specific subset of geometries is used for producing the most advantageous microneedle design in terms of mechanical strength of the needle, suitable deliverable drug volume, and the goal of painlessly delivering drug past the outermost layers of skin, the stratum corneum, and into the epidermis. Results from both the selective UV and the thermal curing methods are demonstrated in Figure 3.4. For all of the polymers described in the previous section, BOPDA polyimide of the thermal curing technique and SU8-2025 & HD-4110 polyimide of the selective UV curing method were found to fulfill all of the fabrication requirements introduced at the beginning of the chapter. SU8-2002 and SU8-2010 had maximum base thicknesses of 2 µm and 10 µm, respectively, and were not able to consistently achieve substrate separation.

The height of the VA-CNT scaffolds is set between 250 µm and 300 µm. Since the needles are now attached to a common polymer base, the working height of the microneedles is reduced to 200 – 250 µm (Figure 3.4 c-h). In this range, the microneedles provide enough depth for skin penetration, while also minimizing the pain associated with the injection (Haq et al. 2009). The average thickness of the human stratum corneum and epidermis layers is 10–20 µm and 50–100 µm, respectively (Prausnitz, Mitragotri, and Langer 2004). Microneedle heights below 200 µm were found to be too short to achieve consistent skin penetration. To facilitate equitable delivery of drug through each microneedle, the height of the microneedles in a single array must be uniform. By utilizing the increased sample uniformity achieved by using the larger 4" diameter quartz tube furnace described in Chapter 2, the average standard deviation in the height of the microneedles in a single array is 9 µm.

Method	Needle	Array	Substrate Separated
As Grown CNT	(a)	(b)	
CNT Masked Photolithography *(Selective UV Curing)*	(c)	(d)	(e)
Thermal Curing	(f)	(g)	(h)
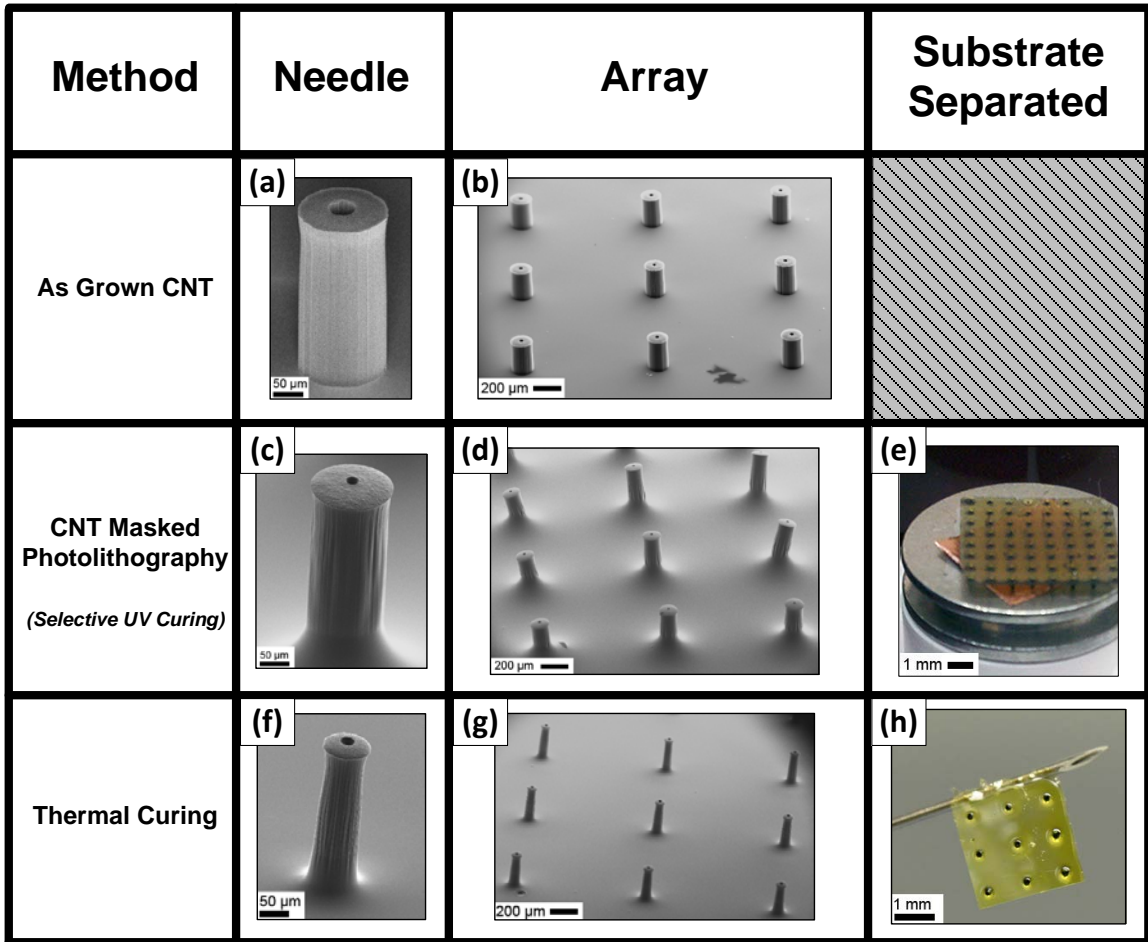
Figure 3.4- Summary of microneedle results. **(a), (b)** 3x3 CNT scaffold of outer diameter/ lumen diameter 150/40 µm. **(c), (d)** CNT-SU8-2025 microneedles of 150/25 µm. **(e)** Underside of CNT-HD-4110 microneedles peeled from substrate. **(f), (g)** CNT-BOPDA microneedles produced from same CNT scaffold pattern as (a), (b). Microneedles illustrate significant shrinkage due to capillography effect. **(h)** CNT-BOPDA microneedles separated from the substrate hanging on a 30 gauge hypodermic needle.

VA-CNT scaffolds were patterned as cylinders with 150 µm outer diameter and lumen diameter ranging from 25 µm to 50 µm. Of particular interest for the CNT-BOPDA polyimide microneedle is the overall shrinkage of the diameter of the microneedles after thermal curing. The initial VA-CNT scaffold had an original outer diameter of 150 µm with a 40 µm diameter lumen. After thermal curing, the diameter of the microneedle reduces to 100 µm outer diameter and 30 µm lumen diameter (Figure 3.4 a,b & f,g). This phenomenon, known as capillography, has been

seen previously by introducing a volatile liquid such as water or isopropanol into the interspacing of the carbon nanotubes (De Volder et al. 2010) (Huang et al. 2007). As the solvent in the polyimide resin evaporates, the resin contracts, pulling the carbon nanotubes closer together.

For the CNT-BOPDA polyimide microneedles, capillography reduces the area of the microneedle tip by 56%. Capillography reductions in microneedle size were not observed for CNT Masked Photolithography polymers. The polymers used for CNT Masked Photolithography depend on UV curing rather than thermal curing, and thus are generally less volatile. The reduction in size of the CNT-BOPDA polyimide microneedles compared to the as grown CNT scaffold and the microneedles produced from the CNT Masked Photolithography method can be seen in Figure 3.4.

The microneedles are spaced 1 mm apart such that the deformation of skin from one microneedle does not interfere with the skin contact of the surrounding microneedles (Burton et al. 2011). The base of the microneedle array is macroscopically thin and flexible. In the configuration used for *in vivo* testing, 9 microneedles are arranged in a 3 x 3 grid. The microneedle array is centered on a 1 cm x 1 cm polymer base, but only takes up an area of 0.2 cm x 0.2 cm. The oversized base allows for sufficient contact area for adhering the microneedles to a variety of delivery platforms, as will be discussed in Chapter 5.

The resulting CNT-polymer microneedle acts mechanically as a single solid structure rather than a network of individual nanotubes, eliminating the failure mode of buckling by individual nanotubes as seen in Chapter 2. The stiffness of the CNT-BOPDA composite was measured as 2.75 ± 0.48 GPa through atomic force microscopy (Dimension Icon AFM, Bruker Corporation, Fremont, CA) with a spatial resolution of 20 nm (Figure 3.5). Compared to the stiffness of the BOPDA polyimide alone, 2.5 GPa, the incorporation of the VA-CNTs does not significantly enhance the stiffness of the material as has been reported in similar nanotube-

polyimide composites (Jiang, Bin, and Matsuo 2005). Instead, the primary motivation for using VA-CNTs is to act as a scaffold to directly create the high-aspect ratio geometry necessary for hollow microneedles. The polymer matrix provides the majority of the mechanical strength of the composite.
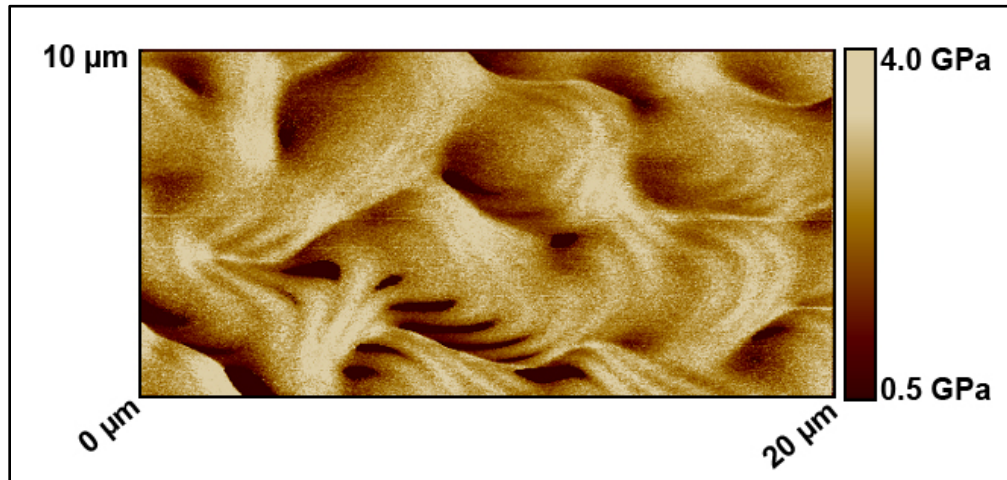
Figure 3.5- Elastic modulus of CNT-BOPDA polyimide microneedle mapped by AFM

Previous studies have demonstrated the use of spin coating and polymer curing to create composites with vertically-aligned carbon nanotubes. The ability to clear a center cavity was achieved using less viscous polymer solution including SU8-2002 (De Volder et al. 2010). However, the low viscosity of the polymer solution does not allow for the creation of a mechanically supportive base. Here, this study is the first to show that this technique can be applied to fabricate functioning microneedles, including the feature of substrate separation. The key to creating functioning microneedles is proper selection of the polymer in order to satisfy the five aforementioned microneedle requirements.

3.4 Fabrication Method Discussion & Comparison

The strength of the fabrication process presented herein lies in its simplicity. By properly choosing the polymer to achieve the mechanical requirements of the microneedle, the fabrication process becomes remarkably simple over the current top-down approaches for hollow microneedles. Thus, this simplification in fabrication expands the range of potential applications and commercial opportunities for hollow microneedles. It is anticipated that this technique is not limited to the polymers described here. Generally, other thermoset polymers of similar viscosity would be viable polymer candidates, as will be described in Chapter 4.

One of the key advantages of the bottom-up approach is that the minimum feature size that can be fabricated is much smaller than what can be attained through conventional top-down approaches. By fully exploring the different combinations of nanotube-polymer composites, it may be possible to further shrink the diameter of the microneedle by up to an order of magnitude without putting any constraints on the fundamental fabrication process. The advantage of reducing the diameter of the microneedle is to increase the packing density of microneedles on a delivery platform. As photolithography becomes more complex at smaller length scales, capillography provides a simple method to further reduce the size of the microneedle without complicating the lithography processes. Additionally, oxygen etching, as introduced in Chapter 7, provides an alternative framework for further shrinking the size of CNT scaffolds beyond what has been achieved with capillography. Using this fabrication approach, VA-CNTs would stand alone from the current top-down fabrication methods in being able to extend hollow microneedles into smaller feature sizes.

CNT-polymer composite microneedles can potentially be fabricated to reach heights taller than 1 mm through CVD techniques (Hasegawa and Noda 2011). In contrast, silicon microneedles are etched from a silicon wafer. Therefore, the combined height of the silicon

microneedles and the thickness of the base supporting the microneedles is restricted to the total thickness of the silicon wafer, which typically ranges from 300-1,000 µm. Micromolding approaches using top-down fabricated master structures have reached heights in the range of 500 µm to 1 mm (Burton et al. 2011; Norman et al. 2013) at the expense of relatively large base diameters on the range of 200-500 µm, which reduces microneedle packing density. As the aspect ratio of the CNT-polymer composite microneedles is increased, to either increase the height of the needles or to reduce the feature size, a taper may need to be utilized to mechanically support the microneedle during skin penetration. The CNT-polymer composite process can be combined with other methods to create more complex geometry. Focused ion beam (FIB) milling has been shown to modify the geometry of CNTs on the nano-scale (Krasheninnikov and Banhart 2007). However, the use of FIB would be difficult to scale for CNT bundles, let alone large arrays of microneedles, and runs counter to the passive, scalable approach used thus far. Alternatively, capillography or oxygen etching, as will be demonstrated in Chapter 7, can be used to passively fabricate more complex geometry that may be advantageous for microneedle performance.

The thin, flexible polymer substrate created by this methodology is unique to other hollow microneedle architectures. The minimalist base increases the number of drug delivery architectures that can be potentially utilized. By being able to curve or deform the base, the microneedles can potentially make better contact with the skin during drug delivery. Another potential application is to attach microneedles to balloon like platforms, like a balloon catheter, such that the polymer base allows for accommodation or incorporation of an expanding structure (Lyon et al. 2014).

Fabrication of both silicon and CNT-polymer microneedles offers similar advantages in terms of geometry customization and parallel processing of large numbers of microneedles. In characterizing the fabrication process for silicon microneedles, reactive ion etching (RIE) is generally the primary method for defining the microneedle shape, with additional processes such

as wet etching or micromachining used as secondary methods to optimize the microneedle geometry (Kim, Park, and Prausnitz 2012; Gardeniers et al. 2003; Ma et al. 2006; Yu et al. 2009). Figure 3.6 compares the fabrication process of CNT-polymer microneedles to silicon microneedles produced by a generic RIE procedure. For producing hollow silicon microneedles, RIE is commonly performed on silicon wafers in three iterations. The first iteration defines the outer geometry of the needle. In the second iteration, the wafer is etched from the back side to create the lumen. The third iteration is used to optimize the geometry and to open the lumen on the top of the microneedle. Fine alignment of the wafer must be maintained between the three etching cycles to ensure that the lumen is aligned with the external shape of the microneedle.
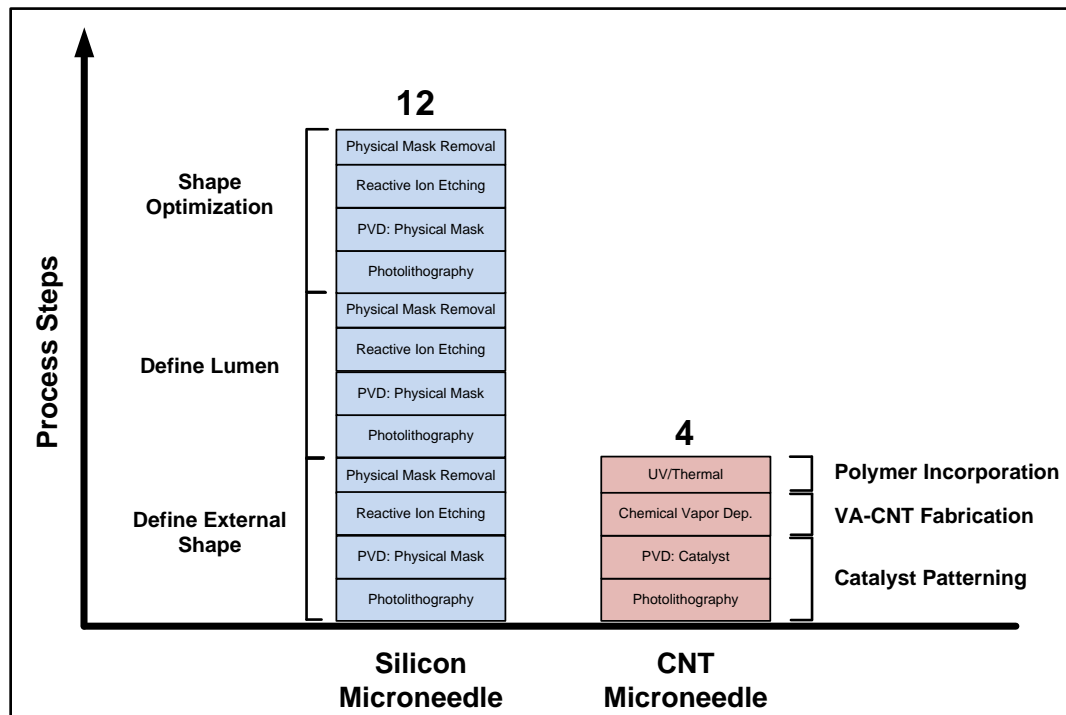
Figure 3.6- Comparison of fabrication process for silicon and CNT-polymer microneedles

In comparing the fabrication sequences, silicon microneedles in general require three times the number of processing steps compared to CNT-polymer microneedles, showing that the CNT-polymer method has the potential to be significantly simpler than the silicon approach. This is because creating a hollow cavity in the silicon approach requires multiple etching iterations, which in turn require multiple processing steps for each iteration. In contrast, the entire geometry of the CNT-polymer needle is defined from the sequential steps of catalyst patterning, nanotube fabrication, and polymer incorporation without. Another important consideration in the CNT-polymer approach is that incorporation of polymer resin on the CNT scaffold relies on a combination of simple and passive mechanisms such as capillary action, thermal curing, and UV exposure that can be easily executed on both the laboratory and industrial level. The primary fabrication challenge for the CNT-polymer microneedle is the fabrication of VA-CNTs. However, as discussed in Section 2.4, the increasing production capacity for fabricating CNTs, along with continued basic research into the CVD process, is projected to lower the overall fabrication difficulty and improve scalability in the long run.

Micromolding is another common approach to producing hollow microneedles by electroplating micromolds to produce a hollow metallic microneedle. Typical master structures for micromolding are fabricated by micromachining or laser drilling of a bulk material, which can be time consuming and ultimately limits the minimum feature size of the needle (Kim, Park, and Prausnitz 2012; Norman et al. 2013). However, after the master structure is complete, the micromolding process allows for fast fabrication of large numbers of microneedles. Both the silicon and CNT-polymer microneedle can achieve a much finer feature size than micromachining and laser drilling, and thus both can be potentially used as a master structure for micromolding. A previous study has demonstrated the successful use of CNT-SU8 composites for general micromolding applications (De Volder et al. 2010).

3.5 Conclusions

A new approach to fabricating hollow microneedles has been presented using a vertically-aligned carbon nanotube-polymer composite. By using VA-CNTs as a scaffold for creating the shape of the microneedle, simple and scalable techniques can be used to directly convert the scaffold into a working microneedle device. The polymer gives the microneedle its mechanical strength, and creates a common base for the microneedle array. The thin, flexible polymer base is a unique feature to the CNT-polymer microneedle, and increases the number of potential drug delivery platforms to which the microneedles can be applied. Both the thermal and selective UV approach can be applied to an arbitrary number of microneedles in parallel, allowing for these methods to be incorporated in future commercial manufacturing processes.

In comparing the fabrication of CNT-polymer composite microneedles with other approaches, the CNT-polymer fabrication method is potentially simpler than that of silicon microneedles. CNT-polymer composites may also be incorporated as master structures for micromolds to allow for rapid development of microneedles with characteristic feature sizes on the order of several microns. Further work to incorporate other polymers into the thermal and selective UV fabrication procedures can lead to a wide range of possibilities to expand the CNT-polymer composite architecture.

Chapter 4

Analysis of Thermoset Fabrication of Microneedles

4.1 Introduction

In Chapter 3, two methods for producing CNT-polymer composite microneedles were introduced: thermal curing of a thermoset polymer and selective UV curing of a negative-tone photoresist polymer. Here, an investigation of the fluid transport properties of the polymer resin in forming the microneedle composite is undertaken to determine how to expand the fabrication techniques from Chapter 3 to a wider range of polymers. The immediate goal of this study is to develop a set of requirements that can allow for screening of an arbitrary thermoset polymer resin as to whether or not the resin can be successfully incorporated into a CNT-polymer composite microneedle.

The ability to adapt the CNT-polymer composite fabrication method to a variety of polymers is advantageous for the general advancement of the technology. Incorporation of stiffer polymers, such as polyamide-imides, can allow for higher aspect ratio microneedles. In the field of dissolving microneedles, many new combinations of drugs embedded in degradable polymers are being developed (Kim, Park, and Prausnitz 2012; Fukushima et al. 2011). Incorporation of a partially dissolving polymer in the CNT scaffold could allow for a CNT-polymer hollow

microneedle to simultaneously deliver multiple drug species in parallel by both luminal transport and polymer degradation.

Table 4.1 lists the primary requirements for the CNT-polymer composite microneedle and the subsequent material data that are required for screening a candidate polymer. "Scalable Process" refers to a method that can process a large number of needles in parallel. In essence, this requirement is satisfied by the fabrication steps outlined in Chapter 3 and is not necessarily a constraint on polymer choice. However, failure of a polymer to satisfy the first four requirements would require additional processing steps that may ultimately reduce process scalability.

Microneedle Requirement	Required Polymer Data
Skin Penetration	Polymer stiffness greater than 1GPa
Clear Lumen	Thermoset Polymer: $\sigma/\mu > 1$ cm/s Negative Photoresist: Photolithography Process Data Sheet
Common Polymer Base	Polymer Spin Speed Curve Base thickness $> 20\ \mu$m
Substrate Separation	Poor adhesion between polymer and substrate
Scalable Process	-

Table 4.1- Polymer requirements for microneedle fabrication.

As discussed in Chapter 3, the stiffness of the composite is derived primarily from the polymer matrix, with the CNTs contributing very little to the mechanical rigidity of the structure under compression. With this in mind, the stiffness of the polymer should be greater than 1 GPa (Park, Allen, and Prausnitz 2005). A common polymer base that is capable of being separated from the silicon substrate requires that a polymer can be spin coated to a thickness greater than 20 μm. This data is readily available from a polymer resin's spin speed curve, which relates the film thickness of the resin to the rotation speed during spin coating. The range of possible film

thickness that can be achieved through spin coating depends primarily on the viscosity of the polymer (Scriven 1988). Poor adhesion between the polymer and substrate must be present to guarantee a clean separation. This can be achieved either by the naturally poor surface interaction between the polymer and substrate, or by introducing a sacrificial layer such as a gold layer to reduce adhesion.

To cure the lumen for the selective UV curing method, the process parameters are largely adapted from the general photolithography protocol for the material, including an estimate of UV dosage as well as types of developers and rinses to be utilized during the process. This data is readily available from reference material, including material and process data sheets. For most commercially available photoresists, this material is made available to application developers by the photoresist manufacturer.

For the thermal curing method for thermoset polymers as presented in Chapter 3, there is no obvious guideline or requirement to ensure that the polymer is compatible with the passive wicking method for clearing the lumen. Here, analysis of the transport of polymer resin during dropcasting and spin coating will be presented to motivate the utility of a characteristic wicking speed, defined as the ratio between a fluid's surface tension, σ, and viscosity, μ. The characteristic wicking speed will be applied as a quantitative criterion to determine whether or not a polymer can reliably produce a clear lumen by the thermal curing process.

4.2 Capillary Action Through Vertically-Aligned Carbon Nanotubes

4.2.1 Introduction

The first objective of this study is to determine a model for describing the transport of polymer resin through the network of vertically-aligned carbon nanotubes. Previous work has demonstrated that the Washburn model of capillary action (Washburn 1921) can be used to describe the transport of aqueous solutions as well as more viscous polymer resins through a network of vertically-aligned CNTs (Zhou 2005).

The Washburn model describes capillary flow, or wicking, through a cylindrical hollow tube of infinite length (Figure 4.1).
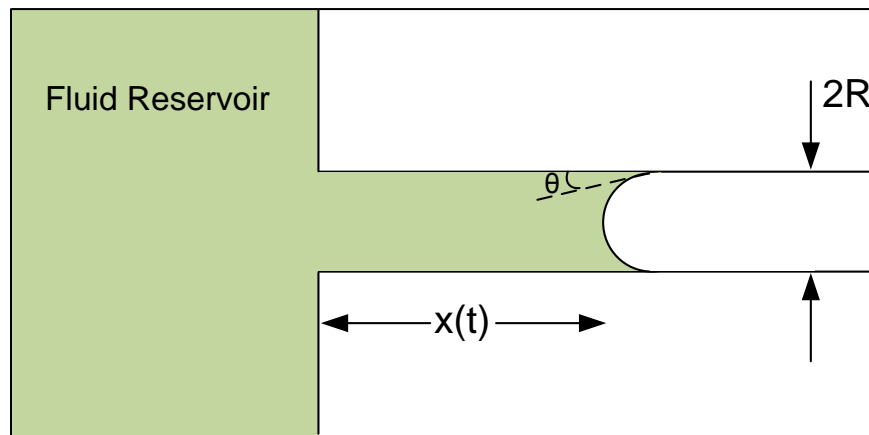
Figure 4.1- Setup for Washburn flow through a capillary tube from a large fluid reservoir

Fluid enters the capillary tube of diameter *2R,* with the location of the fluid front at time *t* described by *x(t)* as the distance of the fluid front from the opening of the capillary tube. The dynamic contact angle, θ, is dependent on the flow rate through the capillary (Joos, Van Remoortere, and Bracke 1990). The Washburn model is derived assuming a Poiseuille flow

through the capillary, where the pressure gradient is given by the capillary pressure as determined by the Young-Laplace Equation. The differential equation for the flow and its solution are given in Equation 4-1 and 4-2 respectively (Washburn 1921).

$$\frac{dx}{dt} = \frac{\sigma R cos(\theta)}{4\mu x} \qquad\qquad 4\text{-}1$$

$$x(t) = \sqrt{\frac{\sigma R cos(\theta)}{2\mu} t} \qquad\qquad 4\text{-}2$$

The 1D Washburn model can be extended to describe volume absorption into a porous medium by conceptually considering the porous medium as an array of parallel capillary tubes of equal diameter, where V (t) is the total volume absorbed by the porous medium and A_{open} is the total wettable area of the capillary tube array at the interface with the fluid reservoir (Equation 4-3) (Middleman 1995).

$$V(t) = A_{open} \sqrt{\frac{\sigma R cos(\theta)}{2\mu} t} \qquad\qquad 4\text{-}3$$

The relevant physical properties of the fluid for the Washburn model are surface tension and viscosity. The ratio of surface tension to viscosity dimensionally represents a characteristic wicking velocity intrinsic to the fluid. For the study goal of developing a tool to compare the transport of different polymer resins through the CNTs, the characteristic wicking velocity provides a good qualitative assessment of the compatibility of the polymer resin to be utilized in the thermal curing approach for microneedle fabrication. The characteristic wicking velocity for several candidate polymer resins is given in Table 4.2.

Polymer	σ (mN)/m	ν (cSt)	$\dfrac{\sigma}{\mu}$ (cm/s)
(Water)	73	1	7,300
SU-8 2002	47	8	558
SU-8 2010	47	380	10.4
(Glycerol)	64	1,110	4.57
BOPDA Polyimide	19	1,400	1.28
SU-8 2025	47	4,500	0.857
HD-4110 Polyimide	19	7,500	0.239
SU-8 2100	47	45,000	0.084

Table 4.2- Characteristic wicking speeds of candidate polymers used in this study.

4.2.2 Materials & Methods

As the properties of vertically-aligned CNT arrays, such as packing density, entanglement, and nanotube diameter, vary immensely between CNT samples due to the exact procedure used to fabricate the nanotubes, the validity of the Washburn model must be demonstrated using the specific type of CNT array used in this study. Unpatterned vertically-aligned CNTs, fabricated by the methods presented in Chapter 2, are used to validate the Washburn model by characterizing the absorption of glycerol. The surface tension and viscosity of glycerol are similar to BOPDA polyimide polymer resin such that the wicking speed of both fluids are similar. A syringe pump is used to dispense a droplet of glycerol of approximate volume of 30 µL onto the CNT surface (Elite Syringe Pump, Harvard Apparatus, Holliston, MA). Images of the droplet absorption into the CNT array are captured by a microscope camera filming

at a frame rate of 30 frames per second (DCM Series Microscope Camera, ScopeTek, Hangzhou, China).

The image stack from the droplet absorption is imported and processed in MATLAB. A custom script converts the grayscale images of the droplet into binary images to allow for the diameter and height of the droplet in each frame to be measured. The droplet is approximated as a spherical cap to allow for calculation of the droplet volume in each frame (Equation 4-4).

$$V = \frac{\pi h}{6}(3r^2 + h^2)$$ 4-4

After contacting the surface of the CNTs, the diameter of the glycerol droplet remains constant such that the extension of the Washburn equation to fluid volume (Equation 4-3) can be applied to the data to determine if transport of polymer resin into the CNT array follows the Washburn model.

4.2.3 Results

The absorption of glycerol droplets into unpatterned CNTs demonstrated good agreement with the Washburn model, as determined by curve fit to the data (Figure 4.2). Thirty microliter droplets of glycerol were fully absorbed by CNT samples on the order of seconds, allowing for sufficient time resolution of the adsorption process. The volume of the spherical cap was measured until the droplet regressed to a volume of approximately 30% of its original volume. Beyond this point, the resolution of the camera and the spherical cap assumption prohibited accurate measurement of the volume. The Washburn model also accurately predicts the time when the droplet is fully absorbed. The experiment was repeated 40 times on different CNT samples, and all cases showed good agreement with the Washburn model.
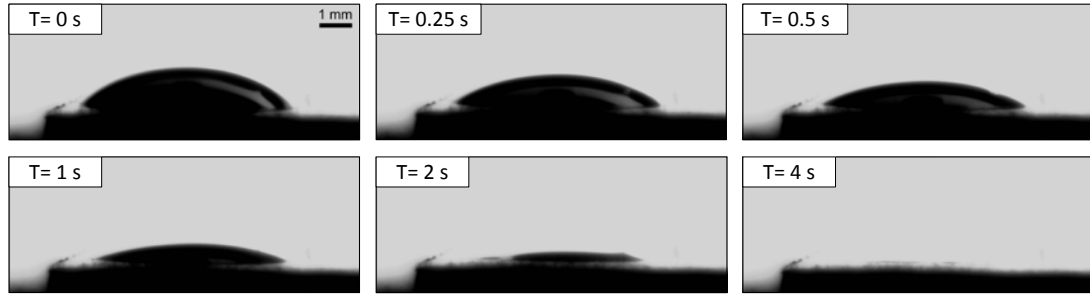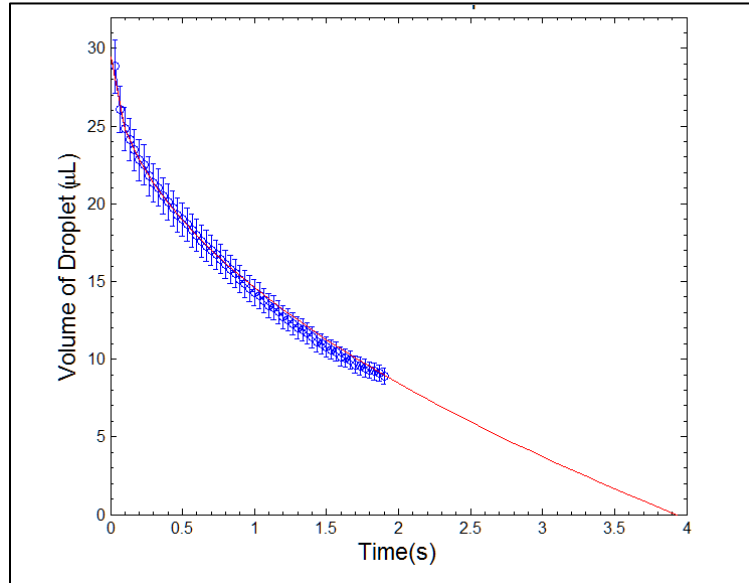
Figure 4.2 (a) Time-lapse images of glycerol droplet being absorbed into unpatterned CNT surface. **(b)** Representative glycerol droplet absorption data. Blue points represents experimental data. Red line represents fit of data to Washburn model.

The data demonstrates that the transport of viscous fluids through the CNTs used in this study can be modeled by the Washburn equation. This result was expected from previous fluid transport studies through CNTs (Zhou 2005). However, validation is a necessary step considering the wide range of catalyst preparations and CVD protocols that can be used to produce vertically-aligned CNTs (Park and Lee 2012). Furthermore, the use of glycerol, which has a similar wicking

velocity as BOPDA polyimide, specifically demonstrates the validity of the Washburn model for highly viscous resins under consideration for the CNT-polymer composite microneedle.

4.3 Application to Thermoset Fabrication Process

4.3.1 Wicking Into the Lumen

With the Washburn model demonstrated as a suitable model for describing capillary flow of viscous fluid in CNT networks, focus is now turned on adapting the Washburn model for the patterned microneedle geometry under the conditions of spin coating. The first consideration is to understand the transport of polymer through the microneedle lumen. The Washburn model is applied for the transport of various polymer resins through a standard lumen diameter of 40 µm. As a simplification, the dynamic contact angle in the Washburn model is set to 0° such that the only relevant material property under consideration in the Washburn model is the capillary radius, *R*, which is equivalent here to the lumen radius. Previous results have demonstrated that wet and dry chemical functionalization techniques can be used to tune the contact angle of CNTs (Aria and Gharib 2011). Wetting properties of CNTs are also highly dependent on the parameters of CNT fabrication. Thus, including contact angles relevant only to the specific CNT species under investigation would only inhibit the application of the model to arbitrary CNT arrays.

Assuming a maximum needle length of 400 µm, results from the Washburn model demonstrate that the central cavity is filled in less than 2 seconds after dropcasting for most polymer resins (Figure 4.3). For polymer resins of significantly lower wicking speed, specifically HD-4110 and SU-8 2100, lumen saturation takes considerably longer but still occurs within the duration of twenty seconds. From the data, it is clear that the lumen is filled at the onset of spin coating. Therefore, the clearing of the lumen depends on the ability of the nanoporous CNT matrix to absorb all of the resin that is present in the lumen. As a further complication, excess

resin from the top of the microneedle at the beginning of spin coating continues to replenish the

lumen, making the lumen a nearly infinite reservoir. (Figure 4.4a).
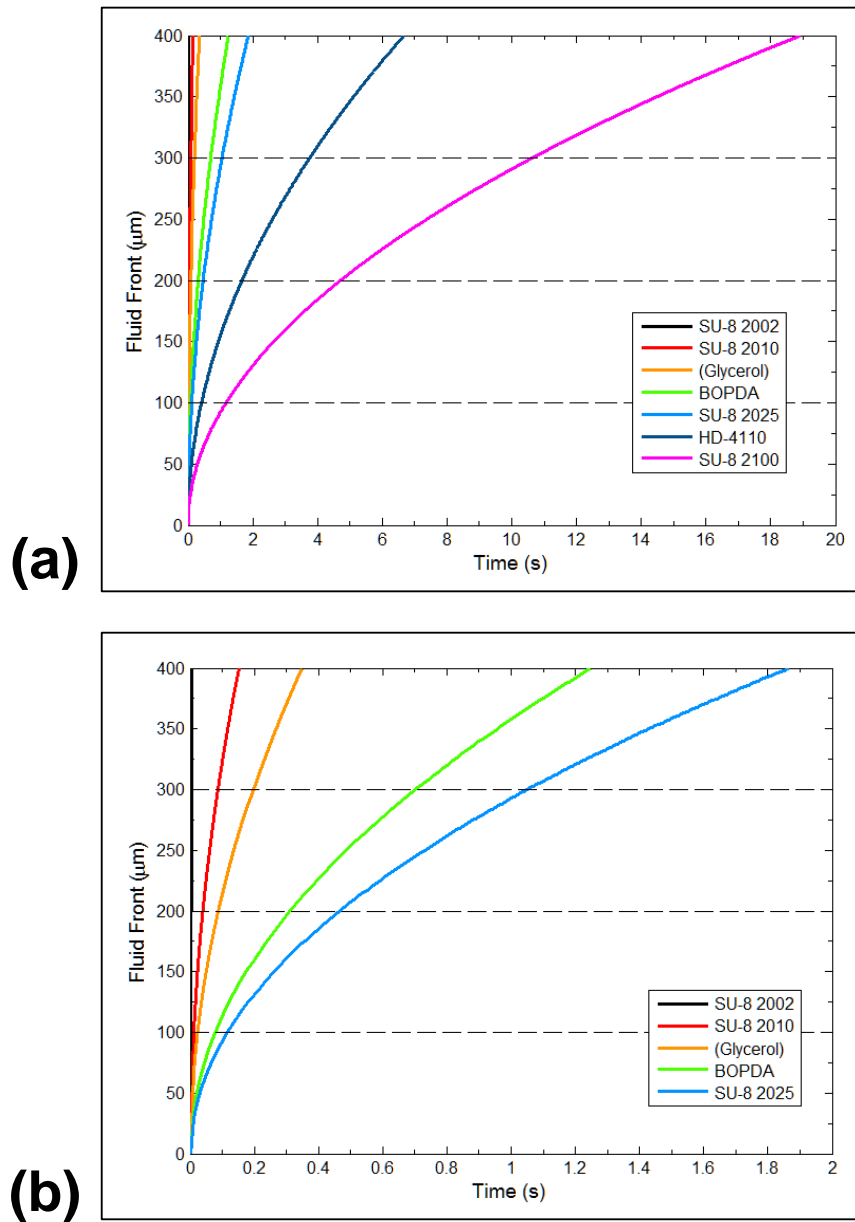
Figure 4.3- Progression of polymer resin into 40 µm diameter lumen.

4.3.2 Effect of Spin

At the beginning of spin coating, the CNT scaffold is completely surrounded by polymer resin (Figure 4.4a). The effective capillary diameter of the CNT scaffold for the Washburn model is set to 30 nm, coinciding with the mean distance between nanotubes in the CNT scaffold. In comparing the curvature of the 40 µm diameter lumen to a single CNT capillary tube of 30 nm diameter, the capillary tube is small enough such that the interface between the lumen and the capillary tube can be considered planar, as is assumed in the standard Washburn model presented thus far. This argument can also be extended to the outer lateral surface of the microneedle such that curvature of the microneedle does not need to be considered in the transport model through the CNT matrix.

Spin coating is performed at constant angular velocity in the range of 1,000 – 3,000 rpm depending on the polymer resin (see Section 3.2). Thus, a rotating reference frame can be used to evaluate the forces on the microneedle and polymer resin. A Coriolis force is exerted on the polymer resin. However, the Coriolis force acts only to push the fluid in the azimuthal direction, causing no net effect to flow for an axisymmetric microneedle scaffold. In contrast, the centrifugal force points in the outward radial direction with magnitude $\rho\omega^2 r$ which, in principle, can act to aid capillary force in clearing polymer resin from the lumen.

Centrifugal force can be appended to the Washburn equation as a body force (Middleman 1995). For transport from the lumen into the CNT matrix, centrifugal force acts in the direction of capillary transport (positive sign, Equation 4-5). For transport from the outer lateral surface of the microneedle, centrifugal force acts against the direction of capillary transport (negative sign, Equation 4-5).
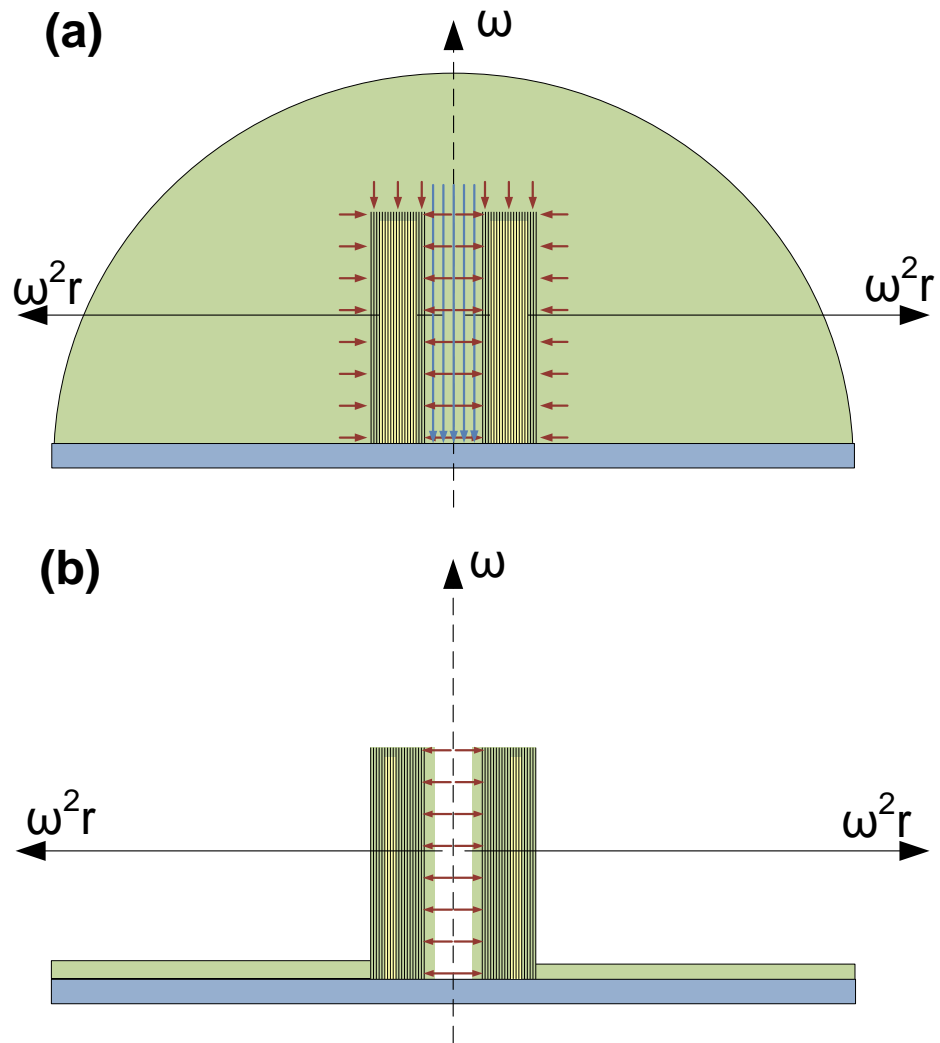
Figure 4.4- Illustration of polymer resin wicking into cross-section of nanoporous CNT structure at early stage of **(a)** and late stage of spin coating **(b).** Blue lines indicate transport into the lumen. Red lines indicate transport into the CNT structure.

The diameter of the pore or capillary is denoted as R, the distance from the center of the microneedle is denoted as r, and the angular velocity of the sample during spin coating is denoted as ω.

$$\frac{dx}{dt} = \frac{\sigma R}{4\mu x} \pm \frac{\rho(\omega^2 r)R^2}{8\mu}$$

4-5

In comparing the magnitude of the capillary and centrifugal terms, as a function of pore size, the capillary term dominates the centrifugal term by more than 7 orders of magnitude. Figure 4.5 illustrates this for the case of BOPDA polyimide spin coated at 1,000 RPM, or 105 rad/s, being wicked from the lumen into hypothetical CNT networks of varying capillary sizes, *R*.
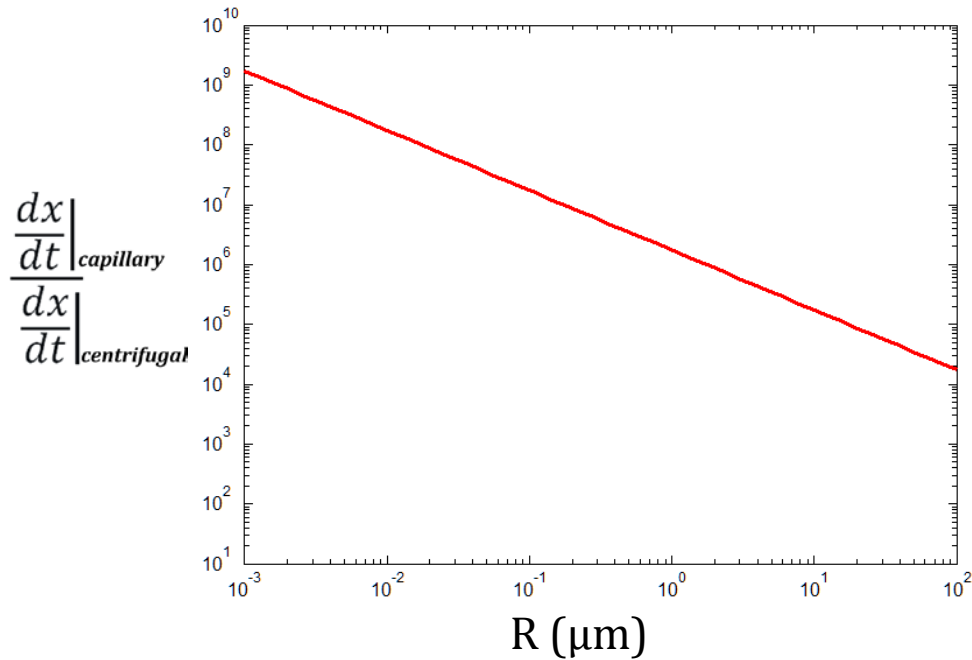
Figure 4.5- Ratio of Capillary and Centrifugal Terms in Washburn Equation as a function of capillary size (Equation 4-5).

In the range of pore size for the CNT network used in this study, 15 nm pore radius, the capillary term is 9 orders of magnitude higher than the centrifugal term. In generalizing this result for different resins and larger spin speeds considered in the fabrication of microneedles, the result of the centrifugal action being negligible compared to the Washburn capillary action is consistent. Therefore, the action of wicking into the CNT network during spin coating can be represented by the original Washburn equation (Equation 4-2).

This is a very important consideration, as it shows that the capillary action of polymer resin through the CNTs is independent of spin speed. In terms of the fabrication process, this result decouples the action of determining a polymer base thickness from the action of forming the CNT-polymer composite through capillary action. From a polymer resin's spin speed curve, the spin speed alone can be used to determine the base thickness. Transport through the CNTs can be characterized by the wicking velocity alone, the ratio of surface tension to viscosity of the resin, to ensure proper setting of the CNT-polymer composite, including a clear lumen. This criterion is still subject to the ultimate range of achievable spin coated film thickness, which is determined by the physical properties of the fluid. However in practice, this criteria allows for fine tuning of the base thickness over the spin speed curve without affecting the formation of the CNT-polymer composite.

4.3.3 Limitations on Lumen Diameter

As described in the previous section, the lumen of the microneedle becomes filled in a matter of seconds after dropcasting. In this same time span, the fluid front of the polymer resin only advances 1-10 µm into the nanoporous network, depending on the resin's wicking velocity. As an additional consideration, in the early stages of spin coating, when excess resin still covers the microneedle, the lumen is continuously being refilled, representing an almost infinite reservoir (Figure 4.4a). Only in later stages of spin coating, when the excess polymer resin is removed from the top surface of the scaffold, can the lumen begin to be emptied by transport through the nanoporous network (Figure 4.4b). Therefore, the total amount of resin absorbed by the CNTs through the lumen is potentially much more than the physical volume of the lumen.

The necessity to drain the volume of the lumen through the surface area of the lumen for the thermal fabrication method places restrictions on the size of the lumen, since the ratio of lumen volume to surface area is linear in diameter. This restriction was observed in a study of

three different microneedle designs. Each design had the same outer diameter, 150 µm, with a varying lumen diameter of either 25 µm, 40 µm, or 75 µm. Each microneedle design was incorporated with BODPA polyimide using the same thermal fabrication protocol as described in Section 3.2.2.2. After fabrication, the lumen was observed for blockage at both the top and the bottom of the needle through SEM imaging (Figure 4.6). The lumen was clear for the microneedles with lumen diameters of 25 µm and 40 µm. Additionally, the open lumen for these designs was verified by fluid delivery experiments, as will be discussed in Chapter 5. For the microneedle with a 75 µm lumen, inspection of the bottom of the needle reveals a clogged lumen.

Outer/Lumen Diameter (µm)	150/25	150/40	150/75
CNT Scaffold			
CNT- BOPDA Polyimide Microneedle	95/20	95/30	95/50
Underside of CNT- BOPDA Polyimide Microneedle			
Ratio of Scaffold Volume to Lumen Volume	32	12	2.7
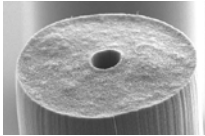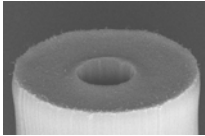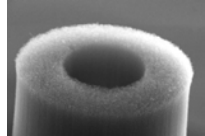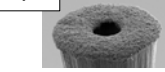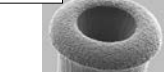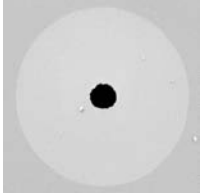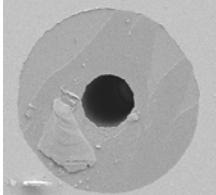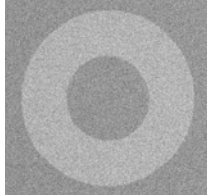
Figure 4.6- Matrix of different lumen diameters showing lumen obstruction for larger lumen diameters. While capillography shrinks the body of the microneedle above the polymer base, the bottom of the microneedle imbedded in the polymer base retains its original dimensions.

The fitness of a microneedle geometry for being able to absorb the resin flowing into the lumen can be determined by the ratio of the open volume in the microneedle to the lumen

volume. Assuming an approximate open area fraction of 90% for the CNT scaffold, the ratio of open scaffold volume to lumen volume is 32, 12, and 2.7 for the 25 µm, 40 µm, and 75 µm diameter lumens respectively. In the early stages of spin coating, it is expected that polymer resin wicks into the scaffold structure from the entire scaffold surface area (Figure 4.4a). Therefore, it is assumed that the scaffold to lumen volume ratio must be sufficiently higher than 1 to accommodate wicking from all surfaces, while still allowing the lumen to be completely cleared in the later stages of wicking, when the lumen becomes the only active wicking surface.

The dependence of the thermal fabrication process on passive fluid transport ultimately limits the maximum size of the lumen for a given outer needle diameter. For fluid delivery through the microneedle, lumen diameter represents a potentially critical parameter, as the volumetric flow rate through the needle scales with lumen diameter to the fourth power for Poiseuille flow. Chapter 5 will investigate further, in the context of delivery, the constraint lumen size has on deliverable volume into the skin for transdermal drug delivery. In order to circumvent this restriction on lumen diameter, the selective UV curing method presented in Chapter 3 would have to be utilized, as it provides for an active method for clearing the lumen.

4.3.4 Capillary Action Through the CNT Scaffold

Wicking from the outer surface of the microneedle is quickly extinguished as the polymer resin droplet is spread across the substrate in the first few seconds of spin coating. Thus, for the majority of the duration of spin coating, wicking from the central cavity is the dominant transport direction (Figure 4.4b). Transport of polymer resin from the lumen through the CNT scaffold as characterized by the Washburn model is presented in Figure 4.7 for various candidate polymer resins. The duration of the dropcasting and spin coating step is sixty seconds for all resins. After that, the sample is transferred onto a hot plate to begin curing the polymer resin. The progression of the fluid front during this time, as predicted by the Washburn model, is used as an indication of

the ability of the resin to fully envelop the CNT scaffold during spin coating, leading to the clearing of the microneedle lumen. The Washburn model describes flow in an infinitely long capillary. In practice, the thickness of the needle ranges from 55 – 63 µm depending on the specific design. Therefore, for fluid front positions greater than the microneedle thickness, it is assumed that the resin fully envelops the CNT scaffold.
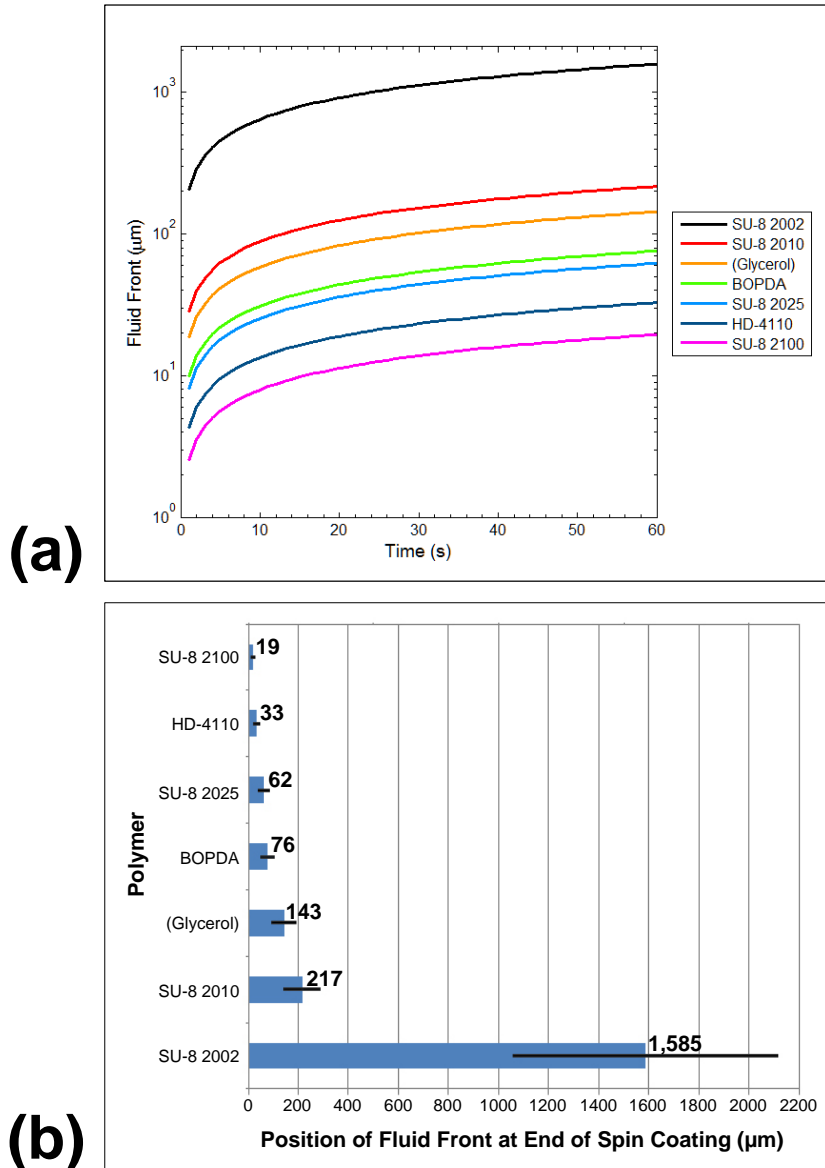
Figure 4.7- (a) Fluid Front vs. Time for CNT scaffold with effective capillary diameter of 30 nm. **(b)** Position of Fluid Front at end of Spin Coating for each polymer. Error bars represent effect of uncertainty in the effective capillary diameter of the CNT scaffold.

Polymers with a very high wicking speed, such as SU-8 2002 and 2010, with wicking speeds of 558 cm/s and 10.4 cm/s respectively, can completely penetrate the thickness of the microneedle with predicted fluid fronts at the end of the spin coating cycle greater than the thickness of the microneedle. While these polymers are adept for forming the CNT–polymer composite, their overall low viscosity does not allow for the formation of a thick base via spin coating, as required by the general microneedle requirements. Glycerol has a suitable wicking speed for penetrating the CNT scaffold. However, glycerol is not a thermoset resin and cannot be used directly to form a composite structure. In the other extreme, polymer resins with very low wicking speed, such as SU-8 2100 and HD-4110, do not allow for sufficient transport into the CNT scaffold to allow for the lumen to be cleared passively. Specifically for SU-8 2100, with a predicted fluid front of only 19 µm after spin coating, the lumen is completely clogged, as can been seen from both the top and the bottom of the microneedle. Thus, these resins are only capable of being incorporated into the CNT-polymer microneedle by using the UV fabrication process.

BOPDA polyimide and SU-8 2025 both have predicted fluid fronts in the range of the thickness of the microneedles. Therefore, both polymers are qualitatively predicted to fully envelop the CNT scaffold, providing for the proper conditions for clearing the lumen of resin. Furthermore, the spin speed curves of both resins demonstrate the capability to generate a base of sufficient thickness to support the microneedle array structure. Experimentally, BOPDA polyimide has consistently demonstrated the ability to clear the lumen. Overall, SU-8 2025 showed mixed results when being processed through a thermal fabrication cycle. A few microneedle array samples showed clear lumen, while the majority of samples demonstrated a clogged lumen as observed by inspection of the lumen on the underside of the microneedle.

The Washburn model, in general, represents an optimistic look at the ability of polymer resin to wick through the CNT scaffold. By modelling the CNTs as a parallel bundle of equal

sized capillary tubes, secondary effects, such as tortuosity, that can impede the transport rate are neglected. Previous work has also demonstrated that for porous media with a distribution of capillary sizes, like CNTs, that the Washburn model overestimates the transport rate as the media approaches saturation (Zhou 2005). This is because in a porous media, larger capillaries are filled at a faster rate than smaller capillaries such that near saturation, the global transport rate is determined solely by transport through smaller, more resistive capillaries. Results presented here approximate the effective capillary diameter as the mean interspacing between nanotubes for the CNT scaffold. In considering VA-CNTs from different sources and fabrication methods, the mean interspacing between nanotubes from generic VA-CNT samples can vary greatly. In considering an uncertainty of 20 nm for the 30 nm capillary diameter, the total transport length of the fluid front during spin coating has a maximum uncertainty of 33%, as visualized in Figure 4.7b.

In applying the thickness of the microneedle as a prerequisite transport distance for forming the composite needle with a clear lumen, the Washburn model can finely differentiate between the performance of resins with similar wicking speeds such as SU8-2025 and BOPDA polyimide, with wicking speeds of 1.28 and 0.857 cm/s respectively. From these results, a screening criterion can be established, for the microneedle geometry under investigation, that a polymer resin must have a wicking speed greater than 1 cm/s in order to be a suitable candidate for incorporation through the thermal fabrication process (Table 4.3).

Polymer	σ (mN)/m	ν (cSt)	$\dfrac{\sigma}{\mu}$ (cm/s)	Lumen Cleared by Thermal Curing?
(Water)	73	1	7,300	N/A
SU-8 2002	47	8	558	YES
SU-8 2010	47	380	10.4	YES
(Glycerol)	64	1,110	4.57	N/A
BOPDA Polyimide	19	1,400	1.28	YES
SU-8 2025	47	4,500	0.857	NO
HD-4110 Polyimide	19	7,500	0.239	NO
SU-8 2100	47	45,000	0.084	NO

Table 4.3- Wicking speeds of candidate polymers used in this study. A wicking speed greater than 1cm/s is required for a polymer to be used in the thermal curing technique. This criteria is verified by experimental observation summarized in the last column.

4.4 Conclusions

The thermal curing method for fabricating CNTs relies on passive capillary action to clear the lumen and infiltrate the CNT scaffold to form the CNT-polymer composite. Understanding the underlying fluid mechanics behind this capillary transport is critical in order to apply this simple, passive fabrication method to a wide range of polymers to improve the utility of the CNT-polymer composite microneedle concept. Fluid absorption experiments performed on unpatterned CNTs demonstrated that the capillary action of viscous polymer resins or fluids can be described by the Washburn model of capillary action.

In applying the Washburn model to the geometry of the microneedles under the conditions of spin coating, it was shown that the contribution of Washburn capillary action dominates the transport of polymer resin into the CNT scaffold, neglecting any centrifugal

contributions from spinning. The ability to clear the lumen using capillary action was shown to ultimately place an upper limit on the size of the lumen relative to the thickness of the microneedle. For the 150 µm outer diameter microneedle under investigation in this study, it was shown that the lumen cannot be passively cleared through capillary action for lumen diameters greater than 75 µm. To overcome this limitation, the thermal curing method must be substituted for the UV curing method, which allows for the lumen to be actively cured through a wet development process.

The rate of capillary transport in the Washburn model scales with a characteristic wicking velocity, which is an intrinsic property of the polymer resin. The characteristic wicking velocity is equal to the ratio of surface tension to viscosity for a fluid, which has the equivalent unit of velocity. While the wicking velocity itself is not an accurate assessment for the actual fluid speed, the wicking velocity can act as a quantitative indicator of whether or not a particular polymer resin can be utilized for the thermal curing fabrication technique. For the specific geometry investigated in this study, 150 µm outer and 40 µm luminal diameter, it was determined that a wicking velocity greater than 1 cm/s is necessary to achieve a clear lumen after spin coating.

With the inclusion of the results from the polymer resin transport analysis, Table 4.1 presents a complete list of microneedle requirements and the corresponding selection criteria for choosing a polymer. With the addition of the wicking velocity criteria for the thermal curing method, all of the polymer selection criteria consist of simple material property data such as surface tension, stiffness, and spin speed curves. Thus, these criteria can be applied to any general thermoset polymer for thermal curing or negative photoresist for selective UV curing to determine whether the polymer is an appropriate match for forming the CNT-polymer composite microneedle. This set of requirements eliminates the underlying empirical nature of forming the composite, as presented in Chapter 3, and can allow for wider adaptation of the technology.

Chapter 5

Laboratory and *In Vitro* Delivery

5.1 Introduction

From the fabrication methods presented in Chapter 2, two microneedle architectures were deemed suitable to proceed to the stage of incorporation onto a delivery platform by assessing the ability of each microneedle architecture to reliably satisfy the fabrication requirements. The two microneedle architectures chosen were CNT-SU8-2025 and CNT-BOPDA polyimide. Each microneedle has an outer diameter of 150 µm and a height between 200-250 µm. The CNT-SU8 microneedles have a lumen diameter of 25 µm, and the CNT-BOPDA microneedles have a lumen diameter of 30 µm.

Here, it is demonstrated that the CNT-polymer microneedles have the capability to successfully deliver aqueous dye using two delivery mediums: hydrogel and *in vitro* swine skin. Additionally, before testing in a delivery medium, the performance of the microneedles is assessed by passing fluid through the microneedles without a delivery medium (delivery into the air) to verify that the polymer base and microneedles are leak-proof. Focus in these experiments is given on the physical aspects of delivery, including the ability of the microneedles to penetrate skin and the ability of the microneedles to conduct fluid into the skin.

The goals of these experiments are to:

- Demonstrate that the CNT-polymer composite microneedles can function as a microneedle, as indicated by successful *in vitro* skin penetration and fluid delivery.

- Demonstrate the compatibility of CNT-polymer composite with different drug delivery platforms.

- Assess the performance the combined system of the CNT-polymer microneedles with a given drug delivery platform.

Of particular importance is to understand how the delivery results are influenced separately by the microneedles and the drug delivery platforms supporting the microneedles. Several drug delivery platforms are investigated, including syringes and band-aid style skin patches. Fluid is driven through these platforms by either hand actuation or actuation by a syringe pump.

A hand actuated band-aid style skin patch is envisioned as the optimal delivery method. Hand actuation simplifies the design of the skin patch by reducing costs and eliminating power requirements associated with an electric pump, and works towards the universal goal of microneedle technology to broadly disseminate medicine without the assistance of medical infrastructure and personnel. Here, development of the hand actuated skin patch is considered in parallel to the development of the CNT-polymer microneedles in order to build a complete drug delivery system.

5.2 Materials & Methods

5.2.1 Delivery Platforms

Several delivery platforms are utilized to characterize delivery through the microneedles, as well as to demonstrate the adaptability of the CNT-polymer microneedles to be incorporated

into several delivery architectures. In this section, a detailed description of the fabrication and the utility of each delivery platform is presented.

5.2.1.1 Dye Coated Microneedles

The first delivery platform considered is a microneedle coated with dye. The purpose of this arrangement is to assess the ability of the microneedles to penetrate skin separately from the ability to deliver fluid. In this way, the mechanical strength of the pillar can be assessed separately from the fluid transport properties of the microneedle.

For this experiment, microneedles were kept on their native silicon substrate. The microneedles and silicon substrate were attached to a 1" x 3" glass slide with double-sided copper tape. A dye solution of methylene blue and chloroform was prepared and poured over the microneedle array (Sigma-Aldrich, St. Louis, MO). Upon evaporation of the chloroform, dry methylene blue powder conformally coated the microneedles. During *in vitro* skin penetration, the methylene blue powder is reconstituted into a dye upon contact with the interstitial fluid from the skin. Concentrated pockets of dye in the skin are then identified as penetration marks.

5.2.1.2 Modified Syringe

An adapter was placed on a standard 3 mL hypodermic syringe to support delivery through a microneedle array. Figure 5.1 demonstrates an example of a CNT-SU8 microneedle array placed upon an adapter assembly used to connect the microneedles to the syringe (not pictured). This approach has been used in previous microneedle studies such that the simplicity of the delivery platform allows for focus on the delivery capabilities of the microneedle as well as use of a syringe pump to precisely actuate the flow (Stoeber and Liepmann 2005) (Norman et al. 2013).
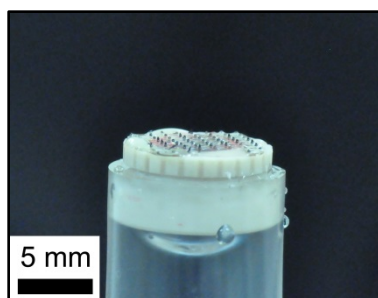
Figure 5.1- Modified syringe platform for microneedle drug delivery.

The microneedle array is glued to a hard plastic reservoir adapter using a quick cure epoxy (Idex Health & Science, Odex Harbor, Washington). The reservoir adapter has an open cavity diameter of approximately 3 mm on its top surface, allowing for actuation of a maximum of 9 microneedles. The rest of the microneedles are adhered directly to the top surface of the reservoir and cannot be filled with fluid. The reservoir adapter is fitted to a piece of clear plastic tubing. The tubing is fitted to a hypodermic syringe with a barb-luer lock adapter. Actuation is achieved by either a syringe pump or manual forcing of the syringe.

5.2.1.3 Single Reservoir Skin Patch

PDMS (polydimethylsiloxane) skin patches were constructed as an additional delivery platform for investigating drug delivery through CNT-polymer microneedles. PDMS is chosen as the material as its soft, flexible properties resemble that of a band-aid. In this sense, a PDMS skin patch represents a platform that can potentially allow for patient administration without direct medical supervision from a nurse or doctor. The first PDMS skin patch constructed is based on a single drug reservoir, hand actuated design. Designs of this type have been utilized in previous conceptions and studies (Gharib, Sansom, and Aria 2010) (Häfeli et al. 2009).

A single reservoir skin patch was designed specifically for use with the CNT-polymer microneedles. The skin patch is 3.4 cm in diameter, with a thickness of 0.5 cm (Figure 5.2 a,b).

The microneedles are connected to the PDMS patch using the same reservoir adapter as in the modified syringe design such that the microneedles can be interchanged on the reservoir during experiments. The microneedles sit directly below the drug reservoir (Figure 5.2 c).
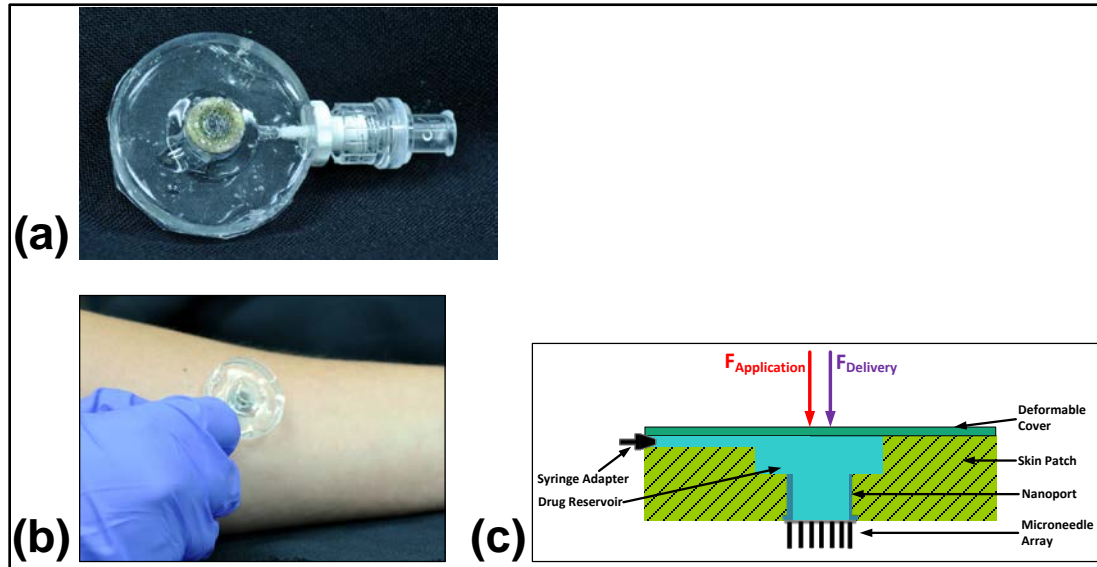
Figure 5.2- Single Reservoir Skin Patch. **(a)** Image of the single reservoir skin patch with CNT-SU8 microneedles. **(b)** The single reservoir skin patch with CNT- SU8 microneedles placed on the forearm to illustrate scale in handling and placing the patch. **(c)** Cross-section schematic of the components and operation of the single reservoir skin patch.

A thin PDMS membrane, of 2 mm thickness, covers the drug reservoir such that by squeezing the cover actuates flow through the microneedles. The drug reservoir has a top diameter of 1.5 cm to allow for actuation with a single finger. The dimensions of the skin patch are selected in order to emulate a band-aid in terms of handling and wearability. The large size of the skin patch compared to the minute dimensions of the microneedles is designed to ensure the skin patch is universally accessible to patients for the goal of self-administration, particularly for patients with impaired coordination.

The drug reservoir is filled through a channel that runs underneath the PDMS cover to the side of the patch. A barb-luer lock adapter at the end of the channel allows for the patch to be

filled by a hypodermic syringe. Additionally, a check valve is placed in between the barb-luer lock adapter and the syringe to prevent backflow (Qosina, Edgewood, New York). Alternatively, the check valve can also be replaced with a luer lock cap during delivery.

To fabricate the skin patch and deformable cover, molds were machined out of acetal plastic using a CNC mill (CNC Mini-Mill 3, Minitech Machinery Corporation, Norcross, Georgia). PDMS resin (Sylgard 184, Dow Corning, Midland, MI) was poured into the molds and then set thermally at 80°C in a convection oven for 1 hour. After removing the components from their respective molds, the cover was attached to the skin patch by using PDMS resin as an adhesive and thermal curing at 80°C in a convection oven for 30 minutes. Similarly, the barb-luer lock adapter was set in the skin patch using PDMS resin as an adhesive element.

5.2.1.4 Dual Reservoir Skin Patch

A second PDMS skin patch was designed utilizing two drug reservoirs connected in series (Figure 5.3). The primary drug reservoir is offset from the microneedles and holds the majority of the drug. (Figure 5.3 d) The primary drug reservoir is covered by a thin, highly deformable silicone (EcoFlex 30 Smooth-On, Easton, PA) to allow the drug release into the skin to be actuated by pressing on the top of the reservoir akin to the single reservoir patch. A small secondary reservoir sits directly above the microneedles to ensure a continuous flow of drugs into the microneedles. The two reservoirs are connected to each other through a small channel within the patch.

The purpose of using an offset drug reservoir is to separate the action of applying the microneedles to the skin and actuating drug delivery. By using a two-step approach, the chance of accidental drug discharge while applying and removing the microneedles is significantly reduced. This is especially important for making the microneedles universally accessible to patients for
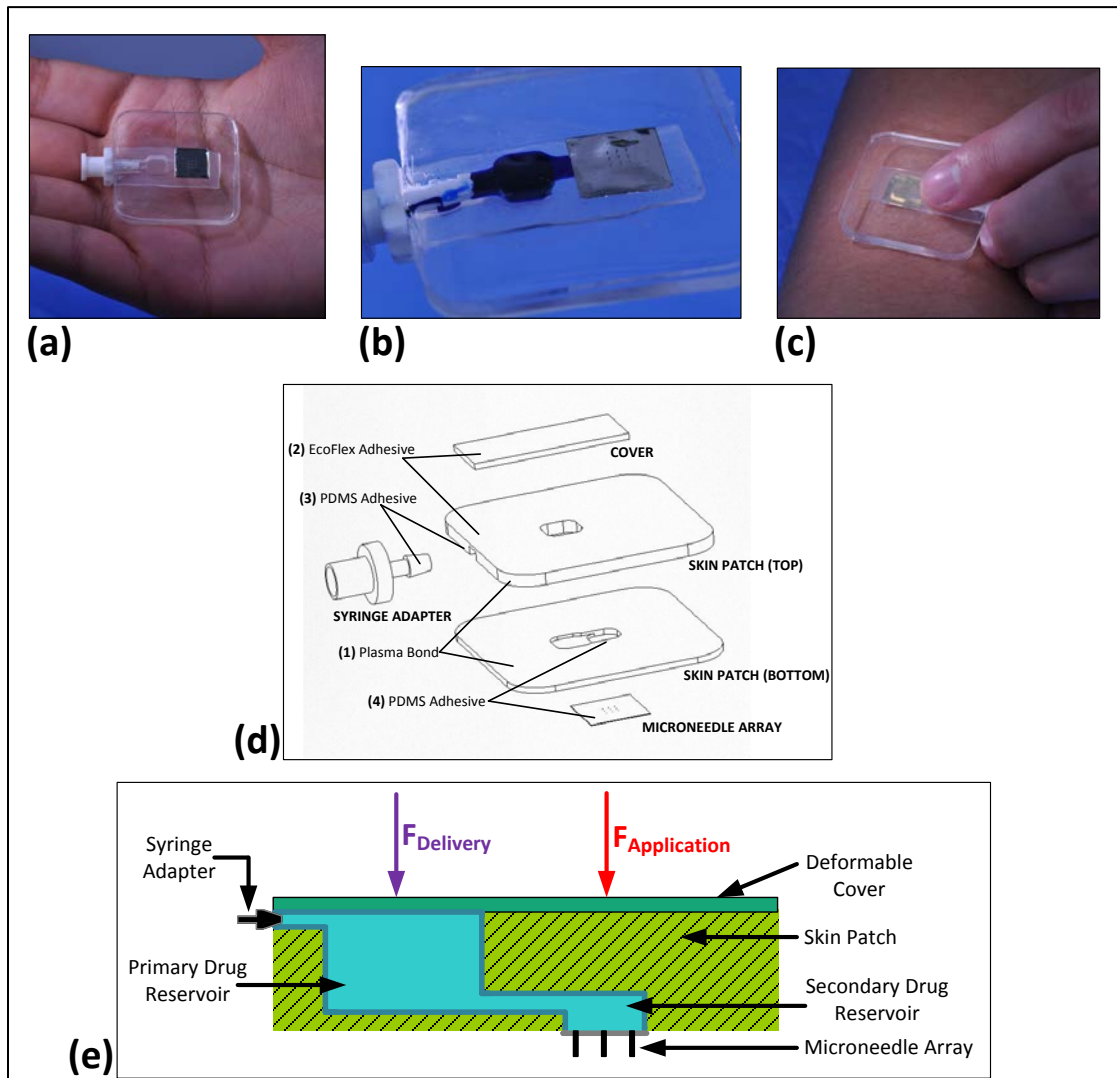
Figure 5.3- Dual Reservoir Skin Patch with CNT-BOPDA Microneedles. **(a)** Skin patch fits within a person's palm. The CNT-BOPDA microneedles are adhered directly to the skin patch. **(b)** Skin patch filled with aqueous methylene blue solution to illustrate the flow path. **(c)** Application of microneedles onto the forearm with actuation of the primary drug reservoir. **(d)** Fabrication schematic of skin patch. **(e)** Cross section schematic of components and operation of skin patch.

self-administration. Particularly for patients with impaired coordination, the two-step approach allows for adjustment in placing the patch before committing to drug delivery. The size of the skin patch is designed specifically such that the delivery can be achieved by using two fingers.

The first finger presses down directly on top of the microneedle to achieve skin penetration. The second finger then presses on the primary drug reservoir to actuate the flow of drug. The overall skin patch is 3.6 cm x 3.6 cm, with a thickness of only 3 mm. In contrast to the single reservoir skin patch, the microneedles in the dual reservoir skin patch are attached directly to the skin patch using uncured PDMS as an adhesive. In this way, the flexibility of the polymer base of the microneedles directly complements the flexibility of the PDMS, allowing for local deformation during skin penetration to improve skin contact.

The components and fabrication steps of the skin patch are illustrated in Figure 5.3d. The patch is constructed from two PDMS layers that are bonded together to create the reservoirs. A thin layer of highly deformable silicone (EcoFlex 30) is then added as a cover. As before for fabricating the PDMS and EcoFlex layers, the resins were poured into micromachined acetal plastic molds. Each material was thermally cured in a convection oven at 80°C for up to 1 hour.

The two separate PDMS layers were bonded together after a remote oxygen plasma surface treatment of 100 sccm oxygen at 500 W and 200 mTorr for 5 minutes (PVA Tepla M4L Gas Plasma System, Corona, CA). After the surface treatment, the PDMS layers were pressed together under a constant pressure of approximately 10N, and placed in a convection oven at 80°C for 30 minutes to form the bond (1). To attach the cover, a small amount of EcoFlex resin was brushed onto the PDMS surface as an adhesive. After placing the cover on top of the skin patch, the assembly was again placed in a convection oven at 80°C for 30 minutes to set the Ecoflex resin (2). Similarly for attaching the microneedle array and the syringe adapter to the skin patch, PDMS resin was used as an adhesive and allowed to set in an 80°C convection oven for 30 minutes (3,4). A standard syringe is used to fill the skin patch via the syringe adapter, a small luer lock adapter connected to the side of the patch. During experiments, the syringe adapter is capped to prevent backflow.

5.2.1.5 Syringe Pump Skin Patch

A skin patch based on the dimensions of the dual reservoir design was designed specifically for actuation by an external syringe pump (Elite Syringe Pump, Harvard Apparatus, Holliston, MA) through the syringe adapter (Figure 5.4). The similarity in design to the dual reservoir skin patch is to directly isolate the effect of hand actuation versus external pump actuation on the microneedle delivery. The modified patch consists of a single reservoir placed above the microneedles using the same area dimensions as the secondary reservoir on the dual reservoir patch. A thick PDMS cover is used in substitution of the flexible EcoFlex cover to prevent any deformation of the patch during syringe pump actuation. The combined thickness of the patch and cover is 7 mm. The skin patch is connected to a T-junction connected to tubing from the syringe pump, as well as a drain that allows for an accelerated flow rate while filling the tubing without risking damage to the skin patch.

Figure 5.4- Syringe pump skin patch attached to T-junction via luer lock connection.

5.2.1.6 Impact Penetration

Similar to the modification to the Syringe Pump Skin Patch in Section 5.2.1.5 to assess the difference between hand actuation and pump actuation in microneedle delivery, a spring-

loaded applicator is considered here as an alternate to using hand force to press the microneedles into the skin to achieve skin penetration. Previous work examined the effect of penetration speed, or impact, on delivery of hollow microneedles of length between 200 and 300 µm. It was shown that by substituting manually driven penetration for high impact penetration driven by an external applicator, the delivery rate can be significantly raised by over an order of magnitude (Verbaan et al. 2008).

For these experiments, the Syringe Pump Skin Patch was used in order to precisely measure the delivery rate. The Syringe Pump Skin Patch was placed directly above the delivery medium. The tip of the microneedle was placed within 2 mm of the top surface of the delivery medium. An aqueous 1% methylene blue solution was used as the injected fluid in order to visually assess the spread of delivered dye.

To provide the actuation force, a lancing device designed for obtaining blood samples for glucose monitoring in diabetes patients was utilized (FreeStyle Lite Lancing Device, Abbott Laboratories, Abbott Park, Illinois). In standard practice, the lancing device presses a metal needle of a few millimeters in length into a patient's skin to draw blood to be collected on a glucose test strip. The metal needle sits upon a flat plastic plunger. The metal needle was removed from the lancet such that the plunger could be used to contact the skin patch directly above the microneedles (Figure 5.5).

The lancing device was placed directly over the microneedles on the skin patch (Figure 5.5). The plunger of the lancing device was modified to provide a flat area to provide an evenly distributed force over the microneedle array. The surface area of the plunger was approximately 3 mm x 3mm, slightly larger than a 3 x 3 microneedle array. A button on the lancing device releases the compressed spring and presses the plunger into the skin patch at a velocity of 2 m/s, which in turn pushes the microneedles into the delivery medium. The penetration velocity investigated here is consistent with previous studies that examined penetration speeds of 1 m/s

and 3m/s (Verbaan et al. 2008). After penetration, the lancet is left engaged to continue providing steady force to keep the microneedles engaged in the delivery medium. Immediately following penetration, the syringe pump was actuated to begin fluid flow. Delivery was sustained over 5 minutes, at constant flow rate.

Figure 5.5- Impact Penetration Setup. Lancing device sits above the Syringe Pump Skin Patch. Upon actuation, microneedles are driven into hydrogel (4% agarose) as a laboratory model for skin.

5.2.2 Delivery Mediums

5.2.2.1 Into the Air

A combination of three delivery mediums are used in conjunction with the above delivery platforms to assess the performance of the CNT-polymer microneedles. The first delivery medium tested is no delivery medium. Fluid is simply flowed through the microneedles and is expelled into the air. This is used as a baseline assessment to check for several conditions:

- Ensure that the lumen of the microneedles is not obstructed.

- Verify there is no defect in the microneedles, such as a tear in the polymer.

- Verify there is no leak in the skin patch, or defect in the connection between the microneedles and the skin patch.

- Quantify the maximum flow rate through the microneedle-delivery platform system.

Delivering fluid into the air represents an opportunity to evaluate the hydraulic resistance of the microneedles independently of any additional resistance contributed by the delivery medium. In this way, it is assessed whether the lumen size and the number of microneedles are sufficient to allow for an acceptable volumetric flow rate under the pressure limitations imposed by utilizing hand actuation.

5.2.2.2 Hydrogel

Hydrogel is made in different concentrations of agarose ranging from 1% to 4% (UltraPure Agarose, Life Technologies, Grand Island, NY). Hydrogel is used for testing fluid delivery of the microneedle-delivery platform system separate from assessing the strength of the microneedles for achieving skin penetration. In this way, delivery in hydrogel is complementary to the dye coated microneedles in providing a platform to test specific aspects of the delivery. Hydrogel can be easily penetrated with the microneedles. Because of the ease of penetration, microneedles can be used for multiple delivery events into hydrogel. In contrast, as will be discussed in Section 5.4.2.3, microneedles can only be used once for delivery experiments into skin.

4% agarose hydrogel is found to be a good laboratory model for skin in terms of comparable hydraulic resistance. Hydrogel is commonly used here in place of skin samples in delivery experiments due to its high availability and quick preparation time. Delivery of an aqueous solution of methylene blue dye is used to visualize the delivery and assess whether dye is fully delivered into the hydrogel or spills over onto the surface of the gel.

5.2.2.3 *In Vitro* **Swine Skin**

Swine skin is used to represent human skin to assess the microneedle-delivery platform system in actual delivery conditions. Previous studies have shown swine skin is similar to human skin in terms of permeability and thickness (Marro, Guy, and Begoña Delgado-Charro 2001; Schmook, Meingassner, and Billich 2001; Takeuchi et al. 2011). Skin samples were collected from the dorsal region of four month old Yucatan Miniature Swine (Sinclair Bio Resources, Columbia, MO). Skin samples were shaved prior to harvesting and kept frozen at -20°C until use, for a maximum period of 12 weeks. Prior to use, frozen skin samples were placed in a sealed plastic bag and thawed in a room temperature water bath. Extraneous fat from the underside of the sample was removed with a straight edge chef's knife.

Full-thickness skin samples were used with the CNT-BOPDA microneedles. A hole punch was used to create uniform sample sizes of 38 mm diameter. Split-thickness skin samples were used with the CNT-SU8 microneedles. To create split-thickness samples, full-thickness skin samples were placed in a dermatome, which removes the bottom layers of the skin to produce a sample less than 0.5 mm thick consisting of the stratum corneum, epidermis, and upper dermis layers of the skin. During delivery, samples were placed on a glass slide and stretched taut to ensure good contact with the microneedles during delivery.

Similar to delivery experiments performed in hydrogel, an aqueous solution of methylene blue dye is used to visualize the delivery and assess whether dye is fully delivered into the skin or spills over onto the surface of the skin. Microneedles can only be used once for skin penetration experiments, as the microneedles tend to collect various oils and debris from the skin that can occlude the lumen or block the microneedles from properly contacting the skin.

5.2.3 Imaging

The resulting injection sites from both the hydrogel and swine skin experiments were imaged immediately after delivery using a stereomicroscope (Zeiss Stereo Discovery V20, Carl Zeiss Microscopy, Jena, Germany). Microneedles were imaged by scanning electron microscopy before and after skin delivery experiments to assess any structural damage.

5.3 Poiseuille Flow Model for Microneedle and Delivery Platform System

Flow actuated from the delivery platform, through the microneedles, and into a resistive delivery medium can be modelled as Poiseuille flow for steady microfluidic flows. Since the goal of the study is to evaluate the delivery volume and volumetric flow rate, the parabolic velocity profile predicted by Poiseuille flow can be integrated to give a 1D equation for volumetric flow through the system (Equation 5-1).

$$\Delta P = Q \left(\frac{8\mu L}{\pi r^4} \right) \qquad \text{5-1}$$

where Q is the volumetric flow rate, ΔP is the applied pressure, μ is the fluid viscosity, L is the channel length, and r is the channel radius.

A helpful analogy for designing microfluidic flow systems is to consider Equation 5-1 as an Ohm's law for microfluidics (Kirby 2010). Applied pressure is equivalent to voltage and volumetric flow rate is akin to current. Hydraulic resistance, R, can then be extracted from Equation 5-1 as shown in Equation 5-2.

$$\Delta P = QR$$

$$R = \frac{8\mu L}{\pi r^4} \qquad \text{5-2}$$

The exact form of hydraulic resistance given in Equation 5-2 physically represents flow through a cylindrical channel like the lumen of the microneedles. For other flow channel geometry, the hydraulic resistance can be considered as an equivalent resistance to a cylindrical channel.

A flow circuit diagram for the microneedle delivery system is shown in Figure 5.6a for an arbitrary number of microneedles, *N*. Since the microneedle geometry is consistent for each needle, the circuit diagram can be simplified by the circuit relation for parallel resistors (Figure 5.6b). Adding the resulting resistances in series gives a total resistance for the system. All delivery experiments considered here will consist of nine microneedles (*N*=9). From this simplification, it is observed that the resistance of the system can be steadily decreased by the addition of more microneedles. In comparing the size of the microneedle lumen to the millimeter sized channels of the delivery platforms described in Section 5.2.1, the resistance of the delivery platform can be neglected, since resistance scales inversely with channel diameter to the fourth power.
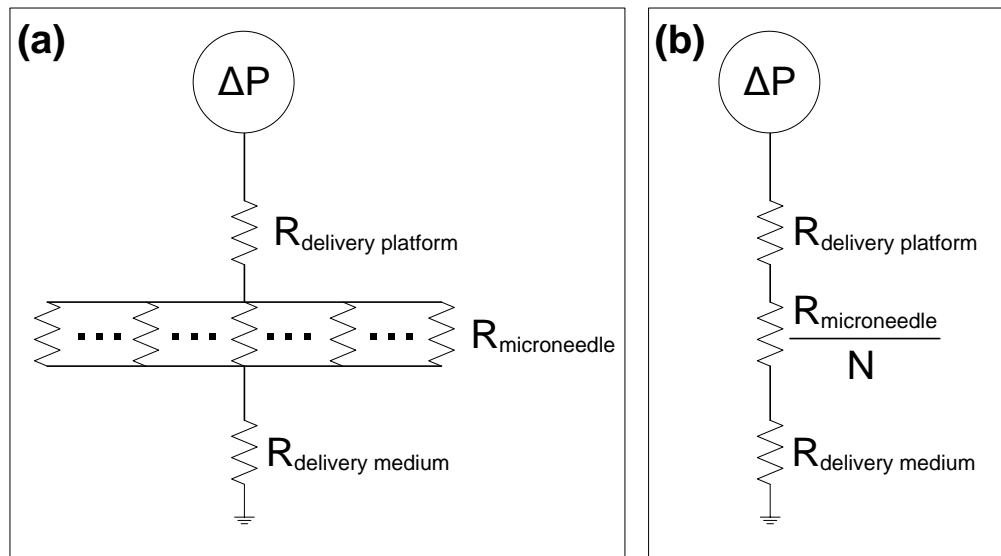
Figure 5.6- (a) Hydraulic circuit representation for microneedle delivery system into a delivery medium for *N* identical microneedles. **(b)** Simplified circuit representation for identical parallel microneedles. Additional microneedles lower system delivery resistance.

For the express application here, this model is used as a tool for considering the separate contributions the skin patch, microneedles, and delivery medium play in resisting fluid flow. Moving forward, the primary sources of hydraulic resistance that will be considered are the microneedles and the delivery medium, while the delivery platform provides the actuation pressure. Minimizing hydraulic resistance is a key design criterion for hand actuated delivery systems. Hand actuation, in practice, limits the total pressure that can be applied to the flow system. With this cap on the maximum applied pressure, minimizing hydraulic resistance is required to ensure proper flow rates can be achieved.

5.4 Delivery Results

The delivery goals for the CNT-SU8 2025 microneedle were different from the goals for the CNT-BOPDA polyimide microneedle. The CNT-SU8 microneedle was the first successful microneedle to be fabricated. The delivery goals for the CNT-SU8 architecture were to separately demonstrate the ability to achieve skin penetration and to conduct fluid through the array via hand actuation.

After these experiments, the focus of the delivery experiments shifted to the newly developed CNT-BOPDA microneedles. The thermal curing approach for the CNT-BOPDA microneedle allowed for microneedles to be fabricated more rapidly, and was seen as being the most advantageous for supporting delivery experiments on the laboratory stage thru *in vivo* testing. Delivery experiments for the CNT-BOPDA microneedle continued where the experiments with CNT-SU8 microneedles ended. The goal of the CNT-BOPDA delivery experiments was to show that the CNT-BOPDA microneedles combined with a hand actuated skin patch can allow for fluid delivery into *in vitro* skin. In this manner, these experiments combined the solid mechanics requirement of penetrating skin with the fluid mechanics requirement of supporting fluid conduction through the microneedle.

5.4.1 CNT-SU-8 2025 Microneedle
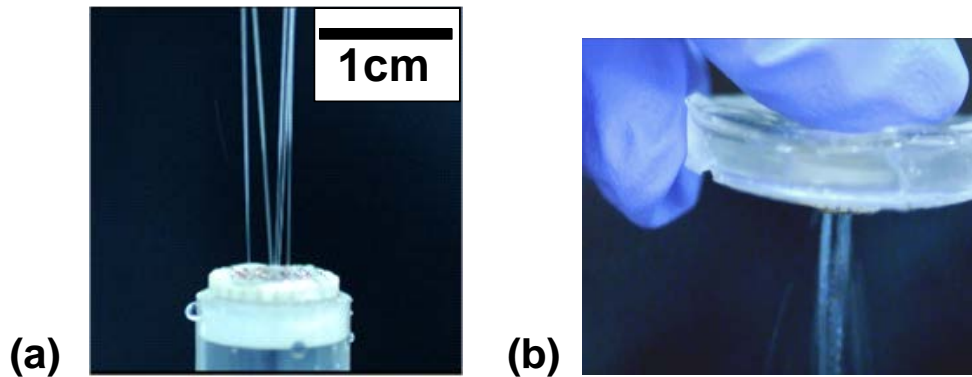
Figure 5.7- Delivery into the air for CNT-SU8 microneedle. **(a)** Modified syringe with total array flow of 4.8 mL/min. **(b)** Flow through single reservoir skin patch under hand actuation.

Liquid flow through the microneedle is demonstrated by connecting the microneedle array to a water filled modified syringe. Despite the small 25 µm lumen diameter per needle, the integrated area of the microneedle array allows for high flow rates into the air of 4.8 mL/min for the array under hand actuation (Figure 5.7a). Despite the relatively thin polymer base of approximately 25 µm, the base shows no signs of fatigue or cracking under high flow rates. Achieving flow greater than 600 µL/min per needle under minimal actuation pressure demonstrates the low hydraulic resistance of the device, which ultimately lowers the work needed to flow liquid through the microneedles at any flow rate. CNT-SU8 microneedles were incorporated into the single reservoir skin patch. Flow was actuated by pressing a single finger into the deformable cover (Figure 5.7 b). To actuate flow, the applied force was exceedingly gentle, with a magnitude of less than 1N. Similar to the experiment on a modified syringe, the base showed no signs of fatigue or cracking during delivery.

In vitro skin penetration is demonstrated on split-thickness (<0.5 mm thick) samples of dorsal swine skin using CNT-SU8 microneedles coated in dry methylene blue powder.

Microneedles were pressed by hand into the swine skin and achieved penetration at tip pressures in the range of 60MPa to 90MPa. Upon contact with the interstitial fluid in the skin, the methylene blue dye is passively released from the needle, marking the point of contact with the skin (Figure 5.8). The clear pattern of the 2 x 2 microneedle array indicates positive penetration and ultimately demonstrates that the CNT-SU8 composite has sufficient strength to achieve skin penetration. The two penetration marks on the left side of the sample show positively that the microneedles penetrated into the skin as can be seen by the local concentration of dye at the penetration sites. The two penetration marks on the right side of the sample show that the microneedles penetrated completely through the split-thickness sample with the light from the microscope shining directly through the sample. A ring of diffuse methylene blue can be seen around each penetration site.
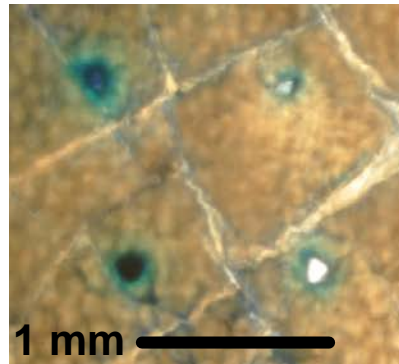
Figure 5.8- CNT-SU8 Microneedle Swine Skin Penetration. Microneedle coated with methylene blue prior to penetration. Sample imaged by stereomicroscope.

From these experiments, it is shown that all of the mechanical objectives of the microneedle outlined previously in Chapter 3 have been achieved. The size and material composition of the microneedle are appropriate for withstanding the applied pressure needed to achieve skin penetration. The lumen is unobstructed and supports fluid conduction. Hand actuation limits the magnitude of the applied delivery pressure on the system. However, from

these experiments, it is observed that the lumen is properly sized to limit hydraulic resistance. Large flow rates were observed under minimal pressure actuation for the case of delivery into the air. The SU-8 base mechanically supports the microneedles from substrate separation, device incorporation, to fluid delivery without tearing or cracking.

5.4.2 CNT-BOPDA Polyimide Microneedle

After verifying the individual components of delivery with the CNT-SU8 microneedle, the delivery experiments for the CNT-BOPDA polyimide microneedle focused on evaluating the combined performance of the CNT-BOPDA microneedle and the dual reservoir skin patch to achieve *in vitro* liquid delivery into swine skin. For these tests, a 3 x 3 array of microneedles were placed in the center of a 1cm x 1cm polyimide base and attached to the delivery platforms delineated in Section 5.2.

5.4.2.1 Delivery into the Air

Before testing in a delivery medium, the fluid conduction of the CNT-BOPDA microneedles and the dual reservoir skin patch assembly was verified. The CNT-BOPDA microneedles were first placed on a modified syringe to verify that significant flow rates could be achieved through the microneedles using hand actuation (Figure 5.9 a). Next, the CNT-BOPDA microneedles were tested on the dual reservoir skin patch. For delivery through the microneedles into the air, hand actuation of the skin patch resulted in a delivery rate of 340 µL/min over the microneedle array or 38 µL/min per needle (Figure 5.9 b). For syringe pump actuation using the syringe pump skin patch, a maximum flow rate into the air was observed of 1.3 mL/min over the array or 144 µL/min per needle. Beyond this flow rate, the pressure in the secondary reservoir pushing on the polyimide base caused the polyimide base to separate from the skin patch, causing fluid to be leaked in the space between the microneedle array and the skin patch.
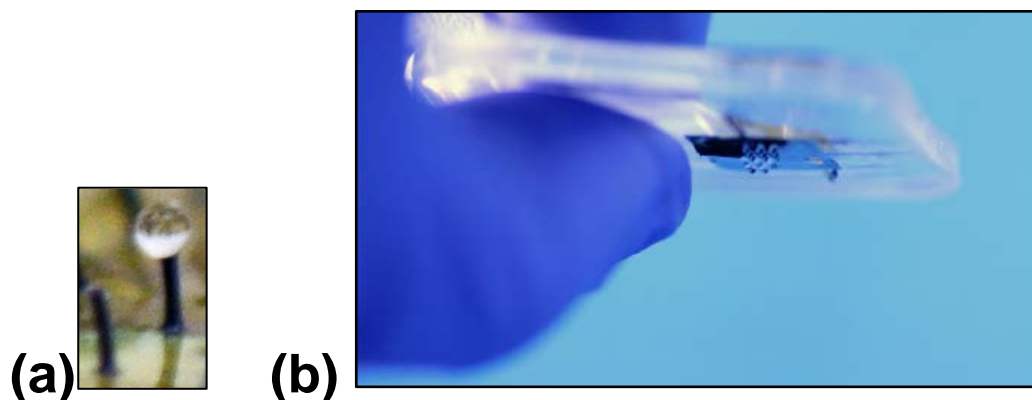
Figure 5.9- (a) Droplet on a single CNT-BOPDA microneedle. **(b)** Hand Actuation of CNT-BOPDA microneedle on Dual Reservoir Skin Patch Platform.

From these experiments, it is observed that like the CNT-SU8 microneedle, the CNT-BOPDA microneedle is capable of supporting significant flow volumes under hand actuation, as is expected since the CNT-SU8 and CNT-BOPDA microneedles have similar lumen diameters of 25 µm and 30 µm respectively. The maximum flow rate using a syringe pump is over three times higher than what can be achieved by hand actuation. Therefore, in considering the performance of the combined microneedle-skin patch system, the constraint on delivery pressure by using hand actuation is the limiting factor in determining delivery rate.

5.4.2.2 Delivery into Hydrogel

A 3 x 3 CNT-BOPDA microneedle array attached to the dual reservoir skin patch was tested by delivering an aqueous solution of methylene blue dye into hydrogel (1% agarose) and *in vitro* swine skin samples. Methylene blue readily spreads in hydrogel (1% agarose) such that any accidental delivery before the microneedles are fully inserted into the gel would result in dye flooding the surface. In this way, the use of the dual reservoir skin patch in minimizing accidental discharge, as described in Section 5.2.1.4, is assessed.
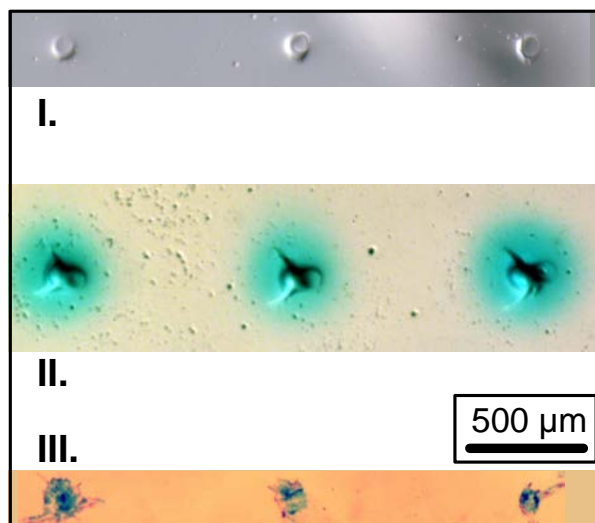
Figure 5.10- Compilation of microneedle penetration images. **I.** Penetration of hydrogel without fluid delivery. **II.** Delivery of methylene blue dye into hydrogel. **III.** *In vitro* delivery of methylene blue into swine skin.

The hydrogel was injected with approximately 15 µL of dye delivered simultaneously through nine microneedles in less than a minute through hand actuation. Comparison of images of hydrogel penetration without fluid delivery and hydrogel immediately after dye delivery show dye concentrated in the punctures made by the microneedles and diffusing into the hydrogel under the surface (Figure 5.10 *I, II*). Additionally, the surface of the hydrogel was blotted after delivery with a kimwipe to verify that all dye was delivered into the hydrogel and did not discharge onto the surface. From this, it is concluded that the microneedle-dual reservoir system achieves a positive delivery in hydrogel (1% agarose). Here, the data demonstrates the utility of the two-step delivery system used in the dual reservoir skin patch in preventing accidental discharge of fluid on the surface.

An additional delivery test was performed in hydrogel (4% agarose) using the CNT-BOPDA microneedles and the syringe pump skin patch. The goal of this test was to determine the

maximum deliverable volume over the span of 5 minutes and to assess the failure mode at the maximum deliverable volume. 4% agarose hydrogel was used, which provides significantly higher flow resistance than 1% agarose hydrogel. Here, the 4% variant is used as a laboratory model for swine skin. The maximum delivery volume was found to be 12.5 µL or 2.5 µL/min. Above this delivery rate, dye would flood the top surface of the hydrogel indicating that the delivery rate was faster than the absorption rate into the hydrogel.

5.4.2.3 Delivery Into *In Vitro* Swine Skin

In vitro skin penetration and delivery of methylene blue dye were achieved in full-thickness swine skin (Figure 5.10, *III*). Comparison of the penetration marks in swine skin with the control penetration marks in hydrogel show that the size of the penetration marks in swine skin is consistent with the diameter of the microneedles. In this way, it is determined that there is no lateral spread of the dye along the top layers of the skin, which confirms a positive penetration. The microneedles were pressed into the skin with a force per needle in the range of 1.1 N to 1.6 N to achieve a tip pressure of 140 to 210 MPa. Given the geometry of the microneedles, the applied force per needle was greater than the minimum force required to achieve skin penetration, as reported in previous work (Davis et al. 2004). To activate the drug flow, the primary drug reservoir was compressed with a finger force in the range of 0.7 to 1.0 N, resulting in delivery of approximately 4 µL into the skin over a 5 minute period. After penetration, the microneedles were imaged by scanning electron microscopy and did not exhibit any signs of buckling, breakage, or other structural damage (Figure 5.11). SEM images of the microneedles after penetration show that debris from the skin, including hair and skin particulates, is present on the microneedles and the polymer base. Given the small size of the microneedle and the release point of the lumen being susceptible to blockage, it is determined from this data that the microneedles represent a single-use delivery system.
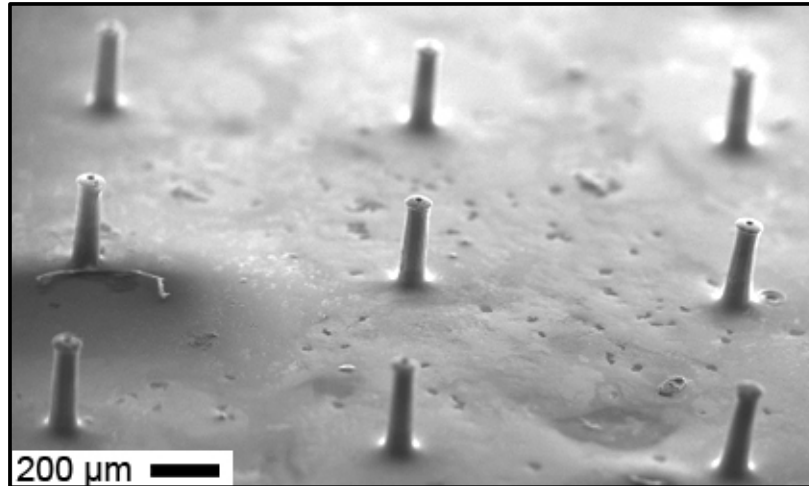
Figure 5.11- SEM image of CNT-BOPDA microneedle array after *in vitro* swine skin delivery.

5.4.2.4 Impulse Penetration

Previous studies using hollow silicon microneedles of similar dimensions to the CNT-polymer microneedles have shown that the use of an external applicator to achieve skin penetration can ultimately increase the delivery rate of the microneedles by over an order of magnitude (Verbaan et al. 2008). Moreover, hollow microneedles that are currently being developed for commercial applications have included external applicators as part of their final design (Burton et al. 2011). In addition to increasing the delivery rate, an impulse injection using an external applicator eliminates the variability from person to person of using hand force to directly actuate drug flow.

For this experiment, the CNT-BOPDA microneedles were placed in the impact penetration setup as described in Section 5.2.1.6. Delivery rates were tested in the range of 1 µL/min to 6 µL/min. The delivery was considered successful only if all methylene blue dye was delivered into the hydrogel. As a control, the lancet was removed and the microneedles were pressed into the hydrogel by hand actuation as described previously in Section 5.4.2.2. The

observation of dye spilling onto the surface of the hydrogel indicated that the delivery rate was too high to allow for proper absorption of the dye into the gel, as was seen in the control experiment in Section 5.4.2.2.
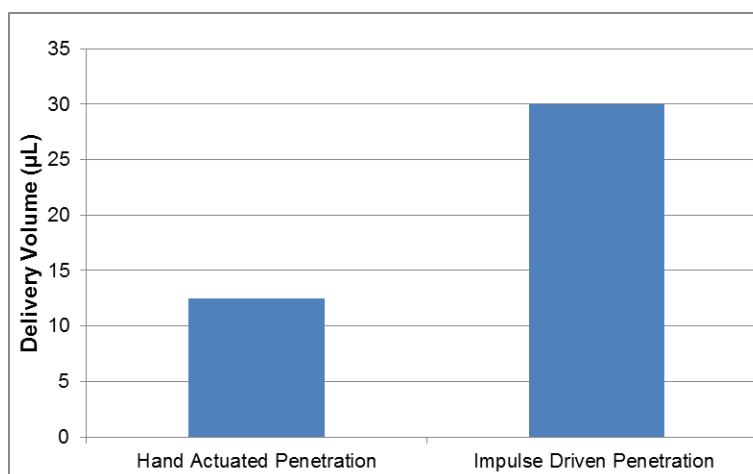
Figure 5.12- Increased deliverable volume in hydrogel (4% agarose) by impulse driven penetration.

Achievable delivery volume in a five minute delivery period was more than doubled from 12.5 µL using hand actuated skin penetration to 30 µL using the high-impact penetration approach (Figure 5.12). The effect of impact penetration is to increase the damage to the delivery medium at the injection site such that the resistance of the delivery medium is decreased. Since the penetration force is provided by a simple mechanical mechanism, it is envisioned that the impulse penetration method can be integrated into a skin patch of similar style as the hand actuated skin patches currently used.

5.5 Discussion

5.5.1 Fluid Throughput

A summary of the maximum delivery rate through the CNT-BOPDA microneedles is presented in Figure 5.13 for syringe pump actuation. In Chapter 6, delivery volume into *in vivo*

rabbit skin actuated by a syringe pump will be shown to have agreement with the data reported here for volume delivered under hand actuation into *in vitro* swine skin. Delivery rate through *in vitro* swine skin is similar in magnitude to hydrogel (4% agarose). Given the relative ease of preparing hydrogel along with the ability to reuse microneedles for hydrogel delivery, hydrogel is vetted as a good laboratory model for testing the fluid conduction of microneedle-skin patch system performance before progressing to animal models. Delivery into the skin models (*in vitro* swine skin and hydrogel [4% agarose]) has an order of magnitude lower delivery rate than delivery into the air. In the context of the flow model presented previously, it is clear that the main source of hydraulic resistance during delivery comes from the delivery medium rather than the microneedles.
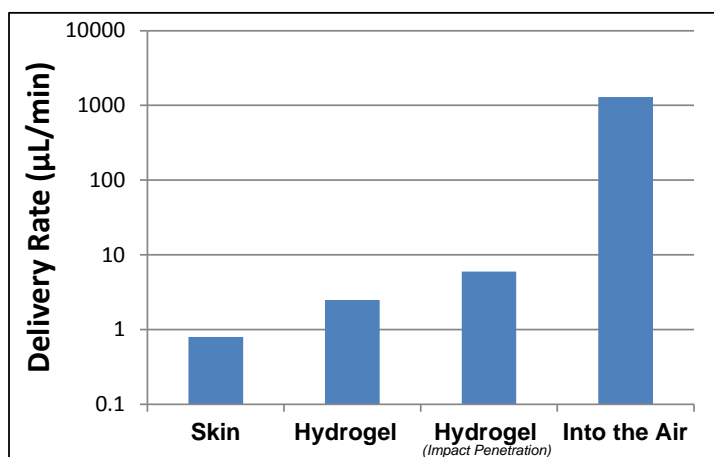
Figure 5.13- Delivery rates for a 3 x3 microneedle array in each delivery medium. Skin refers to both *in vitro* swine skin and *in vivo* rabbit skin. Hydrogel has a concentration of 4% agarose.

Previous work using hollow microneedles of the same height have shown similar or lower delivery rates into the skin (Table 6.1). A full discussion of comparable microneedle delivery systems is reserved until Section 6.4. Comparable delivery performance, as shown here, combined with the fabrication advantages outlined in Chapter 3, demonstrates that the CNT-polymer microneedle, regardless of specific delivery platform, is capable of being developed into a successful microneedle technology.

The CNT-BOPDA microneedles and other contemporary microneedle designs in the height range of 200 – 500 µm are typically limited to delivery volumes on the order of microliters (Table 6.1). The current challenge in the field of hollow microneedles is to increase the total delivery volume to the range of hundreds of microliters. By reaching this delivery threshold, liquid drug formulations that are currently administered by hypodermic injection can be more directly adapted to the hollow microneedle delivery architecture.

To further increase the delivery volume and rate of the CNT-BOPDA microneedles, a number of improvements can be made to either the microneedle or delivery platform. Options for modifying the delivery platform include replacing hand actuation with a micro or MEMS based pump that can allow for higher applied pressure, resulting in higher flow rates at the cost of increased price and complexity (Ma et al. 2006). Additionally, changing the mechanics of microneedle penetration, as discussed in terms of impact penetration versus hand actuation, has been shown here to reduce hydraulic resistance of the delivery medium to significantly increase the delivery rate. Previous work has shown that a spring-actuated delivery device, similar to the lancet used here, can be incorporated into an integrated delivery platform (Burton et al. 2011). Other methods that have been used in contemporary designs include slightly retracting the microneedles after skin penetration in order to create a low resistance cavity for injecting fluid into the skin (Wang et al. 2006).

Increasing the length of the microneedles, as described in Chapter 2, would allow for deeper penetration into the skin, leading to higher delivery rates as skin permeability increases in deeper tissues (Schmook, Meingassner, and Billich 2001). In comparing the CNT-polymer composite microneedles to other hollow microneedle designs, one major difference in terms of delivery pathway can be observed. Whereas the lumen of the CNT-polymer composite microneedle terminates on the top surface of the microneedle, most microneedle designs follow the design of the hypodermic needle with the lumen terminating on the side of the needle (Figure

3.4h) (Häfeli et al. 2009). A previous study examined microneedle-skin interaction in a finite element simulation to compare the release from a top-terminated lumen and a side-terminated lumen. Results from the simulation showed that the high pressure exerted on the skin at the tip of the microneedle restricts fluid delivery, whereas the relatively low pressure along the side of the microneedle provides a better conduit for transporting fluid from the needle into the skin (Roxhed et al. 2007). One option to include a side-terminated lumen to the CNT-polymer composite microneedles would be to micromachine the top of the needle after curing the polymer resin. Micromachining is used commonly in producing a sharpened tip for silicon and polymer microneedles. However, micromachining provides coarse control in assuring uniformity over large arrays of needles and limits scalability for large arrays (Baron et al. 2008).

An alternative approach, unique to CNT-polymer composite fabrication, can be used to create a side-terminated lumen without limiting scalability for large arrays. The height of VA-CNT arrays is very sensitive to a number of conditions during fabrication, including gas mixture and temperature during CVD as well as the thickness and composition of the catalyst. By creating a site specific defect in the catalyst, a side lumen can naturally be created by the stunted height of the VA-CNT array above the defective catalyst. Figure 5.14 illustrates this concept on a CNT scaffold. In this example, the defect was created by over-sonicating the sample during photoresist lift-off, which damaged a small segment of the catalyst ring.

Defects can also be engineered during catalyst patterning by depositing catalyst in two steps in order to use two photoresist masks to separately deposit a pristine catalyst and a defective catalyst. A defective catalyst can be achieved by either changing the thickness of the iron catalyst or by failing to deposit either the alumina or silicon dioxide buffer layers that support the iron catalyst. It is expected that this design is easily supportable through microneedle fabrication, as it has been shown that polymer resin conformally coats the CNT scaffold during processing, and no

changes are made to the intrinsic CNT structure that would affect the transport of polymer resin through capillary action.
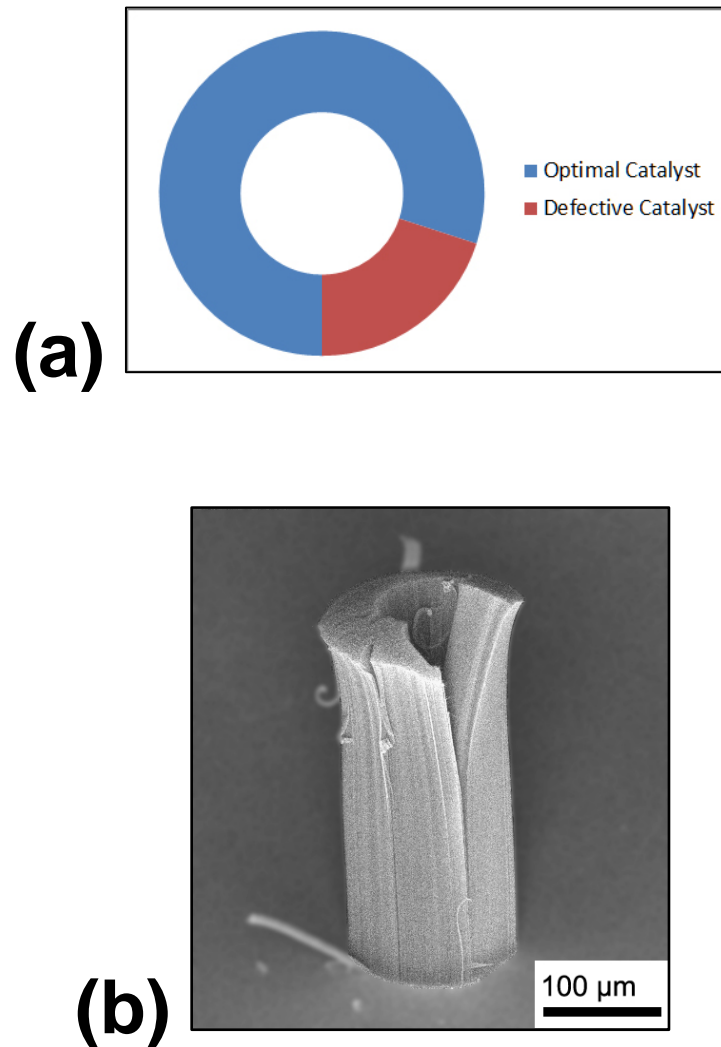
Figure 5.14- **(a)** Conceptual illustration of catalyst distribution on silicon wafer. **(b)** CNT scaffold with side-terminated lumen caused by the presence of site-specific defective catalyst.

5.5.2 Mechanics of Microneedle Penetration

A notable difference in the CNT-polymer microneedle compared to other designs is the simplicity of the geometry. Absent in the CNT-polymer microneedle is the typical tapered

geometry seen in most contemporary hollow microneedles (Roxhed et al. 2007). A tapered geometry is typically utilized to prevent buckling failure and fracture of the microneedle during skin penetration (Davis et al. 2004). However, the CNT-polymer composite microneedle has consistently demonstrated successful skin penetration without structural damage in the height range of 200-300 µm. However, when considering increasing the microneedle height or increasing the aspect ratio, a taper may need to be considered. General fabrication options for fabricating tapered microneedle geometry are considered in Section 3.4. Additionally, a study on utilizing oxygen plasma etching as a novel method to introduce a taper to CNT geometry is delineated in Chapter 7. Buckling failure of the microneedles during skin penetration was observed starting at a needle height of 500 µm for the CNT-BOPDA microneedles with standard outer and lumen diameters (Figure 5.15).
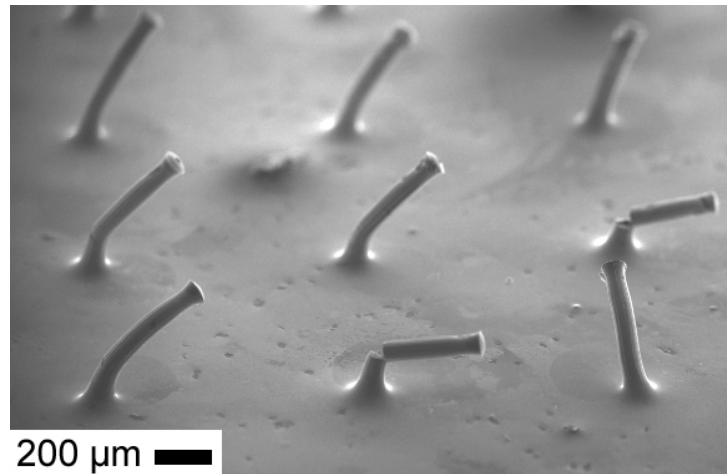
Figure 5.15- 500 µm tall CNT-BOPDA microneedles damaged after *in vitro* skin penetration test.

In considering the tip of the microneedle, previous study of similar blunt tipped microneedles has shown that the force required to penetrate the skin depends purely on the outer diameter of the microneedle tip rather than the surface area of the tip. This is because on the length scale of the diameter of the microneedle tip, the skin cannot locally deform into the lumen

as a mechanism to ease stress (Davis et al. 2004). This observation is important in showing that the requirements of achieving skin penetration and conducting fluid through the microneedle can be decoupled in the microneedle design, as the outer tip diameter determines the force required for penetrating the skin, whereas the lumen diameter determines the hydraulic resistance of the microneedle.

Many contemporary microneedle designs feature a very pronounced taper. This is especially true for silicon microneedles, where the brittle nature of silicon makes the needle particularly susceptible to fracture resulting in a complete break of the needle. In contrast, for the CNT-polymer composite microneedle, buckling failure does not necessarily result in needle breakage. As seen in Figure 5.15, 2 out of 9 microneedles are severely broken, with the top section of the microneedles attached by the thinnest of margins. The rest of the microneedles show deformation in shape but remain intact and attached to the polyimide base. This difference in failure mode is important in assessing patient safety, as a needle material susceptible to fracture and breakage is more likely to become lodged in the patient rather than a needle that deforms but remains attached to its delivery platform.

A potential advantage to not having a taper in the CNT-polymer composite microneedle is the ability to penetrate deeper into the skin for a given microneedle height. The increasing diameter of a pronounced taper limits the overall penetration depth of a microneedle. In a previous study, silicon microneedles with a pronounced taper and a total needle height of 200 µm were shown to have a penetration depth limited between 60 µm and 70 µm (Häfeli et al. 2009). In comparing the penetration depth to the geometry of the microneedle, it can be observed that the penetration depth is coincident with the slender, cylindrical tip of the microneedle before the diameter of the needle begins to increase with the taper. Thus in this instance, it is observed that the taper is the limiting feature that inhibits further penetration of the microneedle. Without the presence of a taper, or similar diameter broadening geometry, to limit penetration depth, the

CNT-polymer microneedle is predicted to have a greater penetration depth than contemporary microneedles of similar lengths. A conservative estimate for penetration depth of the CNT-polymer microneedle is 100 – 125 µm, or 30-65 µm greater penetration depth than the silicon microneedle.

In relying on hand actuation to press the microneedles into the skin, the number of microneedles that can be supported is limited. For the CNT-BOPDA microneedles, a compression force in the range of 1.1 to 1.6 N per needle is applied to achieve skin penetration for a total force of 9.9 to 14.4 N. Maximum sustainable finger force is limited to 35 N for a healthy adult (NASA 1995). Taking into account the goal of universal accessibility, an upper limit of penetration force is estimated to be approximately 17 N (50% maximum finger force). In this case, hand forced skin penetration limits the number of CNT-BOPDA microneedles on a single device to 10 – 15 microneedles. The limit on the number of needles ultimately limits the deliverable volume, as each microneedle operates as an independent conduit for delivery into the skin. Thus, an external applicator, similar to the lancet used here for impact penetration, may become necessary for applications requiring large delivery volumes from a large array of microneedles.

5.6 Conclusions

The utility of the CNT-polymer composite microneedles has been shown through liquid delivery experiments in hydrogel as well as *in vitro* liquid delivery in swine skin. Performance of the CNT-polymer microneedles was demonstrated on a variety of delivery platforms, including modified syringes, hand actuated skin patches, and pump actuated skin patches. The microneedles were portable to a variety of drug delivery platforms due to the thin, flexible nature of the polymer base. From the cumulative ensemble of delivery experiments, no failure of the polymer base, such as cracking or tearing, was observed. This result demonstrates that the thin SU-8 and polyimide bases are mechanically supportive of the microneedle array during delivery.

The design of the microneedles was sufficient for supporting delivery under the limited forcing constraints of hand actuation for both skin penetration and fluid flow. The dual reservoir skin patch, as tested with the CNT-BOPDA microneedles, was shown to provide a unique architecture to avoid accidental discharge of drug by separating the action of microneedle insertion into the skin and fluid actuation. In comparing delivery into the skin and delivery through the microneedles without a delivery medium (into the air), it was found that the delivery rate into the air is over three orders of magnitude higher than the delivery rate into the skin. From this result, it can be concluded that the predominant source of hydraulic resistance during delivery is not the size of the microneedle lumen but rather the hydraulic resistance of the skin. Future strategies and work to reduce the hydraulic resistance presented by the skin will need to focus on how the microneedle interacts with the skin upon insertion.

Deliverable volume into the skin is comparable to similar to contemporary microneedles of the same length. Several approaches to separately improve the skin patch and the microneedle were investigated with the goal of further improving the delivery volume and rate. For the skin patch, replacing hand forcing with an external applicator to drive the microneedles into the delivery medium was shown to increase total deliverable volume. For the microneedle, increasing the length of the microneedle and moving the termination point of the lumen from the top surface to the lateral surface are considered as future strategies for increasing delivery volumes.

Ultimately, by showing here that the microneedles can deliver drug into the skin combined with the simplifications in fabrication as discussed in Chapter 3, the CNT-polymer composite architecture is vetted as a potential microneedle technology. The portability of the CNT-polymer microneedle by a thin polymer base along with the flexibility in microneedle geometry, facilitated by the bottom-up fabrication method, can facilitate the expansion of the CNT–polymer architecture to a wide range of drug delivery platforms.

Chapter 6

In Vivo Delivery

6.1 Introduction

In Chapter 5, different configurations of microneedles and delivery systems were investigated. Here, a single configuration of CNT-BOPDA composite microneedles attached to a hand actuated dual reservoir skin patch is used as a case study for fentanyl delivery in New Zealand White Rabbits. In contrast to the previous chapter that focused on the physical aspect of delivery of both the microneedles and the skin patch, the focus here is on the microneedle-skin patch system as a whole and its ability to deliver drugs systemically.

The objectives of this study are to:

- Determine the onset of action for microneedle delivery of fentanyl (time between application and systemic detection).

- Assess deliverable drug volume as compared to *in vitro* experiments.

- Determine if the microneedle injection is qualitatively painless.

- Assess the ability to successfully administer microneedle trandermal patch to a live animal model and assess damage to the microneedles, if any, after delivery.

The scope of the *in vivo* delivery experiment is not a comprehensive pharmacokinetic study, but rather to collect baseline information on the delivery rate of microneedles compared to standard

drug application routes such as topical and hypodermic injection, and assess the ease in which a hand actuated microneedle patch can be applied to a live subject.

Fentanyl is a highly potent opioid analgesic, with a potency 50 to 100 times higher than morphine (Mather 1983). Fentanyl can be administered by multiple methods, including hypodermic injection and topical patches (Hess, Stiebler, and Herz 1972; Foley et al. 2001; Mather 1983). Fentanyl is chosen for the *in vivo* study, as the high potency of fentanyl does not require the delivery of large drug volumes, and can thus be successfully delivered despite the delivery volume limitations of microneedles discussed in Chapter 5. Fentanyl is absorbed systemically, allowing for the delivery to be characterized in time by taking blood samples throughout the experiment to measure the concentration of fentanyl in the blood plasma. Fentanyl is highly dissolvable in water up to a maximum concentration of 25 mg/mL, allowing for delivery of an aqueous solution similar to prior laboratory and *in vitro* experiments. Furthermore, the commercial availability of fentanyl topical patches and injectable aqueous solutions allow for direct comparison of microneedle delivery with topical and subcutaneous hypodermic delivery.

The overall systemic delivery for the microneedles is expected to be a hybrid of hypodermic injection and a topical skin patch. The microneedles have the same quick application time as hypodermic injection, while incorporating the painless aspect of a topical skin patch. Given the length of the microneedles, the microneedles are expected to pass through the stratum corneum and deliver drug into the epidermis at a depth below the skin surface of 70-120 µm. From the point of delivery, the drug diffuses into deeper tissues in the dermis and subcutaneous layers. The high abundance of blood vessels in the deeper tissues provides the most direct route for systemic drug absorption (Figure 6.1). Given that the hypodermic injection places drug directly in the subcutaneous layer, it is expected that hypodermic injection will have the quickest systemic onset of action compared to topical and microneedle delivery, which rely on diffusion to reach deeper tissues and a sparser network of blood vessels in the upper layer of the dermis.
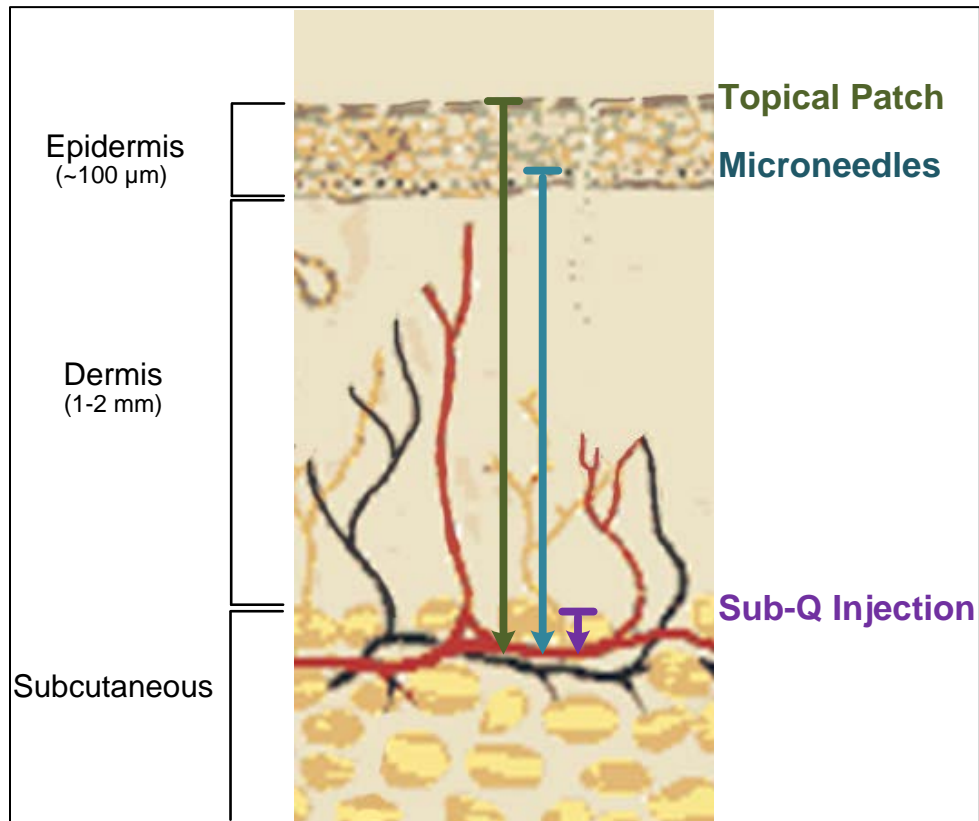
Figure 6.1- Illustration of the different layers of skin, the injection depth for each delivery method, and distance from injection point to blood vessels in the subcutaneous layer. (Adapted from Health and Safety Executive, United Kingdom, 2014).

New Zealand White Rabbits are chosen as the animal model, as the size of the animal allows for multiple blood samples to be collected over the course of the experiment. The delivery of fentanyl citrate on rabbits has been well-characterized in previous studies and is commonly used as a model for subsequent *in vivo* human delivery characterization (Hess, Stiebler, and Herz 1972; Foley et al. 2001). The fentanyl dose typically used for a 4 kg rabbit in veterinary applications is similar to that for a human infant, making the data collected in this study relevant for future investigations of using microneedles for *in vivo* delivery on humans. One drawback to using rabbits is that the morphology of the skin is different from human skin due to the high

concentration of hair follicles on the rabbit skin (Foley et al. 2001). Due to its mechanics and composition, swine skin, as used in Chapter 5, is generally considered the best model for assessing microneedle penetration. However, due to the high volume of previous work linking fentanyl data delivery in rabbits to delivery in human patients, rabbits were deemed the most suitable model for the *in vivo* study.

6.2 Materials & Methods

All experimental methods described within were approved by the California Institute of Technology Institutional Animal Care and Use Committee (IACUC).

6.2.1 Microneedle Preparation

Dimensions of the CNT-BOPDA composite microneedle are consistent with what has been described to present. Nine microneedles are patterned into a 3 x 3 microneedle array with 1 mm spacing between needles. The outer and luminal diameter of the microneedles were 100 and 30 µm respectively. Microneedles used in this experiment have a length in the range of 210 – 230 µm, with the standard deviation in height in a single array averaging 9 µm. A 15 nm thick layer of platinum/palladium is sputter coated onto the microneedles to allow for imaging of the microneedles before and after the *in vivo* experiment. Dual reservoir skin patches, as described in Section 5.2.1.4, are used as the delivery platform.

Before mounting to skin patches, microneedles are imaged in SEM to verify the microneedle dimensions, ensure uniformity between the needles, and to verify the absence of any anomalous defects. After the *in vivo* experiment, microneedles are separated from the skin patch with a razor blade and reimaged under SEM. Comparison of SEM images taken before and after the delivery experiment are used to assess whether the microneedles sustained any damage during the delivery.

After affixing microneedles using methods described previously, the skin patch is filled with the aqueous fentanyl solution through the syringe adapter on the side of the skin patch. The skin patch is tested by squeezing the primary drug reservoir to release a small amount of drug to verify flow through all 9 microneedles on the skin patch. After testing the flow, the primary drug reservoir is replenished, and the surface of the microneedles is wiped dry with a kimwipe. Finally, the filled skin patches are weighed on an analytic balance with a precision 0.1 mg (AGCN100, Torbal Scales, Clifton, NJ). Skin patches are weighed again after delivery to determine the amount of drug that was delivered during the experiment, which allow the deliverable volume to be measured with a precision of 0.1 µL.

6.2.2 Fentanyl Delivery

Six female New Zealand White Rabbits (Charles River, Wilmington MA) were assigned randomly to three groups. Two rabbits were assigned to the microneedle experimental group, two rabbits were assigned to the topical skin patch control group, and two rabbits were assigned to the hypodermic injection control group. The delivery experiment was performed in 2 rounds. During each round, each animal received a single dosage of fentanyl by the predetermined delivery method. The animals had a rest period of 1 month between rounds to allow for the natural elimination of any traces of fentanyl. Each rabbit was examined by a veterinarian to verify the rabbit was in good health before proceeding with each delivery experiment. During the first round of delivery experiments, the rabbits were 13 weeks old and had an average weight of 2.80 ± 0.13 kg. During the second round of delivery experiments, the rabbits were 18 weeks old and had an average weight of 3.53 ± 0.20 kg.

Fentanyl was delivered on the dorsal side of the rabbit near the spine of the rabbit for each delivery group. To prepare the delivery site, hair was removed in an approximate 8 cm x 8 cm area for all rabbits. The majority of hair is removed with hair clippers. The remaining hair is

removed by applying Nair Hair Removal topical solution for several minutes and then rinsing the skin (Nair, Church & Dwight CO, Ewing, NJ). The Nair treatment was observed to produce a mild inflammatory response in the skin that was unrelated to the fentanyl delivery.

For topical patch administration, a commercial fentanyl patch (Duragesic Fentanyl Transdermal System, Janssen Pharmaceuticals, Titusville, NJ) of dosage 12 µg per hour is applied to the shaved dorsal skin of the rabbit (Figure 6.2) for the duration of the experiment, 8 hours. As Figure 6.2 shows, a small residual amount of fur is still present on the rabbit after the hair removal process. The fentanyl patch is specifically positioned to minimize contact with residual fur, as the presence of fur under the patch can affect the delivery rate into the skin (Foley et al. 2001).
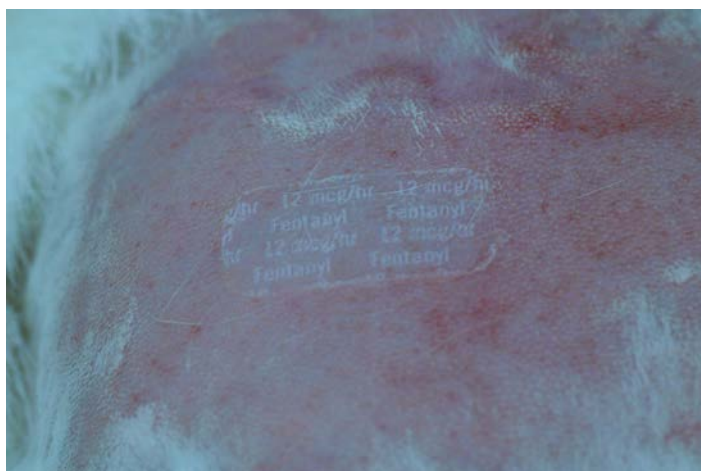
Figure 6.2- Fentanyl patch on rabbit skin.

For hypodermic injection, a commercial aqueous fentanyl solution of concentration 50 µg/mL was used (Baxter Healthcare Corporation, Deerfield, IL). The target dosage for hypodermic injection was 12.5 µg per kilogram body weight, which is far below the maximum intravenous dosage for a rabbit (Foley et al. 2001). Prior to delivery, topical EMLA cream (2.5% lidocaine, 2.5% prilocaine) was applied to the injection site in order to numb the area. To ensure

delivery into the subcutaneous layer of the skin, the dorsal skin was pinched together and then injected with the hypodermic needle.

The microneedle skin patch is assembled as delineated in Section 6.2.1. Like the hypodermic injection, a target dosage of 12.5 µg per kilogram body weight was used. A concentrated aqueous fentanyl solution was prepared from fentanyl citrate salt (Sigma-Aldrich, St. Louis, MO) for microneedle application. This method was used to prepare the microneedle sample since the commercially available fentanyl solution designed for hypodermic injection requires injection volumes on the order of 700- 950 µL, far beyond the delivery capability of the microneedles as shown during *in vitro* skin delivery tests. For the first round of delivery experiments, the fentanyl concentration was set to 3.6 µg/ µL for a target delivery volume of 10 µL. For the second round of delivery experiments, the fentanyl concentration was increased to 11.17 µg/ µL to allow for a smaller delivery volume of 4 µL.

For applying the microneedle patch to the skin, the patch is placed along the center of the rabbit's back to ensure good contact with the skin. Similar to placing the topical patch, the microneedle patch is placed away from residual hair to avoid delivery occlusion. Using the dual reservoir skin patch, the microneedles are first inserted into the skin using the force of a single finger. After insertion, a second finger is used to actuate the primary drug reservoir to begin drug flow. From previous *in vitro* experiments, it is expected that the delivery is completed within 5 minutes. To ensure maximum deliverable volume, the patch is held in place for 10 minutes. After 10 minutes, the primary drug reservoir is released while continuing to hold the microneedles affixed to the skin. After an additional minute, the finger holding the microneedles in the skin is released and the skin patch is removed from the rabbit. The surface of the skin is inspected visually and wiped with a kimwipe to check for any residual drug not absorbed by the skin.

Blood collection was facilitated by an intravenous butterfly catheter placed in the marginal ear vein of the rabbit before the experiment. Rabbits were placed in an Elizabethan collar for the duration of the experiment to prevent the animal from disturbing the catheter. The catheter was secured to the rabbit by wrapping the ear and catheter together in bandaging tape (3M Vetrap Bandaging Tape, Saint Paul, MN). 3 mL of blood was collected from each rabbit at 6 time points: before fentanyl application and then 15 minutes, 30 minutes, 60 minutes, 2 hours, and 8 hours after application. During blood collection and fentanyl administration, rabbits were wrapped in a large towel and manually restrained. Blood samples were tested for the presence of fentanyl through ELISA (enzyme-linked immunosorbent assay) analysis performed by an external laboratory (AniLytics, Gaithersburg, MD). The ELISA analysis had a minimum detection limit of 0.013 ng/mL.

6.2.3 Saline Syringe Pump Delivery

To verify the delivery volume obtained during the fentanyl trial, a follow-on study was performed using the CNT-BOPDA microneedles with the syringe pump skin patch as described in Section 5.2.1.5. Fentanyl was replaced with a 0.9% saline solution, such that the delivery volume could be modified without concern for the medicinal effect on the rabbit (Abbott Laboratories, Abbott Park, IL). A rabbit was chosen randomly from the 6 rabbits used during the fentanyl trial. Before beginning the saline trial, the rabbit was given a minimum 1 month rest period. Total delivery time was set for 5 minutes, and the saline was flowed at a continuous rate. Successful delivery was determined by examining the skin after delivery to ensure that saline did not pool on the skin surface and that the skin patch did not leak during delivery, which would indicate a significant buildup of back pressure caused by the high hydraulic resistance of the skin.

6.3 Results

Each delivery mechanism was tested four times over the course of two rounds of fentanyl delivery experiments. Figure 6.3 shows the onset of action for each delivery group. Onset of action is defined as the time between fentanyl application and the time it is first measured in the blood plasma. Dashed lines represent the scheduled blood sampling times delineated in Section 6.2.2. Deviation from the scheduled blood sampling times represents the actual blood sampling time during the experiment. The onset action is defined as a range between blood sampling times where the closed marker indicates the first positive measurement of fentanyl in blood plasma, and the open marker indicates the previous negative measurement of fentanyl in plasma. The precise onset of action is presumed to occur somewhere along the highlighted range.
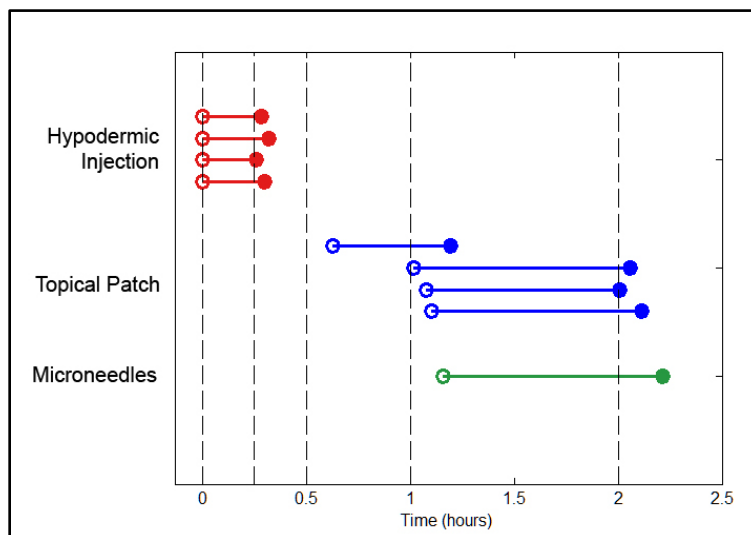
Figure 6.3- Onset of action for fentanyl as determined by time between fentanyl application and first detection of fentanyl in plasma. Open circle represents last negative measurement of fentanyl in plasma. Closed circle represents first positive measurement of fentanyl in plasma. Dashed black line represents scheduled blood sampling times.

Hypodermic injection has an almost instantaneous onset of action, with the first plasma sample taken at 15 minutes showing a non-zero fentanyl application for all 4 delivery

experiments. The near instantaneous result is expected, as fentanyl is injected directly into the subcutaneous layer and agrees with previous results (Hess, Stiebler, and Herz 1972). The topical patch has an onset of action between 1-2 hours for three patches, and an onset of action between 30 minutes to an hour for 1 patch. For the experiment with the early onset of action, a more pronounced inflammatory response was observed from the Nair pretreatment. Previous work has shown that damage to the outer layers of skin caused by an overaggressive Nair treatment can result in an increased transport rate through the skin (Foley et al. 2001). Therefore, the onset of action is determined to be between the nominal 1 hour and 2 hour blood sampling times for the topical patch group.

Four microneedle patches were tested during the *in vivo* experiments. For the first round of experiments, the concentration of the fentanyl solution was targeted for a delivered drug volume of 10 µL. Actual released drug volume was determined to be 4 µL. Due to the underdosing of fentanyl and the sensitivity limits of the ELISA kit, no traces of fentanyl were detected in the plasma for the first experiment cycle. In the second round of experiments, the concentration of the fentanyl solution was increased to target a 4 µL dose, as discussed in Section 6.2.2. Of the two microneedle deliveries in the second round experiments, one microneedle delivery failed due to bad skin contact with the rabbit during the experiment. During delivery, the rabbit moved, causing the microneedles to lose contact with the skin. For the successful delivery in the second round, the onset of action was found to be between 1-2 hours, the same range as the topical patch.

A large time range is investigated, as the onset action for microneedles has not been well-characterized in previous work. Furthermore, this investigation represents the first *in vivo* experiments to deliver fentanyl through a microneedle. Now that the approximate onset of action times are defined for each delivery mechanism, future experiments can focus in the 1 to 2 hour

range to determine conclusively whether microneedles or topical patches have a faster onset of action.

The general agreement of onset action for microneedles and topical patch is expected, as the diffusion length from the epidermis to the subcutaneous layer is on the order of millimeters, and the difference in starting depth in the skin between the microneedles and topical patch is less than 100 µm. The fentanyl plasma concentration of the skin patch and the microneedles is shown at the observed onset of action (2 hours after application) in Figure 6.4. The fentanyl concentration of the topical patch is 0.076 ± 0.005 ng/mL whereas the fentanyl concentration of the microneedles is 0.063 ng/mL, which is 83% of the topical patch concentration. The measured fentanyl concentrations were consistent with results seen in previous rabbit model studies on topical fentanyl delivery (Foley et al. 2001).
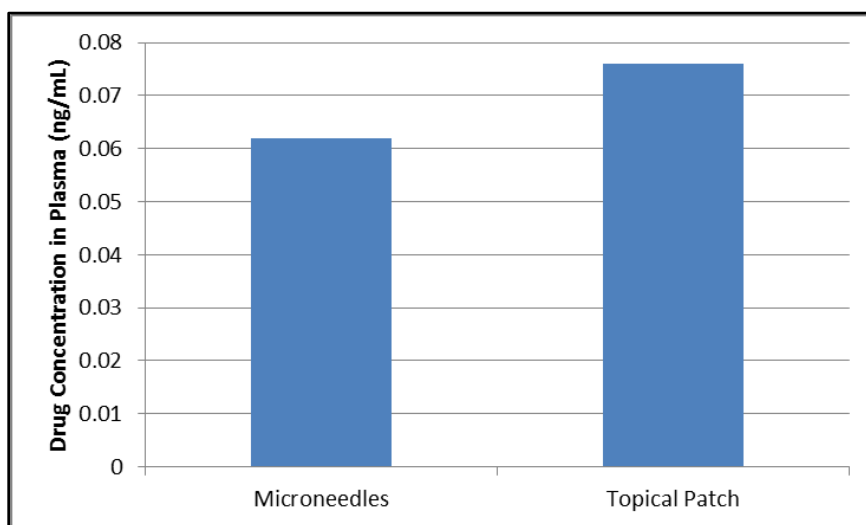

Figure 6.4- Measured fentanyl concentration in blood plasma at onset of action.

An important consideration in comparing the topical patch to the microneedles is that the commercial topical patch contains diffusion enhancers, which act to reduce the onset of action compared to a standard aqueous fentanyl solution, which is used in the microneedle patch. The

molecular weight of fentanyl citrate, 0.528 kDa, is quite small compared to large molecule drugs like insulin, with a molecular weight of 5.8 kDa. While small molecular drugs, like fentanyl, are able to slowly diffuse through the skin in a manner of hours, large molecular drugs like insulin are unable to cross through the stratum corneum layer of the skin, which is the outer layer of skin. Therefore, large molecule drugs are dependent on a transdermal delivery system, like microneedles or hypodermic injection, to overcome this boundary.

Thus, the primary objective of this experiment is not to show a more rapid onset of action over a topical patch for fentanyl, but rather that the CNT microneedle-skin patch system successfully delivers drugs into the epidermis and allows for diffusion into deeper tissues. For small molecule drugs that can be delivered through topical patches, a distinct advantage demonstrated is that while topical patches need to be worn over the course of hours to achieve drug absorption into the skin, the microneedle skin patch only needs to be applied over the course of 5-10 minutes to have the same effect. In essence, instead of having a drug reservoir on the topical patch, the CNT microneedle-skin patch creates a small reservoir of drug in the epidermis, allowing the external patch to be removed within minutes rather than hours.

Figure 6.5 shows a CNT microneedle array before (a,b) and after (c,d) *in vivo* delivery. As before for *in vitro* swine skin delivery, no notable damage is seen on any of the microneedle samples after *in vivo* rabbit skin delivery. Skin debris is readily identified on the polymer base as well as along the side of the microneedle (c). The presence of large skin debris relative to the size of the microneedle limits the use of the microneedles to a single-use device to avoid the risk of possible occlusion of the microneedles.

In regard to pain associated with injection, rabbits did not tolerate hypodermic injection. Rabbits held by manual restraint consistently flinched when contacted with the hypodermic needle. This allowed the rabbit to break free of restraint and did not allow for the injection to be

administered. Rabbits needed to be given a pretreatment of EMLA cream, as described in Section

6.2.2, to numb the injection area in order for the injection to be administered successfully. The

dermal patch, as expected, did not produce any pain upon application. Due to the presence of the

Elizabethan collar on the rabbit during the experiment, it was unclear whether the patch was a

source of irritation to the rabbit, as the collar restricted the rabbit from scratching or biting the

patch. Rabbits readily accepted microneedle injection for the duration of the 10 minute

application. Rabbits were manually restrained during injection and did not physically respond to

the microneedles. This result is expected, as microneedles of similar and greater lengths have

been shown in previous studies to produce minimal or no pain sensation (Haq et al. 2009).
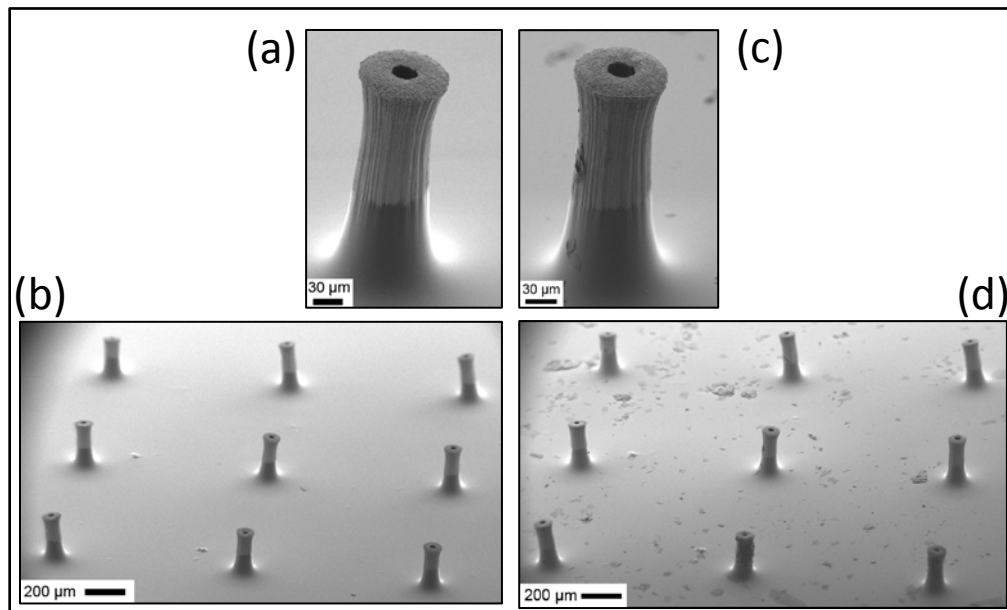
Figure 6.5- SEM Images of microneedles before **(a,b)** and after **(c,d)** delivery. Skin debris is present on the microneedles after delivery, but the microneedles do not sustain any structural damage.

In order to assess possible skin irritation caused by the microneedles, the injection site

was imaged before delivery, immediately after delivery, and 8 hours after delivery. Figure 6.6

shows a microneedle injection site and the surrounding region 8 hours after delivery. Non-site-

specific irritation can be seen, as the skin is generally inflamed as a result of the Nair treatment, similar to what was observed in Figure 6.2 for the rabbit undergoing fentanyl delivery through a topical patch. At the specific microneedle injection site, no secondary irritation to the skin is observed. For all microneedle treatments, no skin irritation was present 8 hours after delivery. Immediately following delivery, a vague imprint of the polyimide base could be seen in the rabbit skin for a couple of cases, but this imprint quickly vanished within the course of an hour.

The combined lack of pain and skin irritation seen in this *in vivo* study is promising, considering that the CNT-BOPDA polyimide composite microneedle represents a new material that has never before been used for skin penetration. These results are significant in demonstrating that the CNT-polymer composite can be considered a viable microneedle platform not only in terms of physical dimensions and material strength but also in terms of compatibility with transdermal delivery.
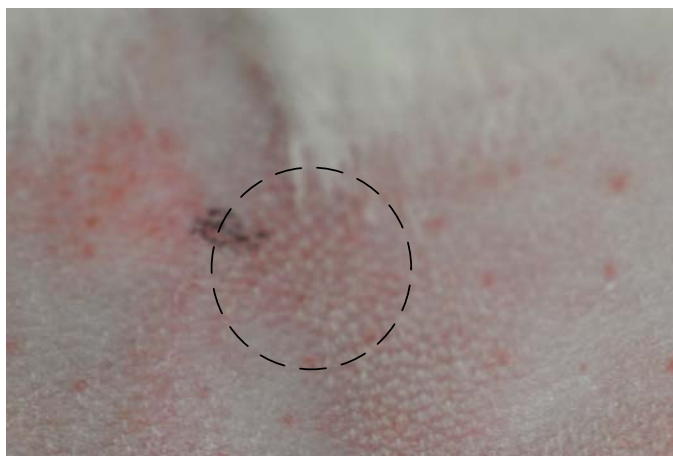
Figure 6.6- Rabbit skin, 8 hours after microneedle application (circled region). No observation of microneedle specific skin irritation.

The deliverable volume of 4 µL observed in the fentanyl delivery trial using the dual reservoir skin patch was verified using the same design of CNT-BOPDA microneedles on a

syringe pump skin patch. Constant flow rates of 500nL/min, 800nL/min, and 1 µL/min were applied for 5 minutes, for total delivery volumes of 2.5 µL, 4 µL, and 5 µL respectively. Positive delivery was observed for 2.5 µL and 4 µL. At 5 µL, a leak was observed in the syringe pump skin patch, which is indicative of significant backpressure resisting the saline flow into the skin. Thus, 4 µL over 5 minutes is viewed as a maximum volume for the microneedle-skin patch system. While the rate of 800nL/min is presumably stable over longer time periods, it is envisioned for practical applications that a manually actuated skin patch has a limit of 5 minutes for a patient to continuously provide actuation force to the patch.

6.4 Discussion

Previous studies using hollow microneedles in the same length range (200-500 µm) as the CNT-polymer microneedles have shown similar results to the CNT microneedle-skin patch system in terms of onset of action and delivery rate. Gardeniers et al. reports preliminary data using microneedles of length 350 µm to show the presence of diclofenac in the blood plasma only after 6 hours of continuous delivery. The same study also repots the delivery of insulin through the same microneedles at a steady delivery rate of 1U/hr (10µL/hr). For insulin delivery, microneedles of height 350 µm took slightly under 2 hours to achieve a 20% reduction blood glucose level, whereas microneedles of height 150 µm took approximately 2.5 hours (Gardeniers et al. 2003). Davis et al. also examines insulin delivery comparing transdermal microneedles of height 500 µm to topical delivery. In this study, the peak reduction of the blood glucose level for the microneedle delivery occurs 4.5 hours after application, compared to 6 hours for topical delivery (Davis et al. 2005). From these studies, it is observed that the onset of action for systemic absorption from hollow microneedle delivery is consistently in the range of hours.

Therefore, in evaluating the future role of hollow microneedles, it is observed that although the hollow microneedles physically resemble a hypodermic injection, the onset of action

for systemic absorption of the microneedles is more akin to an accelerated topical patch. This is to be expected, as the short length of the microneedles is designed to bypass only the first few layers of the skin, the stratum corneum, which provide the largest impedance for drug transfer, especially for large molecule drugs (Figure 6.1) (Prausnitz, Mitragotri, and Langer 2004). In this sense, hollow microneedles provide a head start past the more tortuous layers of the skin, but the primary delivery mechanism of diffusion into deeper tissues remains unchanged.

Rapid onset of action (< 1 hour) from a microneedle delivery is most likely restricted to applications where the target delivery site is in the skin at or near the injection site where long range diffusion is not required. This has been demonstrated in a previous study examining the delivery of lidocaine on coated microneedles to achieve local analgesia. Lidocaine, when applied as a topical cream (such as EMLA cream as used here as a pretreatment before hypodermic injection), has an onset of action ranging from 1-2 hours when used as a pretreatment for local medical procedures in the skin. In contrast, lidocaine coated microneedles were able to achieve the same analgesic effect with an onset of action of under a minute (Zhang et al. 2012) .

The current pairing of the CNT-polymer microneedle array with a hand actuated skin patch generally results in low delivery rates into the skin. However, the results are comparable to previous results using hand actuated skin patches and microneedles of similar height (Häfeli et al. 2009). 5 minutes is taken as the nominal application time for the CNT-polymer microneedle consistent with the results from the *in vitro* study presented in Chapter 5. However, by hand actuating the deformable drug reservoir with constant force, it is expected that the applied pressure in the drug reservoir decreases as the reservoir begins to drain. Therefore, the delivery rate is expected to decrease over the course of delivery. In this case, it is likely that the drug delivery is complete before the total 5 minute application time, which would result in the CNT-polymer microneedles having a delivery rate similar to what is reported in the Häfeli et al. study.

Reference	Drug	Number of Needles	Needle Height (µm)	Application Time	Total Drug Volume (µL)	Delivery Rate (µL/min)	Delivery Rate per needle (µL/min)
CNT/BOPDA	Fentanyl	9	219	5 min (nominal)	4	0.8	0.089
Hafeli et al.	Albumin	6	200	1 minute	3.2	3.20	0.53
Roxhed et al.	Insulin	21	400	3 hours	6	0.03	0.0014
Gardeniers et al.	Insulin	36	350	6 hours	60	0.17	0.0047
McAllister et al.	Insulin	16	500	30 minutes	5	0.17	0.011

Table 6.1- *In vivo* microneedle delivery data for microneedles of length 200-500 µm.

Table 6.1 summarizes *in vivo* delivery data for hollow microneedles in the length range of 200 µm to 500 µm. The results show that the delivery rate obtained *in vivo* for the CNT-polymer microneedles is quite high compared to similar microneedles. Improvements in delivery rate for the CNT microneedle-skin patch system can continue to be made using some of the strategies outlined in Section 5.5, including the use of an external applicator and incorporating a side-terminated lumen in the microneedle design. Even with these improvements, the global data on drug delivery for hollow microneedles under 500 µm demonstrates consistently that the platform is best suited for delivery of highly-concentrated drugs with minimal volume.

6.5 Conclusions

In vivo drug delivery of the CNT-BOPDA composite microneedle and dual reservoir skin patch was investigated in delivering fentanyl transdermally to New Zealand White Rabbits. The onset of action time of the microneedles was found to be of the same approximate time as commercial topical fentanyl patches. At the onset of action, microneedles and skin patch delivered a similar systemic dose of fentanyl, with blood plasma concentrations of 0.063 ng/mL

and 0.076 ng/mL respectively. Inspection of the microneedles before and after delivery demonstrated that the microneedles did not sustain any damage during delivery. Inspection of the injection site on the rabbit up to 8 hours after injection did not indicate any signs of skin irritation that can be directly correlated to the microneedle delivery.

In assessing discomfort during delivery, rabbits tolerated the microneedle injection with no observable signs of pain and discomfort. In contrast, rabbits unanimously did not tolerate a direct hypodermic injection of fentanyl without pretreating the injection site with a local topical analgesic. This indicates that the CNT-polymer microneedle achieves a painless delivery, which is consistent with contemporary hollow microneedle architectures. The delivered drug volume into the skin utilizing the hand actuated dual reservoir skin patch was 4 µL. The deliverable volume was verified in follow-on experiments injecting saline using the syringe pump skin patch variant of the dual reservoir patch. The CNT-BOPDA microneedle and dual reservoir skin patch achieves high delivery rates compared to contemporary microneedle designs of the same needle length.

This investigation has demonstrated the ability of the combined CNT-polymer microneedle and hand actuated skin patch system to function as a transdermal drug delivery platform. While microneedles and topical patches were shown to have similar onset of action for fentanyl, the application of this result is restricted to small molecule drugs. Delivery of large molecule drugs through topical patches is impossible due the restrictive permeability of the stratum corneum. Therefore, microneedles are projected to have a well-defined role in providing for painless, self-administered transdermal delivery of large molecule drugs, therapeutics, and vaccines including insulin, proteins, DNA, and inactive viruses (Kim, Park, and Prausnitz 2012; Sullivan et al. 2010). By bypassing the stratum corneum, microneedles allow for delivery of large molecule drugs and therapeutics directly into the epidermis at which point they are able to diffuse

into deeper tissues in the same manner as small molecule drugs, as has been demonstrated here with fentanyl.

Unlike small molecule drugs that can be effectively administered into the body by nearly any delivery means, large molecule drugs can only be delivered via intravenous, intramuscular, or subcutaneous injection. All of these methods for delivering large molecule drugs involve significant discomfort and pain for the patient. Because of the limited therapeutic capabilities of small molecule drugs, highly potent modern drugs typically consist of large molecules, such as nucleic acids and proteins. Therefore, there is significant value in developing hollow microneedle drug delivery platforms to enable effective and painless administration of large molecule drugs that cannot be delivered via existing topical patches.

Chapter 7

Oxygen Etching

7.1 Introduction

The CNT-polymer microneedles, as has been demonstrated, are capable of acting as a transdermal delivery system in their present configuration. Several options have been presented to increase the performance or flexibility of the platform by allowing for features such as taller microneedles, smaller tip diameters, and side-terminated lumens. In a departure from the preceding chapters that examined the microneedle-skin patch system as a whole, here, a more fundamental look is taken at how these goals can be achieved by introducing a new technique to modify the CNT scaffold before polymer incorporation.

Capillography was introduced in Chapter 3 as a natural byproduct of thermal curing of a polymer resin, causing the CNT scaffold to contract as volatile components of the resin evaporated. Capillography is dependent on the evaporation of the wicking fluid to bring neighboring CNTs into closer contact. Oxygen etching is introduced here as a more versatile option for increasing the packing density and interaction between CNTs to induce macroscopic shape change in CNT scaffolds.

CNT scaffolds are fabricated by standard catalyst patterning and chemical vapor deposition techniques. After fabrication, CNTs are exposed to a low power isotropic oxygen plasma. Oxygen plasma has two effects on CNTs: an increase in oxygenated functional groups and an increase in the structural defects. The result of both modifications cause neighboring

CNTs to come into closer contact with each other, causing a macroscopic densification of the CNT scaffold (Aria 2013). This technique allows for higher densification of CNT scaffolds than is possible with capillography, and also makes the densification process controllable as well as independent of a fluid medium. Here, oxygen etching is investigated within the scope of exploring the concept of controllable shape change of macroscopic CNT structures for the express application of hollow microneedles.

7.2 Materials & Methods

Two patterns of CNT bundles are fabricated in the same manner as described in Chapter 2. The first pattern investigated consists of hollow cylindrical pillars of similar dimension to the CNT scaffolds used thus far. Pillars have a circular cross-section, with 150 µm and 120 µm outer and lumen diameter respectively. The second pattern consists of a hollow pillar with a non-axisymmetric cross-section to investigate the effect of oxygen etching on complex cross-section geometries. Details on the geometry of the second pattern will be presented in Section 7.4. All of the samples used in this study have a height in the range of 150 to 500 µm.

To achieve the oxygen etching effect, CNT pillar samples are placed in a plasma etcher (M4L RF Gas Plasma System, PVA Tepla, Corona, CA). Plasma is produced remotely such that the plasma is isotropic in distribution when it contacts the CNT samples. This allows for the CNT pillar to be uniformly etched on all surfaces, rather than an anisotropic etching as typically seen in other plasma processes such as reactive ion etching (RIE). The RF power is set for 50W, with an oxygen flow rate of 150 sccm, and a chamber pressure of 500 mTorr. Process time is varied from 3 to 20 minutes.

As has been demonstrated in a previous study, the progression of oxygen etching on CNTs can be quantified by measuring the atomic composition of the material and calculating the oxygen to carbon ratio of the sample (Aria 2013). The atomic composition of the CNT scaffold is

measured through energy dispersive x-ray spectroscopy (EDS) (X-Max Silicon Drift Detector EDS System, Oxford Instruments, Abingdon, England). EDS measurement is integrated with SEM imaging to allow for EDS analysis on specific microneedles. In this way, the geometry and the atomic composition of a CNT pillar are measured concurrently.

7.3 Experimental Results

7.3.1 Hollow Cylindrical Pillars

Oxygen etching effectively introduces a taper geometry to hollow cylindrical CNT pillars. The base diameter of the pillar remains constant at 150 µm, while the tip diameter progressively shrinks. Figure 7.1 demonstrates the geometry that can be achieved through oxygen etching by starting with a hollow circular cylinder produced by standard catalyst patterning and CVD methods. At low oxygen plasma dosages with a measured oxygen-to-carbon ratio below 10%, the tapering effect is uniform over the height of the pillar. Above this threshold, the etching rate at the tip of the pillar decreases relative to the etching rate of the rest of the needle, causing the formation of a neck just below the microneedle tip where the outer diameter reaches a minimum value. Additionally, at high dosage levels, the base of the microneedles begins to collapse. In the final configuration of the etched pillar as seen in Figure 7.1e, formerly vertical CNTs now run horizontal across the substrate before coming together to support a pillar with a reduced base diameter of 20 µm.

Figure 7.2 plots the progression of the pillar's minimum diameter over the course of etching. From the plot, it is observed that the etching behavior can be divided into three regions. In Region I, the oxygen-to-carbon ratio, or O/C ratio, varies from 0% to 3.8%. The shape of the pillar remains unchanged during this regime as the effects of etching can only be seen on the atomic scale, as oxygenated functional groups, including carbonyl, carboxyl and epoxide groups,

begin to deposit on individual CNTs (Figure 7.1a) (Aria 2013). In Region II, a smooth taper is

developed along the length of the pillar. (Figure 7.1 b,c). Region II is characterized by an O/C
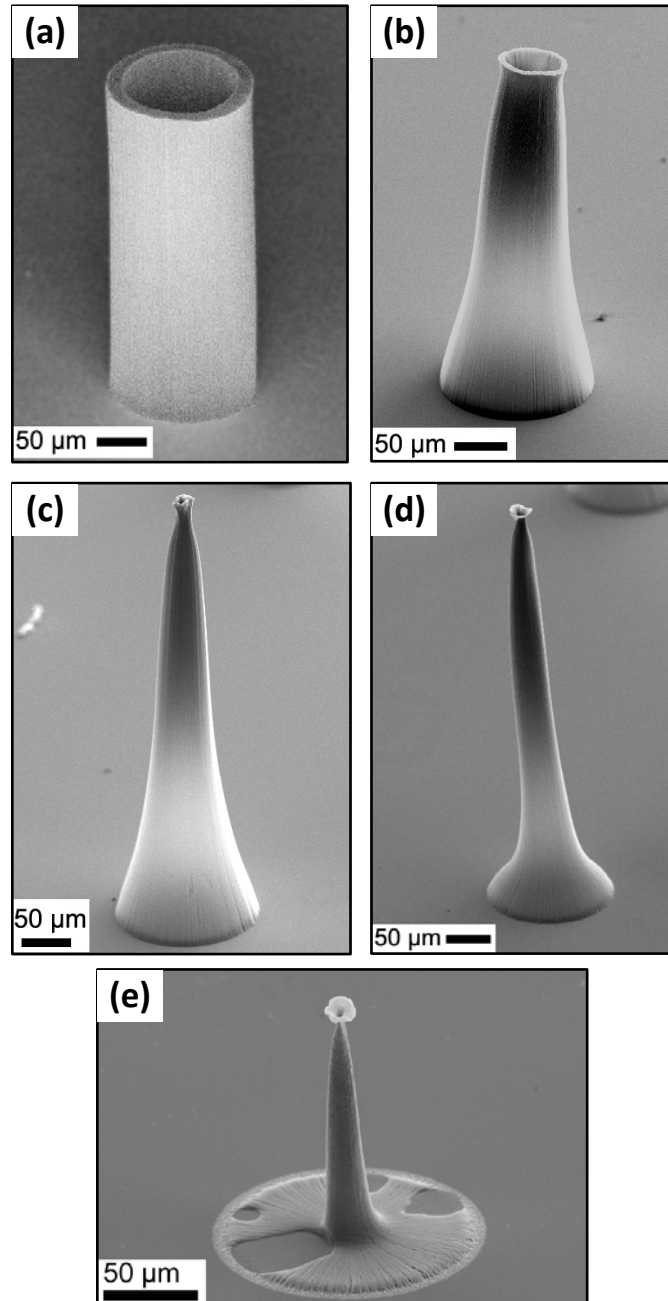

Figure 7.1- SEM images of microneedles at different stages of oxygen etching process with oxygen-carbon ratios of **(a)** 0% (Region I), **(b)** 8.49% (Region II), **(c)** 8.71% (Region II) **(d)** 18.05% (Region III) **(e)** 31% (Region III). All base diameters are 150 µm.

ratio range between 3.8% and 10.2%. The pillar is highly responsive to the plasma treatment, as the tip diameter can be reduced to 8.3% of its original size to produce a 12 µm tip.
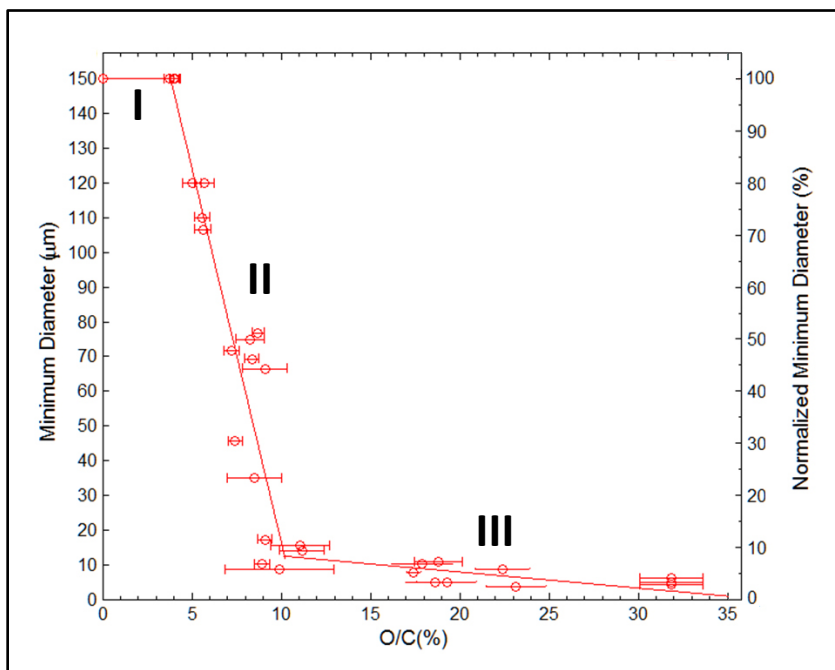
Figure 7.2- Minimum pillar diameter vs. oxygen-to-carbon ratio (O/C)

In Region III, for an O/C ratio greater than 10.2%, the etching rate with respect to the minimum diameter begins to decrease. The etching rate over the pillar becomes non-uniform as the minimum diameter point in the pillar shifts from the tip to slightly below the tip to form a neck (Figure 7.3). This necking effect is caused by non-uniformities in the distribution and quality of CNTs in the original unetched CNT pillar. A crust region of several microns thickness is typically present at the top of vertically-aligned CNT bundles (Meshot and Hart 2008). In the crust region, the alignment of the CNTs breaks down, creating a dense layer of highly entangled

CNTs. A conformal layer of amorphous carbon can also be observed in the crust region, depending on the quality of the CNT growth. The increased nanotube density combined with the presence of amorphous carbon makes the crust layer more resistant to etching than the rest of the CNT pillar at high etching doses. Thus, as can be observed in Figure 7.3, the crust layer reaches a minimum feature size while the rest of the pillar continues to contract. The neck of the pillar, therefore, represents the boundary between the crust and well-aligned CNT layers.
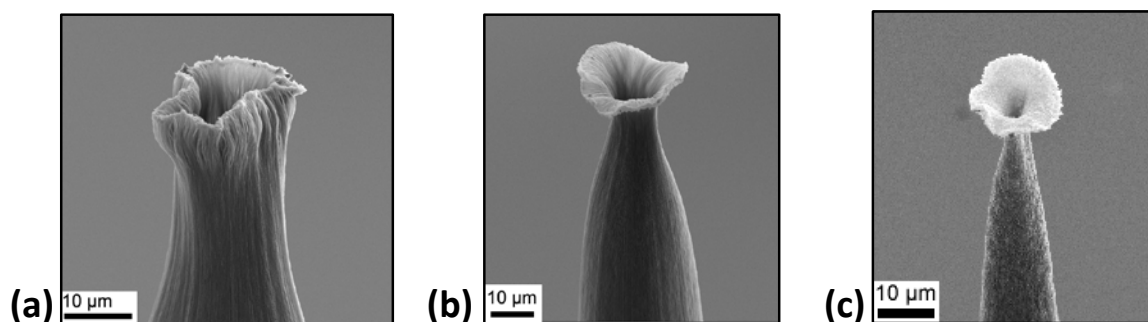
Figure 7.3- CNT pillars with tip-neck ratios of **(a)** 1, **(b)** 2.36, **(c)** 3.3.

The observed necking effect occurs consistently in Region III for pillars where the tip diameter drops below 10 µm (Figure 7.4). For the application of hollow microneedles, the formation of a neck represents a failure mode for the CNT scaffold. The neck represents a weak point in the structure that would be prone to failure during skin penetration. Above the 10 µm diameter threshold, oxygen etching can be used to reproducibly fabricate microneedle geometry to introduce a taper and produce a maximum reduction in tip diameter of 93%.

As the diameter of the pillar contracts, the thickness of the pillar also contracts (Figure 7.5). In examining the network of vertically-aligned nanotubes, the cumulative effect of oxygen etching increases the interaction between neighboring CNTs pulling the nanotubes together. (Figure 7.6) Previous results have linked this effect to the presence of oxygenated functional group facilitating nanotube interactions, as well as an increase in electrostatic interactions during

etching. For highly etched samples, it was also shown that the sp^2 structure of the CNT begins to degrade, resulting in an amorphous structure (Aria 2013). This can be observed in the CNT pillars at an O/C ratio of 32%, where the heavily damaged CNT fibers take on an almost fuzzy or shaggy appearance (Figure 7.6g). Overall, the increase in interactions between nanotubes increases the packing density of the CNT mesh, which in turn results in the macroscopic reduction in pillar thickness.
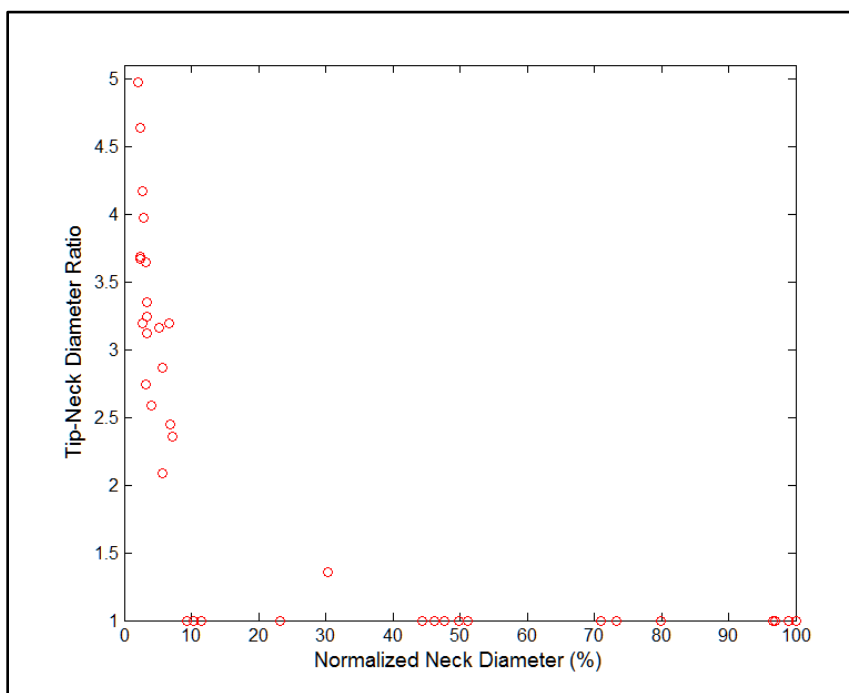
Figure 7.4- Ratio between Tip and Neck Diameter vs. Normalized Neck Diameter

The formation of the neck at the beginning of Region III induces the tip of the pillar to progress through a transformation akin to a blooming flower. Just prior to the formation of the neck, the tip loses its circular shape, which indicates the high degree of flexibility of the pillar tip (Figure 7.5c). As the diameter of the neck continues to shrink, the CNT fibers that support the tip begin to bend, causing the tip of the microneedle to expand outward, creating a flower like-bloom (Figure 7.5d). The flower bloom created at the tip remains with constant size even at higher

etching rates. However as etching continues, the difference in the texture of the nanotubes is observed as the CNTs become more rough and the pattern of vertically-aligned fibers becomes heavily distorted, indicating an amorphous state of the CNTs.
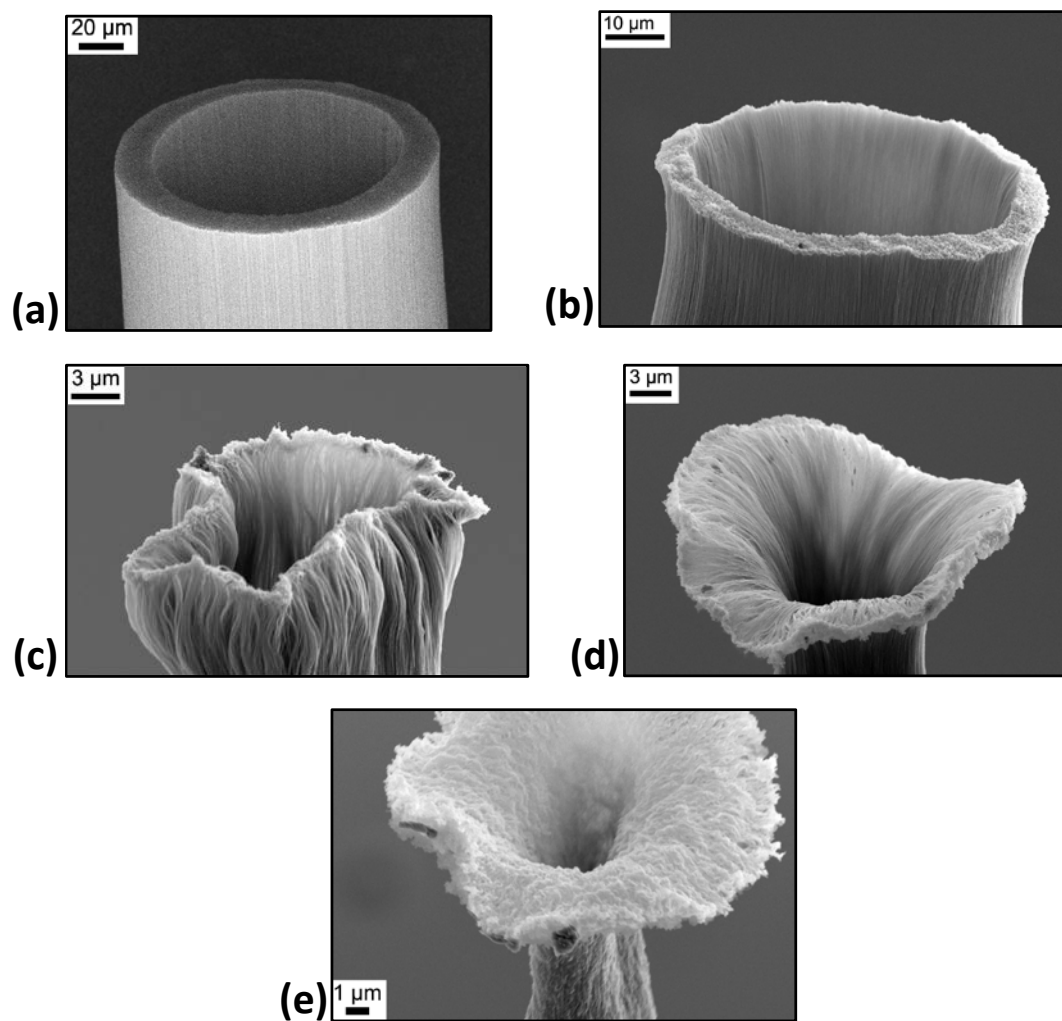
Figure 7.5- Needle tips for oxygen-carbon ratios of **(a)** 0% (Region I), **(b)** 8.49% (Region II), **(c)** 8.71% (Region II) **(d)** 18.05% (Region III) **(e)** 31% (Region III).
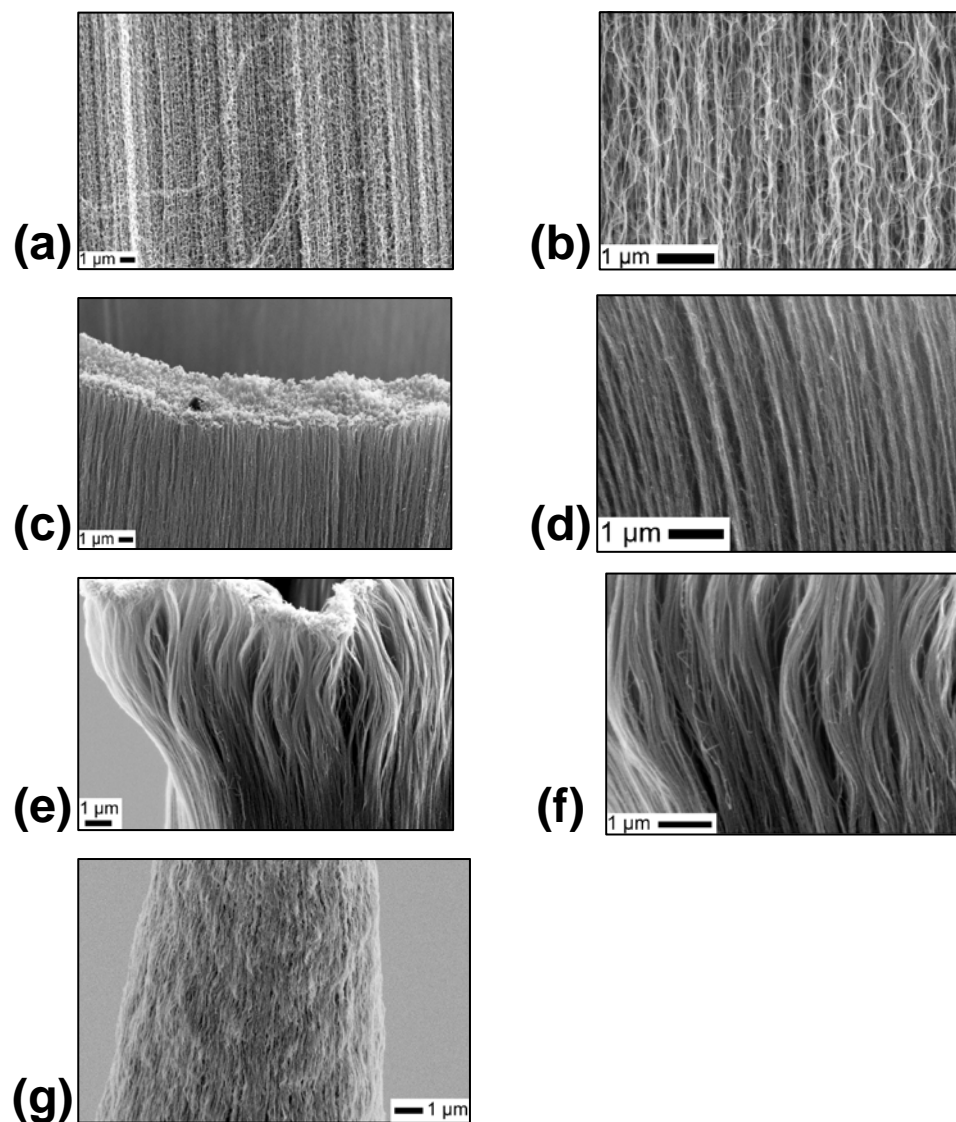
Figure 7.6- Densification of the CNT mesh for oxygen-carbon ratios of **(a), (b)** 0% (Region I), **(c), (d)** 8.49% (Region II), **(e),(f)** 8.71% (Region II) **(g)** 31% (Region III).

The reduction in thickness follows the same three regions that were used to describe reduction in minimum diameter (Figure 7.6a). The reduction of thickness is also qualitatively similar in each region to what was observed with minimum diameter. Thickness is initially constant in Region I. In Region II, the CNT network is very responsive to etching as the packing density of the network increases. In Region III, the thickness continues to decrease slightly but is

less responsive to etching as in Region II. Instead, the primary characteristic of Region III is that the CNTs become amorphous.
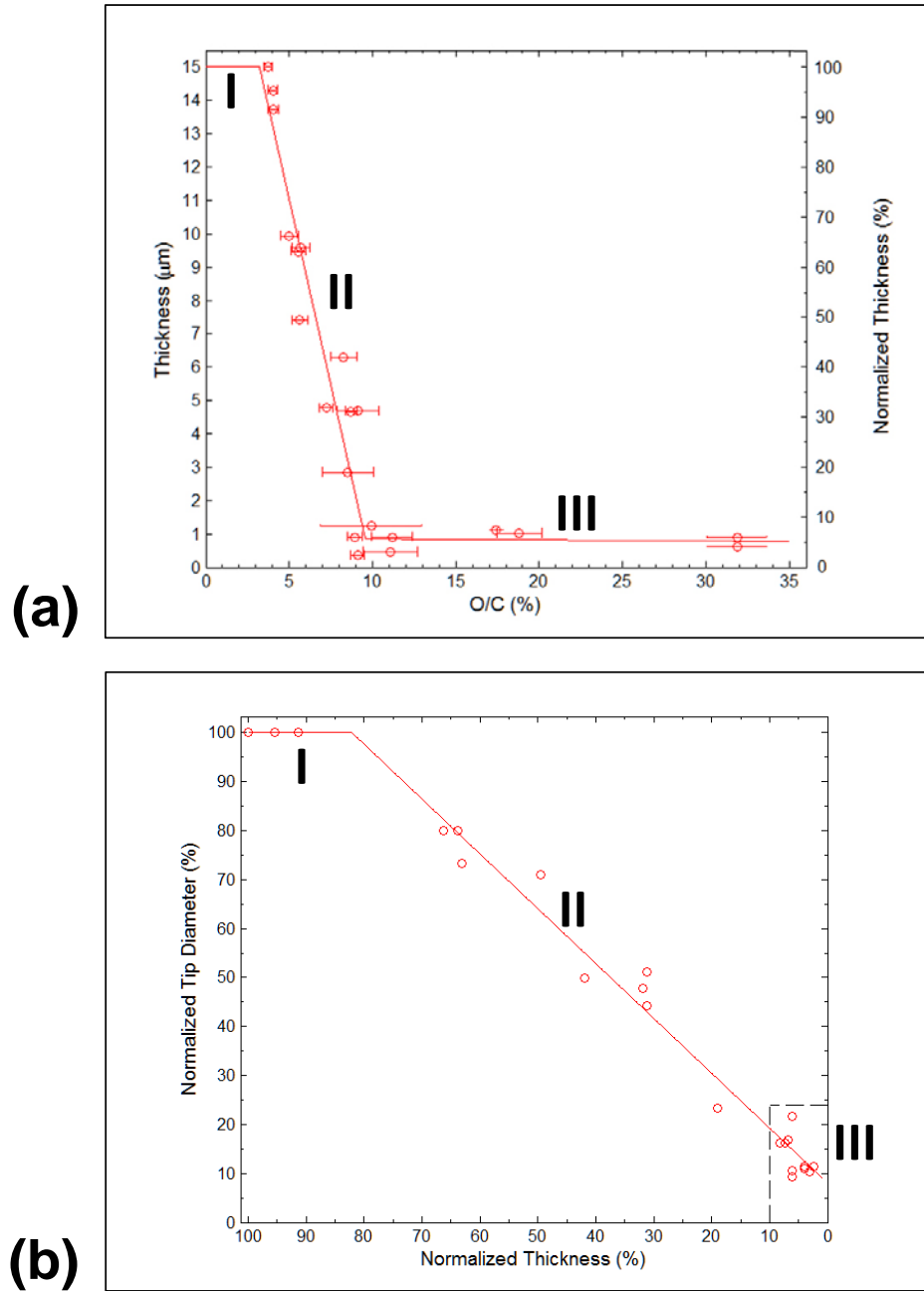
Figure 7.7- (a) Thickness vs O/C Ratio. **(b)** Normalized Thickness vs Normalized Tip Diameter.

Transition	Thickness	Diameter
Region I and II	3.23 %	3.82%
Region II and III	9.57%	10.20%

Table 7.1- Transition point in terms of O/C ratio, as determined by linear fit to data.

In comparing the region transition points for diameter and thickness as defined by the linear fit to the data, it is observed that for both the transition from Region I to II and the transition from Region II to Region III, the transition occurs in thickness before diameter (Table 7.1). This indicates that contraction in diameter follows contraction in thickness. In Figure 7.7b, the normalized tip diameter is plotted against the normalized thickness. It is estimated that the diameter remains constant until the thickness reaches 82% of its original value, or 12.3 µm. A single linear fit can be used to fit the data from Region II and Region III. This demonstrates that despite large changes in etching sensitivity between Region II and Region III, the relative etching rate between diameter and thickness remains the same throughout Regions II and III.

Oxygen etching, as presented here, represents a novel bottom-up approach to modify the shape of CNT pillars. The isotropic distribution of the plasma allows for the etching effects to be distributed throughout the pillar, rather than focused on the top surface as seen with anisotropic etching processes such as RIE. Because of this isotropic distribution coupled with the low RF power utilized, shape change is introduced not by destructive etching of CNTs, but rather by an increase in interactions between neighboring CNTs, resulting in a more compact CNT network that triggers shape change in terms of pillar thickness and ultimately pillar diameter on the macroscopic scale.

7.3.2 Application to Complex Geometry

To demonstrate the potential of this technique to induce macroscopic shape change by CNT densification, oxygen etching was applied to a shape with a complex cross-section. A vertically-aligned CNT array is patterned into a flower-shaped ring with 5 petals connected to each other by thin bridge elements (Figure 7.8a). Fabrication of the flower ring followed standard catalyst patterning and chemical vapor deposition procedures. The circular cavity has a diameter of 100 µm, and the distance from the center of the pattern to the tip of each petal is 100 µm. The bridge element has a minimum thickness of 25 µm, and the petal has an approximate diameter of 40 µm. The shape is chosen to be qualitatively similar in design to a previous study that investigated using capillography to induce shape change in complex patterns (De Volder et al. 2010).
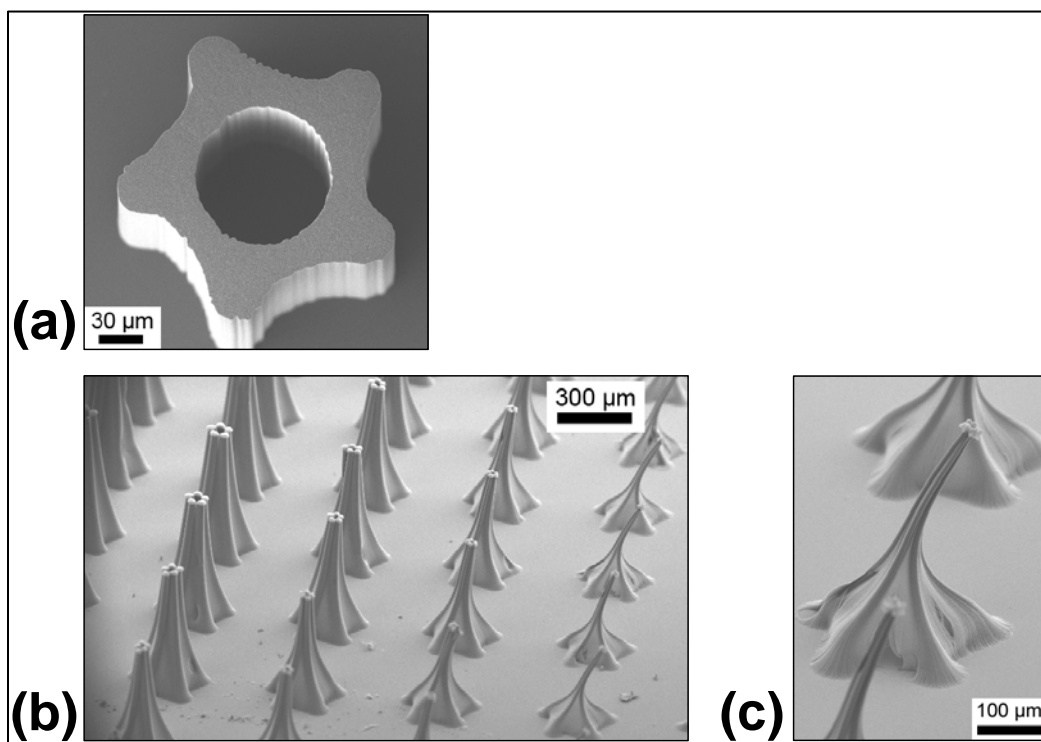

Figure 7.8- (a) Flower ring patterned vertically-aligned carbon nanotubes after CVD. **(b), (c)** After oxygen etching, petals converge in the center to create a central pillar. Etching progression increases from left to right across the sample.

Figure 7.8 b,c shows the result of oxygen etching in the flower ring geometry. The thinner bridge elements are more easily penetrated by the oxygen plasma, allowing the bridge element to compress at a faster rate than the petal element. The compression of the bridge before the petal results in the petals being brought together in the center of the geometry to form a single pillar from the intertwining petals. Figure 7.8b shows the progression of oxygen etching, moving from left to right across the sample. The original 100 µm central cavity is reduced to a central pillar with an ultimate tip diameter of 20 µm. Similar to the hollow cylindrical pillars investigated earlier, the original catalyst patterned geometry remains present at the base of the flower ring pillar. In Figure 7.8c, the CNTs that comprise the bridge element can be clearly observed near the substrate. Higher up on the geometry, as the central pillar begins to form, the bridge element can no longer be observed as the petal elements come into direct contact.

7.3.3 Comparison to Capillogrpahy

For the flower ring geometry, the same qualitative shape transformation achieved by oxygen etching is also observed using capillography as the CNT densification method (De Volder et al. 2010). However, oxygen etching, when compared to capillography, represents a much more powerful platform for inducing shape change in CNT structures. Previous work using solvent capillography on 200 µm diameter hollow cylindrical pillars, of similar thickness to the cylindrical pillars investigated here, was able to demonstrate an ultimate tip diameter reduction of 44% (De Volder et al. 2010). In contrast, oxygen etching, as presented here, was able to reduce the tip diameter of a cylindrical pillar by 92% by the end of Region II, before the occurrence of necking in Region III.

Additionally, oxygen etching offers more process control as factors such as pressure, flow rate, and RF power can be adjusted to optimize the etching process. In contrast, the capillography process is fully dependent on the capillary transport and evaporation of a volatile

fluid medium. In order to affect change into the densification process of capillography, the fluid medium must be changed, which only allows for large discrete changes in the process. Instead, tuning of the plasma parameters in oxygen etching allows for fine control of the process.

7.4 Geometric Model

7.4.1 Motivation

Here, a geometric model for oxygen etched hollow cylindrical pillars is investigated. The model uses pillars of the same dimensions as those used in Section 7.3.1. The ability of oxygen etching to introduce a taper into cylindrical pillars, as demonstrated in the experimental results, represents a major advantage in terms of the fabrication and delivery of CNT-polymer composite microneedles as described in Chapter 3 and Chapter 5 respectively. The ability to controllably fabricate a taper can improve microneedle delivery by reducing penetration force. This in turn enables fabrication of microneedles with higher aspect ratios allowing for either longer microneedles to achieve higher penetration depth or smaller diameter microneedles to increase the microneedle packing density on a drug delivery platform.

Region II represents the ideal etching range for the application of microneedles, as described previously, as the tip diameter can be reduced to 92% of its original size without the complication of neck formation as observed in Region III. The geometric model presented here aims to understand what occurs during Region II on the macroscopic scale in terms of structure geometry. The ultimate goal of the model is to develop a tool for predicting the shape of tapered microneedles fabricated through oxygen etching. In this way, the model allows for the design of a specific microneedle geometry before committing to fabrication.

CNT bundles are approximated as an array of vertically-aligned strings with constant properties throughout the length of the pillar. As a string, the CNTs can be deformed into any

curved geometry and maintain a constant length throughout the etching process. From this approximation, the model aims to predict the profile of the needle geometry for a given etching progression and examine secondary effects of etching that cannot be easily resolved through experimental observation. It is expected that the height of the microneedles decreases during etching as a result of the introduction of curvature into the needle shape. However, due to the large variance in height of the CNT microneedles, this has not been conclusively proven from experimental data.

7.4.2 Methods

The profile of the pillar is modeled as a hyperbolic cosine with the variable definitions in terms of the microneedle geometry given in Figure 7.9 (Equation 7-1). A hyperbolic cosine is typically used in models to represent the curvature of strings. Most commonly, a subset of hyperbolic cosine curves, a catenary curve, is used to model the deformation of a string under its own weight (Ng and Grimsdale 1996).

$$y = a \cosh\left(\frac{x}{b}\right)$$

7-1

The origin of the coordinate system is placed at the center of the pillar tip. The direction along the length of the microneedle is given by x. The radius of the pillar at a given height is given by y. Equation 7-1 describes the profile for the right side of the microneedle. The microneedle is axisymmetric such that the profile for the left side of the microneedle is given by reflecting the profile generated by Equation 7-1 across the x-axis.
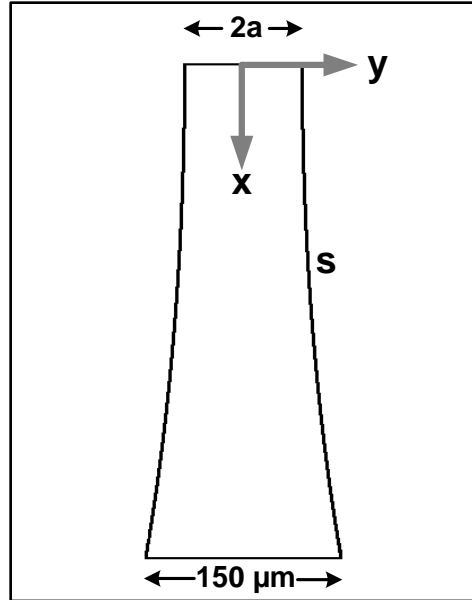
Figure 7.9- Coordinate and variable definition for geometric model.

From the experimental results of Section 7.3.1, it was observed that the base is constant throughout Region II. This constraint is present in the model such that the base diameter for all generated microneedles is constant at 150 µm.

The parameter b is set to keep the arc length, s, of the CNT string constant throughout the etching process. The consistency of the base diameter in the experimental results indicates that the primary method of shape change during oxygen etching is not the destruction of individual CNTs, but rather the densification of the CNT network causing the CNT pillar to compress. The arc length is set as the initial height of the pillar before etching. The parameter b is connected implicitly to arc length by Equation 7-2.

$$s = \int_0^{b \cosh^{-1}(75/a)} \sqrt{\left(\frac{a}{b}\sinh\left(\frac{x}{b}\right)\right)^2 + 1} \ dx \qquad \text{7-2}$$

The parameter b is solved for numerically to within an error of 0.01% in arc length.

7.4.3 Results

Figure 7.10 depicts the results of the model for the evolution of the profile of the cylindrical pillar examined in Section 7.3.1 through Region II. A cylindrical pillar of initial height 200 µm and 400 µm with a base diameter of 150 µm is depicted by the black cross section (Figure 7.10 a,b respectively). As the O/C ratio of the pillar increases, as denoted in the transition from blue to red profile, the tip diameter begins to contract. The side profile of the pillar is initially linear and then becomes more concave as etching progresses. The termination of Region II is depicted in the final pillar profile with a tip diameter of 10 µm.
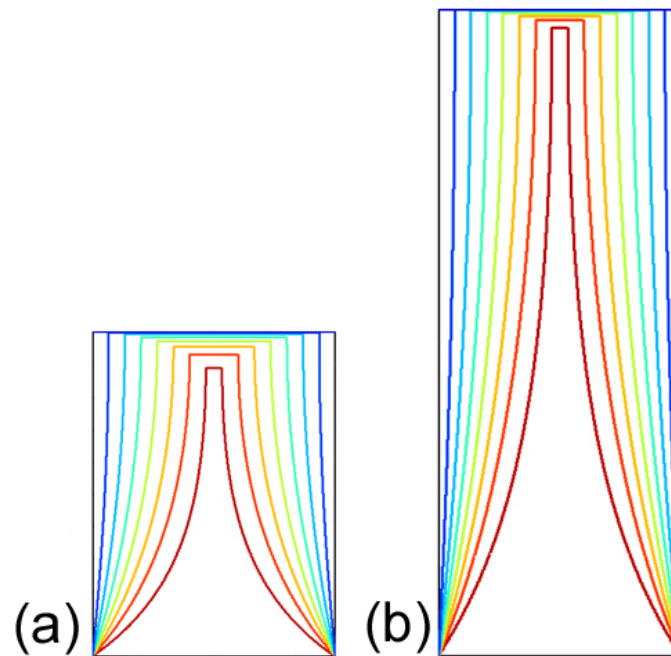
**Figure 7.10-** Profile evolution of microneedle of 150 µm diameter base and **(a)** 200 µm height **(b)** 400 µm height. Images to relative scale.

The profile predicted by the model has very good agreement with the experimental results from Region II, as exemplified in Figure 7.11a. The success of the model in Region II highlights the smoothness of the profile along the length of the pillar created by oxygen etching.

In Region III, the model no longer captures the profile of the needle, as the profile cannot be represented as a single global curve. Features such as necking at the tip and the collapse of the base seen at higher etching rates create local deviations in the shape of the pillar. These deviations prevent the profile from being defined simply from the boundary conditions of the pillar. Figure 7.11b illustrates an example of this for a pillar with a slight neck at the boundary between Region II and III. Comparing the pillar shape to the predicted curve, the model captures the overall profile of the pillar with the exception of the top 20% of the pillar. The formation of the neck changes the curvature of needle near the tip. In approaching the tip, the model predicts a more gradual compression of the pillar diameter. However, the presence of the neck causes a more rapid compression of the pillar, which is confined to the top 20% of the pillar.
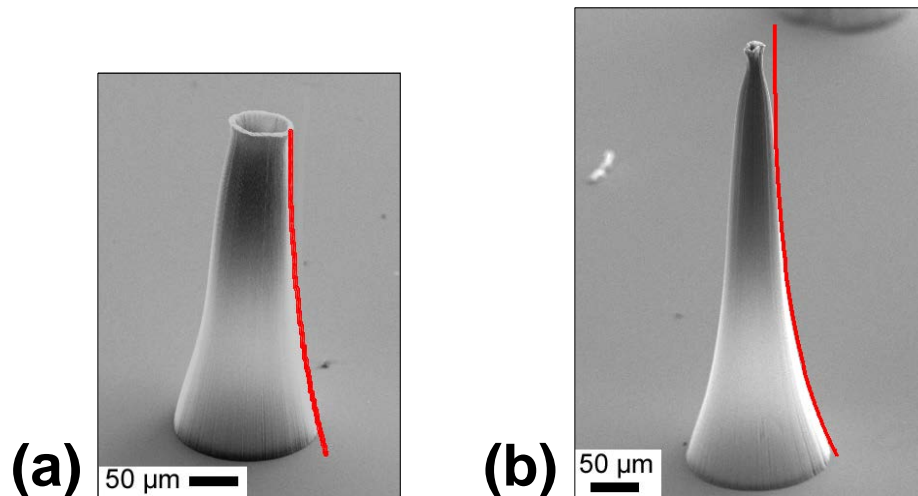
Figure 7.11- Comparison of microneedle with model predicted profile for **(a)** Region II microneedle and **(b)** microneedle at transition between Region II and III showing early stages of necking.

In addition to predicting the profile of the pillar, the constraint of the model to preserve the arc length of the CNTs allows for insight into how the height of the pillar changes during etching. This is of particular importance for the microneedle application, where the total height of the microneedle determines the penetration depth of the microneedle in the skin. Figure 7.12

shows the relation between normalized pillar height and tip diameter for initial pillar heights of 200, 300, 400, and 500 µm. The overall change in height during etching depends greatly on the initial height of the pillar. In the span of etching, where the tip diameter is decreased by up to 93% of its original size, pillars of initial height 200 µm and 500 µm have a change in height of 2% and 11% respectively. While the change in height of the CNT scaffold during etching can be neglected for shorter microneedles, change in height for taller CNT scaffolds can be significant and needs to be incorporated into the final microneedle design to ensure proper penetration depth in the skin.
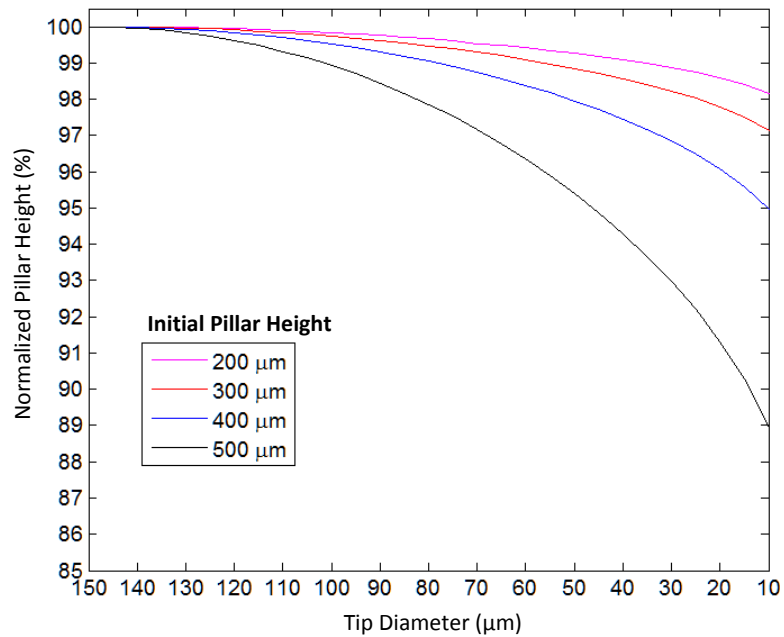
Figure 7.12- Change in pillar height during oxygen etching as a function of tip diameter.

The relation between the model parameters *a* and *b* is illustrated in Figure 7.13 for different initial pillar heights. The qualitative trend is the same for pillars of different initial heights throughout the etching process, as represented by the shrinking tip radius *a.* In the hyperbolic cosine function, *b* acts as a scaling parameter that determines the degree of curvature

in the profile. For very large *b*, the profile of the pillar is linear. As *b* decreases, the curvature of

the pillar increases.
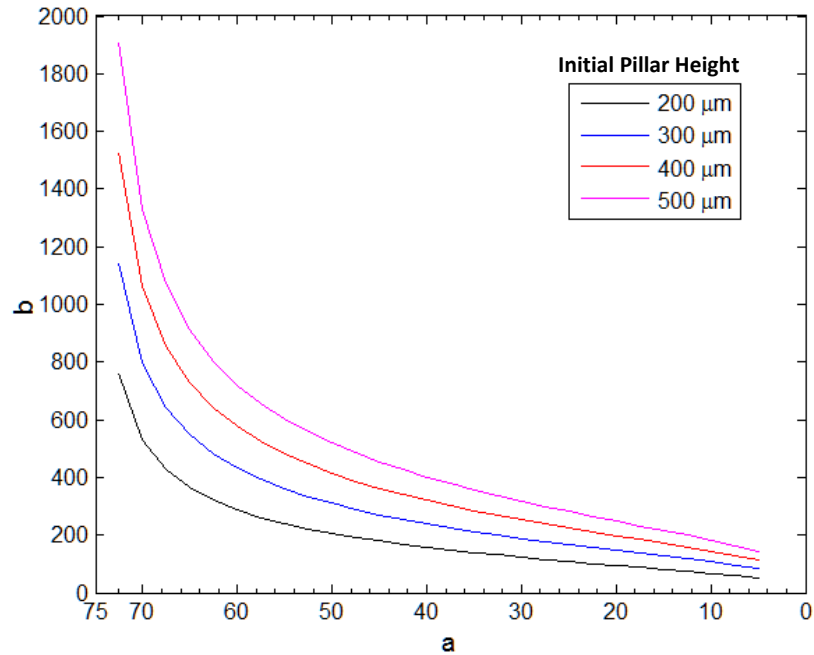
Figure 7.13- Model parameter plot for *b* vs. *a* (tip radius).

7.5 Conclusions

Bottom-up assembly, as demonstrated in the application of the CNT-polymer composite microneedles, represents a powerful fabrication technique. The direct access to the nano-scale of bottom-up assembly allows for faster, more flexible, and more scalable fabrication of micro- and nano- structures than what can be achieved by conventional top-down fabrication. For CNTs, traditional bottom-up fabrication methods, such as catalyst patterning and chemical vapor deposition, restrict CNTs to extruded geometries with constant cross-section. This restriction ultimately limits the adaptation of CNTs for microneedles and other applications.

Oxygen etching, as introduced here, is a passive, scalable method for overcoming this obstacle by enabling 3D geometry for CNT structures. Using a cylindrical pillar of the same diameter as the CNT-polymer composite microneedles, oxygen etching was shown to introduce a tapered geometry to the cylindrical pillar, reducing the tip diameter by 93%. Further etching beyond this point is possible, resulting in a blossoming-type transformation of the pillar tip that illustrates the potential of unique shape transformations that can be achieved by oxygen etching. However, for the express application of microneedles, the creation of a minimum diameter neck during the blossoming transformation makes the geometry ill-suited for use as a microneedle scaffold.

A geometric model was introduced for the cylindrical pillar to illustrate the shape transformation during the second phase of oxygen etching (Region II). The profile of the etched pillar can be represented as a single, smooth curve derived from a hyperbolic cosine function. From the model, it was observed that oxygen etching reduces the height of the cylindrical pillar. The magnitude of the height reduction is dependent on the initial height of the pillar. Short pillars are only marginally affected with a 2% maximum height reduction for an initially 200 µm tall pillar. In contrast, taller pillars are susceptible to larger height reductions with an 11% maximum reduction for an initial pillar height of 500 µm.

Oxygen etching in itself operates as a bottom-up method, inducing densification in the mesh of vertically-aligned CNTs. This densification then triggers macroscopic shape change, as observed in the cylindrical pillar by a reduction in pillar thickness followed by reduction in tip diameter. In CNT scaffolds with more complex geometry, oxygen etching can be used to generate unique shape transformation beyond the capabilities of standard top-down fabrication approaches. Here, a flower pattern with a hollow cavity was used to demonstrate how the CNT mesh is compressed at a faster rate in thinner features than thicker features to cause macroscopic shape change, as the flower collapses into a central hollow pillar via oxygen etching.

Oxygen etching represents a significant step towards creating scalable fully three-dimensional CNT structures. For microneedles, this technique has the immediate application for introducing tapered geometry and increasing the aspect ratio of microneedles, allowing for more compact microneedle arrays and taller microneedles. The interplay of features with different thicknesses, as illustrated in the flower ring example, may allow for fabrication of a much wider range of geometries that would be of interest in the future development of the CNT-polymer composite microneedle concept. In one potential application, by patterning an off-center lumen to create a microneedle geometry with variable thickness, oxygen etching may initiate a side-terminated lumen, akin to a hypodermic needle, on the thin side of the needle, while keeping the geometry of the thick side of the needle unchanged. In future work to incorporate oxygen etched geometry into the CNT-polymer composite framework, attention must be placed on the effect of CNT densification on the transport of polymer resin through the CNT scaffold.

Chapter 8

Conclusion

8.1 Summary

8.1.1 Impact of the Study

Carbon nanotubes represent a multi-functional material with a unique set of structural, electrical, thermal, and fluidic properties that make them attractive for use in an extensive field of micro- and nano- devices. However, their widespread use to date has been restricted to CNT powders, random alignment of CNTs without attachment to a common substrate, due to a lack of methodology to shape and transport nanotubes after their fabrication. Here, in the context of hollow microneedles, new fabrication techniques were demonstrated to increase the utility of patterned vertically-aligned carbon nanotubes. Hollow microneedles represent an ideal technology for evaluating the efficacy of incorporating CNTs into a complex mechanical system. Current hollow microneedle designs rely on top-down approaches due to their heritage as a spinoff technology from microelectronics based microfabrication. However, the technical difficulty of creating high aspect ratio features and efficiently defining the lumen in top-down approaches has added considerable fabrication complexity that has suppressed further development of the technology.

Developing a more streamlined fabrication process for hollow microneedles through a CNT architecture can have a profound impact on drug delivery and healthcare in general. Microneedle skin patch designs such as the dual reservoir skin patch with CNT-BODPA

polyimide microneedles allow for painless, self-administered drug delivery. Enabling patients to self-administer drugs normally reserved for hypodermic injection decreases the overall demand for medical personnel and facilities. This is especially important for many countries where access to medical infrastructure is limited. The enhanced immunogenic response of the skin to vaccination, compared to deeper tissues where vaccines are typically injected, not only makes microneedle administered vaccines more effective in inoculating a patient but also reduces dose size, allowing for increased worldwide supply of vaccines.

8.1.2 Microneedle Fabrication

The fabrication methods presented in this thesis are aimed to fill the engineering gap between vertically-aligned carbon nanotubes, fabricated by catalyst patterning and chemical vapor deposition techniques, to fully functional microneedles. The nanoporosity of CNT structures was found to be key to creating CNT-polymer composites that conform to the shape of the original patterned CNT structure. Through spin coating, polymer resins simultaneously create a composite with CNTs and form a common polymer base to allow for the microneedles to be transferred onto delivery platforms. Two fabrication approaches were demonstrated: a thermal curing technique for thermoset polymers and CNT Masked Photolithography, which uses CNTs as a photomask for selectively curing negative photoresists. These methods were demonstrated for a few representative polymers: BOPDA-polyimide for thermal curing and SU8-2025 & HD-4110 polyimide for selective UV curing. These fabrication approaches both focus on simple, passive fabrication steps such that the fabrication can potentially be scaled up to commercial production. In particular, the thermal curing technique relies solely on the fluid mechanics of the polymer resin to ensure the lumen remains unobstructed.

In order to make the fabrication technique more universally accessible, a set of requirements was developed to screen the compatibility of arbitrary thermoset polymers and

negative photoresists with the presented fabrication process. Transport of polymer resin through the lumen and into the nanoporous network of CNTs was analyzed by the Washburn model of capillary action. From this analysis, it was determined that the intrinsic material properties of a polymer resin alone could determine the resin's compatibility with the thermal curing process. A characteristic wicking velocity in the Washburn model, defined as the ratio of surface tension to viscosity, is used to qualitatively describe the ease in which the polymer is wicked through the nanoporous matrix. Polymer resins with a wicking velocity greater than 1 cm/s were found to be generally compatible with the thermal curing technique.

CNT-polymer microneedles were fabricated with needles heights in the range of 200 – 250 µm in order to penetrate into the epidermis layer of the skin. Microneedles were cylindrical in shape, with typical outer diameter between 100-150 µm and typical lumen diameter between 25-50 µm. Despite the seemingly blunt tip of the microneedles, microneedles attached to hand actuated silicone skin patches demonstrated positive *in vitro* delivery of aqueous dye in swine skin and *in vivo* delivery of fentanyl in rabbits without sustaining any structural damage. However, in order to fabricate taller microneedles to penetrate deeper into the skin, a taper geometry is needed to both reduce the force needed for skin penetration and increase the resistance of the needle to fracture failure.

Isotropic oxygen etching is introduced as a new fabrication method to introduce a taper to CNT microneedle geometry. Standard CNT fabrication practices only allow for construction of CNT structures with constant cross-section, since the geometry of the CNT structure is defined by catalyst patterning on a planar substrate. Prior to incorporating polymer, oxygen etching acts to densify the nanoporous network of nanotubes to induce macroscopic shape change in the CNT structure. In the case of a thin-shelled hollow cylinder, the size of the cylinder tip shrinks axisymmetrically, while the base of the cylinder remains fixed via attachment to the substrate to create a tapered needle geometry. Oxygen etching allows for the tip diameter to be controllably

reduced by up to 93% of its original size. Beyond this point, non-uniformities in the CNT structure cause the etching rate to accelerate just below the microneedle tip to create a neck with a diameter smaller than the tip. The existence of the neck makes the geometry inapplicable to microneedles, as the neck represents a weakened point in the structure.

A model to predict the geometry of oxygen etched pillars was developed. CNTs were modeled as deformable strings of constant length. As the tip diameter of the pillar is reduced, the CNTs begin to bend near the base of the pillar, causing the height of the microneedle to shrink by a maximum of 11%. The model is envisioned to allow for mechanical analysis of potential microneedle designs before committing to catalyst patterning and CNT fabrication. A CNT structure patterned into a flower with a central cavity is used to demonstrate the full potential of oxygen etching to create three-dimensional CNT geometry beyond the range of top-down fabrication. The presence of thick petal structures connected by thin bridge elements results in an accelerated etching rate on the thin bridge elements, causing the petals to spiral into the center of the ring to form a common pillar. While these oxygen etched designs were not incorporated into microneedles during this study, the microneedle fabrication methods presented in this study are all applicable to CNT structures created through oxygen etching.

8.1.3 Microneedle Delivery

The unique thin, flexible polymer base of the CNT-polymer microneedles allows for easy incorporation of the microneedles onto a number of drug delivery platforms. In particular, a dual reservoir silicone skin patch was developed for use with the CNT-polymer microneedles. Silicone is chosen such that the flexibility of the silicone complements the flexibility of the polymer base allowing for better contact with the skin. The dual reservoir skin patch is designed for manual operation. A single finger presses the microneedles into the skin, and a second finger actuates drug flow from a drug reservoir positioned offset from the microneedles. Development of the

dual reservoir was performed in parallel with the development of the CNT-polymer microneedles. Hand actuation is seen as an advantageous platform for microneedle delivery by eliminating pumps and the need for electricity to operate the delivery platform. This allows the hand actuated skin patch to be made more cost-effectively and allows for wider distribution.

Delivery experiments using the dual reservoir skin patch along with several variant platforms revealed deliverable drug volumes into *in vitro* swine skin and hydrogel (4%) of 4 µL and 12 µL respectively within a delivery window of 5 minutes. Upon comparing the delivery volumes with contemporary microneedles of similar lumen size and height, the CNT-polymer microneedles were found to have a delivery rate consistent, with if not higher than, comparable microneedle designs. Delivery results revealed that the primary source of hydraulic resistance for the delivery system is not the microneedles, but rather the delivery medium.

To demonstrate the utility of the CNT-microneedles in the context of drug delivery, an *in vivo* delivery study of fentanyl was performed in New Zealand White Rabbits. CNT-polymer microneedle delivery was found to be qualitatively painless compared to hypodermic injection, which was not tolerated by the rabbits. Microneedles were found to have the same approximate onset of action in the range of 1-2 hours as a topical patch. Onset of action was determined by first detection of fentanyl in the blood plasma. Performance of the CNT-polymer microneedle was found to be comparable to other microneedles of the same height. Comparison to similar microneedles confirmed an expected systemic onset of action in the range of hours. Deliverable volume was found to be consistent with what was reported for the CNT-BOPDA microneedles in the *in vitro* delivery study.

The combined results of the physical delivery study and the fentanyl study demonstrate that the delivery performance of the CNT-polymer microneedle is akin to other microneedle architectures of similar height. The results reveal that microneedles penetrating near the boundary

of the epidermis and dermis act as a hybrid between a topical patch and hypodermic needle. The microneedles are shaped like hypodermic needles and have the same short application time. However, the pharmacokinetics of drug absorption is more akin to the skin patch, as diffusion remains the primary transport mechanism for the drug to reach capillary networks in the upper dermis or denser blood vessel networks in deeper tissue layers.

8.2 Future Work

Given the fabrication advantages of the CNT-microneedles coupled with successful *in vitro* and *in vivo* delivery studies demonstrating the CNT-microneedle as having the same delivery performance of concurrent microneedle designs, this study has demonstrated that the CNT-polymer composite microneedle concept is viable for further technological development. The body of work presented here, representing a combination of fabrication methods and analysis as well as delivery results from both a physical and medicinal perspective, has been designed with the intent of creating a foundation for further work into the fabrication and application of CNT-polymer composite microneedles. It is also the author's intent that the fabrication methods presented herein can also be applied to CNT structures outside the application of microneedles in order to enable further engineering applications of CNTs beyond the current limits of CNT powders.

Throughout this study, several opportunities were presented that have the potential to augment the delivery results reported here. From analysis of the stiffness of the CNT-BOPDA composite, it was shown that the stiffness of the composite needle depends primarily on the polymer. Exploration of other CNT-polymer combinations such as polyamides-imides can allow for stiffer composite, which would enable higher aspect ratio microneedles leading either to deeper penetration by increasing the height or increased microneedle packing density by

decreasing the needle diameter. Tri-component composites using a polymer resin and nanoparticles may also lead to enhanced material properties.

Oxygen etching represents a potential revolution for shaping carbon nanotube structures. For the immediate application of hollow microneedles, the effect of densification of the nanotubes may reduce the transport rate of polymer resin through the CNT network but is not expected to significantly impact microneedle design. Being able to model and generalize the shape morphing behavior of the flower ring would allow for a new class of 3D nano-scale geometries beyond the capabilities of top-down fabrication. Combining the oxygen etching process with a vacuum annealing process to remove oxygen content from the CNTs may result in a partial reversal of the shape change observed during oxygen etching or may allow for a secondary mechanism to passively shape CNT structures.

From a functional standpoint in the microneedle design, the incorporation of a side terminated lumen may allow for reduced hydraulic resistance during delivery. This can be achieved by depositing catalyst in two stages in order to create a defect region in the microneedle structure that would result in shorter CNT growth on a single side, as presented in Chapter 5. Alternatively, a side terminated lumen can potentially be produced by oxygen etching by off-setting the lumen in the CNT scaffold to vary the thickness of the scaffold.

An exciting aspect to this work is its compatibility with continuing advances in the fields of both CNT fabrication and microneedles. The fundamental concepts and techniques for chemical vapor deposition are consistently being refined with the rise of research in graphene, which requires a much stricter CVD process than CNTs to produce quality samples. Refinements in CVD can lead to innovations leading to taller microneedles greater than 1mm in length and making the process more compatible with industrial-scale manufacturing. Given the small size of the CNT-polymer microneedles, including the macroscopically thin polymer base, the

microneedles can be easily ported to new delivery platform designs. The similarity in delivery performance of the CNT-polymer microneedles to other microneedles demonstrates that new delivery strategies, such as impact penetration and partial microneedle retraction, that have been successfully validated in other microneedle designs can be readily applied to the CNT-polymer microneedles.

Bibliography

Ali, Wahied G, and Gihan Nagib. 2011. "Embedded control design for insulin pump." *Advanced Materials Research* no. 201:2399-2404.

Amama, Placidus B, Cary L Pint, Seung Min Kim, Laura McJilton, Kurt G Eyink, Eric A Stach, Robert H Hauge, and Benji Maruyama. 2010. "Influence of alumina type on the evolution and activity of alumina-supported Fe catalysts in single-walled carbon nanotube carpet growth." *ACS nano* no. 4 (2):895-904.

Aria, Adrianus I., and Morteza Gharib. 2011. "Reversible Tuning of the Wettability of Carbon Nanotube Arrays: The Effect of Ultraviolet/Ozone and Vacuum Pyrolysis Treatments." *Langmuir* no. 27 (14):9005-9011.

Aria, Adrianus I.. 2013. *Control of Wettability of Carbon Nanotube Arrayby Reversible Dry Oxidation for Superhydrophobic Coating and Supercapacitor Applications*, Graduate Aerospace Laboratories, California Institute of Technology, Pasadena, CA.

Aria, Adrianus Indrat, Bradley Lyon, and Morteza Gharib. 2013. Sharp Tip Carbon Nanotube Microneedle Devices and their Fabrication. US Patent Publication US 2013/0178722: California Institute of Technology.

Baron, N, Jacky Passave, Blandine Guichardaz, and Gonzalo Cabodevila. 2008. "Investigations of development process of high hollow beveled microneedles using a combination of ICP RIE and dicing saw." *Microsystem Technologies* no. 14 (9-11):1475-1480.

Battelle Memorial Institute. *Press Release: Battelle's Anti-Icing System Advances in Research Program* 2011. Available from http://www.battelle.org/media/press-releases/battelle's-anti-icing-system-advances-in-research-program.

Bedewy, Mostafa, Eric R Meshot, Haicheng Guo, Eric A Verploegen, Wei Lu, and A John Hart. 2009. "Collective mechanism for the evolution and self-termination of vertically aligned carbon nanotube growth." *The Journal of Physical Chemistry C* no. 113 (48):20576-20582.

Birchall, James C. 2006. "Microneedle array technology: the time is right but is the science ready?" *Expert Rev. Med. Devices* no. 3(1): 1-4.

Burton, Scott A, Chin-Yee Ng, Ryan Simmers, Craig Moeckly, David Brandwein, Tom Gilbert, Nathan Johnson, Ken Brown, Tesha Alston, and Gayatri Prochnow. 2011. "Rapid intradermal delivery of liquid formulations using a hollow microstructured array." *Pharmaceutical research* no. 28 (1):31-40.

Chin, Curtis. 2009. "Biotechnology for global health: Solutions for the developing world." *Consilience: The Journal of Sustainable Development* no. 1 (1):19-30.

Ci, L., J. Suhr, V. Pushparaj, X. Zhang, and P. M. Ajayan. 2008. "Continuous Carbon Nanotube Reinforced Composites." *Nano Lett* no. 8 (9):2762-2766.

Cormier, Michel, Bonny Johnson, Mahmoud Ameri, Kofi Nyam, Luz Libiran, Dee Dee Zhang, and Pete Daddona. 2004. "Transdermal delivery of desmopressin using a coated microneedle array patch system." *Journal of Controlled Release* no. 97 (3):503-511.

Davis, S. P., W. Martanto, M. G. Allen, and M. R. Prausnitz. 2005. "Hollow metal microneedles for insulin delivery to diabetic rats." *Biomedical Engineering, IEEE Transactions on* no. 52 (5):909-915.

Davis, Shawn P, Benjamin J Landis, Zachary H Adams, Mark G Allen, and Mark R Prausnitz. 2004. "Insertion of microneedles into skin: measurement and prediction of insertion force and needle fracture force." *Journal of biomechanics* no. 37 (8):1155-1163.

de Villoria, R Guzmán, SL Figueredo, AJ Hart, SA Steiner Iii, AH Slocum, and BL Wardle. 2009. "High-yield growth of vertically aligned carbon nanotubes on a continuously moving substrate." *Nanotechnology* no. 20 (40):405611.

De Volder, M., S. H. Tawfick, S. J. Park, D. Copic, Z. Zhao, W. Lu, and A. J. Hart. 2010. "Diverse 3D microarchitectures made by capillary forming of carbon nanotubes." *Adv Mater* no. 22 (39):4384-9.

De Volder, Michael FL, Sameh H Tawfick, Ray H Baughman, and A John Hart. 2013. "Carbon nanotubes: present and future commercial applications." *Science* no. 339 (6119):535-539.

Doddaballapur, Satish. 2009. "Microneedling with dermaroller." *Journal of cutaneous and aesthetic surgery* no. 2 (2):110.

Foley, Patricia L, Andrea L Henderson, Eric A Bissonette, Gina R Wimer, and Sanford H Feldman. 2001. "Evaluation of fentanyl transdermal patches in rabbits: blood concentrations and physiologic response." *Comparative medicine* no. 51 (3):239-244.

Fukushima, Keizo, Ayaka Ise, Hiromi Morita, Ryo Hasegawa, Yukako Ito, Nobuyuki Sugioka, and Kanji Takada. 2011. "Two-layered dissolving microneedles for percutaneous delivery of peptide/protein drugs in rats." *Pharmaceutical research* no. 28 (1):7-21.

Gardeniers, H. J. G. E., R. Luttge, E. J. W. Berenschot, M. J. De Boer, S. Y. Yeshurun, M. Hefetz, R. van't Oever, and A. van den Berg. 2003. "Silicon micromachined hollow microneedles for transdermal liquid transport." *Microelectromechanical Systems, Journal of* no. 12 (6):855-862.

Gharib, M., E.B. Sansom, and A.I. Aria. 2010. Drug delivery and substance transfer facilitated by nano-enhanced device having aligned carbon nanotubes protruding from device surface. US Patent Publication 2012/657,862: California Institute of Technology.

Gill, Harvinder S, Donald D Denson, Brett A Burris, and Mark R Prausnitz. 2008. "Effect of microneedle design on pain in human subjects." *Clinical journal of pain* no. 24 (7):585-594.

Häfeli, Urs O, Amir Mokhtari, Dorian Liepmann, and Boris Stoeber. 2009. "In vivo evaluation of a microneedle-based miniature syringe for intradermal drug delivery." *Biomed Microdevices* no. 11 (5):943-950.

Haq, MI, E Smith, DN John, M Kalavala, C Edwards, A Anstey, A Morrissey, and JC Birchall. 2009. "Clinical administration of microneedles: skin puncture, pain and sensation." *Biomed Microdevices* no. 11 (1):35-47.

Hasegawa, Kei, and Suguru Noda. 2011. "Millimeter-tall single-walled carbon nanotubes rapidly grown with and without water." *ACS nano* no. 5 (2):975-984.

Health and Safety Executive, United Kingdom. *Structure and Functions of the Skin* 2014. Available from http://www.hse.gov.uk/skin/.

Hegde, Nagendra R, Srinivas V Kaveri, and Jagadeesh Bayry. 2011. "Recent advances in the administration of vaccines for infectious diseases: microneedles as painless delivery devices for mass vaccination." *Drug discovery today* no. 16 (23):1061-1068.

Hess, R, G. Stiebler, and A Herz. 1972. "Pharmacokinetics of fentanyl in man and the rabbit." *European journal of clinical pharmacology* no. 4 (3):137-141.

Huang, Xiao, Jijie J. Zhou, Elijah Sansom, Morteza Gharib, and Sow Chorng Haur. 2007. "Inherent-opening-controlled pattern formation in carbon nanotube arrays." *Nanotechnology* no. 18 (30):305301.

Huang, Zhipeng, Hui Fang, and Jing Zhu. 2007. "Fabrication of silicon nanowire arrays with controlled diameter, length, and density." *Adv Mater* no. 19 (5):744-748.

Iijima, Sumio. 1991. "Helical microtubules of graphitic carbon." *Nature* no. 354 (6348):56-58.

Jiang, Xiaowen, Yuezhen Bin, and Masaru Matsuo. 2005. "Electrical and mechanical properties of polyimide–carbon nanotubes composites fabricated by in situ polymerization." *Polymer* no. 46 (18):7418-7424.

Joos, P, P Van Remoortere, and M Bracke. 1990. "The kinetics of wetting in a capillary." *Journal of colloid and interface science* no. 136 (1):189-197.

Jung, Yung Joon, Swastik Kar, Saikat Talapatra, Caterina Soldano, Gunaranjan Viswanathan, Xuesong Li, Zhaoling Yao, Fung Suong Ou, Aditya Avadhanula, Robert Vajtai, Seamus Curran, Omkaram Nalamasu, and Pulickel M. Ajayan. 2006. "Aligned Carbon

Nanotube−Polymer Hybrid Architectures for Diverse Flexible Electronic Applications." *Nano Lett* no. 6 (3):413-418.

Kenney, Richard T, Sarah A Frech, Larry R Muenz, Christina P Villar, and Gregory M Glenn. 2004. "Dose sparing with intradermal injection of influenza vaccine." *New England Journal of Medicine* no. 351 (22):2295-2301.

Kim, Yeu-Chun, Jung-Hwan Park, and Mark R. Prausnitz. 2012. "Microneedles for drug and vaccine delivery." *Advanced Drug Delivery Reviews* no. 64 (14):1547-1568.

Kim, Yeu-Chun, and Mark R Prausnitz. 2011. "Enabling skin vaccination using new delivery technologies." *Drug delivery and translational research* no. 1 (1):7-12.

Kirby, Brian. 2010. *Micro-and nanoscale fluid mechanics: transport in microfluidic devices*: Cambridge University Press.

Krasheninnikov, AV, and F Banhart. 2007. "Engineering of nanostructured carbon materials with electron or ion beams." *Nature materials* no. 6 (10):723-733.

La Montagne, John R, and Anthony S Fauci. 2004. "Intradermal influenza vaccination—can less be more?" *New England Journal of Medicine* no. 351 (22):2330-2332.

Lee, Jeong Woo, Seong-O Choi, Eric I Felner, and Mark R Prausnitz. 2011. "Dissolving microneedle patch for transdermal delivery of human growth hormone." *Small* no. 7 (4):531-539.

Lyon, Bradley, Adrianus I. Aria, and Morteza Gharib. 2013(a). "Feasibility Study of Carbon Nanotube Microneedles for Rapid Transdermal Drug Delivery." *MRS Proceedings* no. 1569.

Lyon, Bradley, Adrianus I. Aria, Masoud Beizai, and Morteza Gharib. 2013(b). Polymer Composite Carbon Nanotube Microneedle Devices and Their Fabrication. US Patent Publication 2014/231,267: California Institute of Technology.

Lyon, Bradley, Adrianus I. Aria, and Morteza Gharib. 2013(c). Dual Reservoir Skin Patch for Transdermal Microneedle Drug Delivery. Provisional Patent Disclosure CIT-6672-P: California Institute of Technology.

Ma, Bin, Sheng Liu, Zhiyin Gan, Guojun Liu, Xinxia Cai, Honghai Zhang, and Zhigang Yang. 2006. "A PZT insulin pump integrated with a silicon microneedle array for transdermal drug delivery." *Microfluidics and Nanofluidics* no. 2 (5):417-423.

Marro, Diego, Richard H Guy, and M Begoña Delgado-Charro. 2001. "Characterization of the iontophoretic permselectivity properties of human and pig skin." *Journal of Controlled Release* no. 70 (1):213-217.

Marzin, J-Y, J-M Gérard, A Izrael, D Barrier, and G Bastard. 1994. "Photoluminescence of single InAs quantum dots obtained by self-organized growth on GaAs." *Physical Review Letters* no. 73 (5):716.

Mather, LE. 1983. "Clinical pharmacokinetics of fentanyl and its newer derivatives." *Clinical pharmacokinetics* no. 8 (5):422-446.

McAllister, Devin V, Ping M Wang, Shawn P Davis, Jung-Hwan Park, Paul J Canatella, Mark G Allen, and Mark R Prausnitz. 2003. "Microfabricated needles for transdermal delivery of macromolecules and nanoparticles: fabrication methods and transport studies." *Proceedings of the National Academy of Sciences* no. 100 (24):13755-13760.

Meshot, Eric R, and A John Hart. 2008. "Abrupt self-termination of vertically aligned carbon nanotube growth." *Applied Physics Letters* no. 92 (11):113107.

Microchem. *SU-8 2000 Permanent Epoxy Negative Photoresist Processing Guidelines*. Newton, MA.

Middleman, Stanley. 1995. *Modeling Axisymmetric Flows: Dyanmics of Films, Jets, and Drops*. San Diego, CA: Academic Press.

Milne, WI, KBK Teo, GAJ Amaratunga, P Legagneux, L Gangloff, J-P Schnell, V Semet, V Thien Binh, and O Groening. 2004. "Carbon nanotubes as field emission sources." *Journal of Materials Chemistry* no. 14 (6):933-943.

Mizuno, K., J. Ishii, H. Kishida, Y. Hayamizu, S. Yasuda, D. N. Futaba, M. Yumura, and K. Hata. 2009. "A black body absorber from vertically aligned single-walled carbon nanotubes." *Proc Natl Acad Sci U S A* no. 106 (15):6044-7.

NASA. 1995. Man-Systems Integration Standards. In *NASA-STD-3000*.

Ng, Hing N, and Richard L Grimsdale. 1996. "Computer graphics techniques for modeling cloth." *Computer Graphics and Applications, IEEE* no. 16 (5):28-41.

Norman, J. J., S. O. Choi, N. T. Tong, A. R. Aiyar, S. R. Patel, M. R. Prausnitz, and M. G. Allen. 2013. "Hollow microneedles for intradermal injection fabricated by sacrificial micromolding and selective electrodeposition." *Biomed Microdevices* no. 15 (2):203-10.

Novoselov, KS, VI Fal, L Colombo, PR Gellert, MG Schwab, and K Kim. 2012. "A roadmap for graphene." *Nature* no. 490 (7419):192-200.

Ochoa, Manuel, Charilaos Mousoulis, and Babak Ziaie. 2012. "Polymeric microdevices for transdermal and subcutaneous drug delivery." *Advanced Drug Delivery Reviews* no. 64 (14):1603-1616.

Park, Junbeom, and Kun-Hong Lee. 2012. "Carbon nanotube yarns." *Korean Journal of Chemical Engineering* no. 29 (3):277-287.

Park, Jung-Hwan, Mark G Allen, and Mark R Prausnitz. 2005. "Biodegradable polymer microneedles: fabrication, mechanics and transdermal drug delivery." *Journal of Controlled Release* no. 104 (1):51-66.

Prausnitz, M.R., S. Mitragotri, and R. Langer. 2004. "Current status and future potential of transdermal drug delivery." *Nature Reviews Drug Discovery* no. 3 (2):115-124.

Roxhed, Niclas, T Christian Gasser, Patrick Griss, Gerhard A Holzapfel, and Göran Stemme. 2007. "Penetration-enhanced ultrasharp microneedles and prediction on skin interaction

for efficient transdermal drug delivery." *Microelectromechanical Systems, Journal of* no. 16 (6):1429-1440.

Roxhed, Niclas, Björn Samel, Lina Nordquist, Patrick Griss, and Göran Stemme. 2008. "Painless drug delivery through microneedle-based transdermal patches featuring active infusion." *Biomedical Engineering, IEEE Transactions on* no. 55 (3):1063-1071.

Sansom, E., D. Rinderknecht, and M. Gharib. 2008. "Controlled partial embedding of carbon nanotubes within flexible transparent layers." *Nanotechnology* no. 19 (3):035302.

Schmook, Fritz P, Josef G Meingassner, and Andreas Billich. 2001. "Comparison of human skin or epidermis models with human and animal skin in in-vitro percutaneous absorption." *International journal of pharmaceutics* no. 215 (1):51-56.

Scriven, LE. 1988. Physics and applications of dip coating and spin coating. *MRS Proceedings* no. 121.

Stoeber, Boris, and Dorian Liepmann. 2005. "Arrays of hollow out-of-plane microneedles for drug delivery." *Microelectromechanical Systems, Journal of* no. 14 (3):472-479.

Sullivan, Sean P, Dimitrios G Koutsonanos, Maria del Pilar Martin, Jeong Woo Lee, Vladimir Zarnitsyn, Seong-O Choi, Niren Murthy, Richard W Compans, Ioanna Skountzou, and Mark R Prausnitz. 2010. "Dissolving polymer microneedle patches for influenza vaccination." *Nature medicine* no. 16 (8):915-920.

Takeuchi, Hiroyuki, Shuichi Terasaka, Takanobu Sakurai, Atsushi Furuya, Hidetoshi Urano, and Kenji Sugibayashi. 2011. "Variation assessment for in vitro permeabilities through yucatan micropig skin." *Biological and Pharmaceutical Bulletin* no. 34 (4):555-561.

Teo, KBK, M Chhowalla, GAJ Amaratunga, WI Milne, DG Hasko, G Pirio, P Legagneux, F Wyczisk, and D Pribat. 2001. "Uniform patterned growth of carbon nanotubes without surface carbon." *Applied Physics Letters* no. 79:1534-1536.

Upadhyayula, Venkata KK, Shuguang Deng, Martha C Mitchell, and Geoffrey B Smith. 2009. "Application of carbon nanotube technology for removal of contaminants in drinking water: a review." Science of the total environment no. 408 (1):1-13.

Verbaan, FJ, SM Bal, DJ Van den Berg, JA Dijksman, M Van Hecke, H Verpoorten, A van den Berg, R Luttge, and JA Bouwstra. 2008. "Improved piercing of microneedle arrays in dermatomed human skin by an impact insertion method." *Journal of Controlled Release* no. 128 (1):80-88.

Wang, Ping M, Megan Cornwell, James Hill, and Mark R Prausnitz. 2006. "Precise microinjection into skin using hollow microneedles." *Journal of investigative dermatology* no. 126 (5):1080-1087.

Washburn, Edward W. 1921. "The dynamics of capillary flow." *Physical review* no. 17 (3):273.

Yang, Yonglai, Mool C Gupta, Kenneth L Dudley, and Roland W Lawrence. 2005. "Novel carbon nanotube-polystyrene foam composites for electromagnetic interference shielding." Nano Lett no. 5 (11):2131-2134.

Yoon, Youngsam, Gil S Lee, Koangki Yoo, and Jeong-Bong Lee. 2013. "Fabrication of a Microneedle/CNT Hierarchical Micro/Nano Surface Electrochemical Sensor and Its In-Vitro Glucose Sensing Characterization." *Sensors* no. 13 (12):16672-16681.

Yu, L. M., F. E. H. Tay, D. G. Guo, L. Xu, and K. L. Yap. 2009. "A microfabricated electrode with hollow microneedles for ECG measurement." *Sensors and Actuators A: Physical* no. 151 (1):17-22.

Yu, Min-Feng, Oleg Lourie, Mark J Dyer, Katerina Moloni, Thomas F Kelly, and Rodney S Ruoff. 2000. "Strength and breaking mechanism of multiwalled carbon nanotubes under tensile load." *Science* no. 287 (5453):637-640.

Zhang, Ying, Ken Brown, Kris Siebenaler, Amy Determan, Daniel Dohmeier, and Kris Hansen. 2012. "Development of lidocaine-coated microneedle product for rapid, safe, and prolonged local analgesic action." *Pharmaceutical research* no. 29 (1):170-177.

Zhou, Cui-Ping, Yu-Ling Liu, Hong-Liang Wang, Peng-Xiao Zhang, and Jin-Lan Zhang. 2010. "Transdermal delivery of insulin using microneedle rollers in vivo." *International journal of pharmaceutics* no. 392 (1):127-133.

Zhou, Jijie. 2005. *Nanowicking: Multi-Scale Flow Interaction with Nanofabric Structures*, California Institute of Technology, Pasadena, CA.